



8-2004

## **Boundary Layer Flow Acceleration by Paraelectric and Peristaltic EHD Effects of Aerodynamic Plasma Actuators**

Madhan Raja Chandra Mohan  
*University of Tennessee - Knoxville*

Follow this and additional works at: [https://trace.tennessee.edu/utk\\_gradthes](https://trace.tennessee.edu/utk_gradthes)

 Part of the [Electrical and Computer Engineering Commons](#)

---

### **Recommended Citation**

Mohan, Madhan Raja Chandra, "Boundary Layer Flow Acceleration by Paraelectric and Peristaltic EHD Effects of Aerodynamic Plasma Actuators. " Master's Thesis, University of Tennessee, 2004.  
[https://trace.tennessee.edu/utk\\_gradthes/2184](https://trace.tennessee.edu/utk_gradthes/2184)

This Thesis is brought to you for free and open access by the Graduate School at TRACE: Tennessee Research and Creative Exchange. It has been accepted for inclusion in Masters Theses by an authorized administrator of TRACE: Tennessee Research and Creative Exchange. For more information, please contact [trace@utk.edu](mailto:trace@utk.edu).

To the Graduate Council:

I am submitting herewith a thesis written by Madhan Raja Chandra Mohan entitled "Boundary Layer Flow Acceleration by Paraelectric and Peristaltic EHD Effects of Aerodynamic Plasma Actuators." I have examined the final electronic copy of this thesis for form and content and recommend that it be accepted in partial fulfillment of the requirements for the degree of Master of Science, with a major in Electrical Engineering.

Dr .J. Reece Roth, Major Professor

We have read this thesis and recommend its acceptance:

Dr. Marshall Pace, Dr. Mostafa Howlader

Accepted for the Council:

Carolyn R. Hodges

Vice Provost and Dean of the Graduate School

(Original signatures are on file with official student records.)

To the Graduate Council:

I am submitting herewith a thesis written by Madhan Raja Chandra Mohan entitled, "Boundary Layer Flow Acceleration by Paraelectric and Peristaltic EHD Effects of Aerodynamic Plasma Actuators". I have examined the final electronic copy of this thesis for form and content and recommend that it be accepted in partial fulfillment of the requirements for the degree of Master of Science, with a major in Electrical Engineering.

Dr .J. Reece Roth  
\_\_\_\_\_  
Major Professor

We have read this thesis  
and recommend its acceptance:

Dr. Marshall Pace  
\_\_\_\_\_

Dr. Mostafa Howlader  
\_\_\_\_\_

Accepted for the Council:

Anne Mayhew  
\_\_\_\_\_  
Vice Chancellor and Dean of Graduate Studies

(Original signatures are on file with official student records)

BOUNDARY LAYER FLOW ACCELERATION BY PARAELECTRIC AND  
PERISTALTIC EHD EFFECTS OF AERODYNAMIC PLASMA ACTUATORS

A Thesis

Presented for the

Master of Science Degree

The University of Tennessee, Knoxville

Madhan Raja Chandra Mohan

August 2004

## **ACKNOWLEDGEMENTS**

Sincere thanks to my advisor Professor J. Reece Roth for providing me the opportunity to pursue my Master's at this university and for guiding me towards the completion of this thesis. I also thank Dr. Marshall Pace and Dr. Mostafa Howlader for serving on my thesis committee. Special thanks to Mr. Steve Wilkinson for his support and encouragement during my work at NASA Langley Research Center. Also this work was supported in part by AFOSR Contract AF F49620-01-1-0425. Thanks to all the faculty and staff at our department for making my graduate study such a rewarding experience.

I am grateful to all my friends both here in the US and back home in India. And finally, thanks to my parents for their love and encouragement. I owe it all to you.

## **ABSTRACT**

Plasma actuators based on the OAUGDP<sup>TM</sup> (One Atmosphere Uniform Glow Discharge Plasma) promise to be a convenient method to modify aerodynamic boundary layers. The development of the OAUGD Plasma has made it possible to locate enough plasma actuators on airfoils and the wings and fuselage of aircraft to have significant effects on flow control and re-attachment at relatively low power cost. In this study OAUGD Plasma actuators have been used to effect flow re-attachment and to manipulate aerodynamic flows, possibly leading to improved methods of flight control. The OAUGDP<sup>TM</sup> actuators have been tested in the 7 x 11 Inch Low Speed Wind Tunnel at the NASA Langley Research Center during several experimental campaigns that began in the mid 1990's. The 7 x 11 Inch Low Speed Wind Tunnel is instrumented to conduct drag measurements, smoke flow visualization tests, Pitot tube velocity profile measurements and airfoil flow re-attachment visualization studies.

This thesis is concerned with two EHD (electrohydrodynamic) flow control methods that utilize only RF displacement currents to produce the body forces that accelerate the plasma; paraelectric and peristaltic (traveling wave) flow acceleration. Paraelectric flow acceleration is achieved when the applied electric field acts on the net charge density of the plasma, to provide a body force capable of accelerating the neutral gas to velocities as high as 10 m/sec. During the acceleration process, the plasma moves paraelectrically towards increasing electric field gradients, and drags the neutral gas along with it as the result of frequent ion-neutral Lorentzian collisions. Peristaltic flow acceleration results from a traveling electrostatic wave, analogous to the apparent motion

of light in a phased array of bulbs on a theatre marquee. To produce a traveling electrostatic wave, adjacent plasma actuators are energized at progressively larger phase angles. The resulting horizontal electric field produces a body force that accelerates the plasma.

A OAUGDP<sup>TM</sup> panel or a plasma actuator intended for aerodynamic flow acceleration consists of linear strip electrodes adhering to either side of a dielectric panel. The actuators are energized using RF power at voltages between 0 and 10 kV, and frequencies between 0.5 kHz and 8 kHz. A major contribution described in this thesis was the development of flexible and ceramic panels, the polyphase signal generator based on LabVIEW, and accessories for the polyphase power supply. During development of the plasma actuators, many electrode geometries were tested to achieve the best operating conditions i.e. highest flow velocity. This thesis presents experimental results from several plasma actuator configurations, and performance data from both paraelectric and peristaltic flow acceleration.

# TABLE OF CONTENTS

<b>1. INTRODUCTION</b>	<b>1</b>
<b>1.1 BACKGROUND</b>	<b>1</b>
<b>1.2 OAUGDP™ (ONE ATMOSPHERE UNIFORM GLOW DISCHARGE PLASMA)</b>	<b>1</b>
1.2.1 DEVELOPMENT OF THE OAUGDP™	2
1.2.2 PAST ATTEMPTS TO MANIPULATE BOUNDARY LAYER	6
<b>2. EHD FLOW ACCELERATION</b>	<b>9</b>
<b>2.1 PARAELECTRIC FLOW ACCELERATION</b>	<b>11</b>
<b>2.2 PERISTALTIC FLOW ACCELERATION</b>	<b>13</b>
<b>3. CO-PLANAR PLASMA ACTUATORS</b>	<b>15</b>
<b>3.1 DEVELOPMENT OF PLASMA ACTUATORS</b>	<b>15</b>
<b>3.2. COPLANAR ELECTRODE GEOMETRIES</b>	<b>17</b>
3.2.1 PARAELECTRIC PLASMA ACTUATORS	19
3.2.2 PERISTALTIC PLASMA PANELS	22
<b>3.3 ROBUSTNESS OF PLASMA PANELS</b>	<b>26</b>
<b>4. EXPERIMENTAL APPARATUS</b>	<b>31</b>
<b>4.1 PARAELECTRIC SYSTEM</b>	<b>31</b>
<b>4.2 DEVELOPMENT OF A POLYPHASE POWER SUPPLY</b>	<b>33</b>
4.2.1 POLYPHASE SIGNAL GENERATOR	35
4.2.2 POWER AMPLIFIER AND TRANSFORMER	41
4.2.3 PERISTALTIC EXPERIMENTAL SETUP	44
<b>4.3 SMOKE WIRE FLOW VISUALIZATION SYSTEM</b>	<b>44</b>
<b>4.4 PITOT PROBE SYSTEM</b>	<b>52</b>
<b>5. EXPERIMENTAL RESULTS AND DISCUSSION</b>	<b>55</b>
<b>5.1 SMOKE FLOW VISUALIZATION</b>	<b>55</b>
5.1.1 PREPARATION OF OAUGDP™ AIRFOIL	59
5.1.2 PARAELECTRIC FLOW RE-ATTACHMENT	61
5.1.3 SMOKE FLOW STUDIES OF PARAELECTRIC PANEL	71
5.1.4 SMOKE FLOW STUDIES OF PERISTALTIC PANEL	74
<b>5.2 BOUNDARY LAYER VELOCITY PROFILE OF PLASMA ACTUATORS</b>	<b>78</b>
5.2.1 EFFECT OF NUMBER OF PLASMA ACTUATORS ENERGIZED	84
5.2.2 PARAMETRIC VARIATIONS OF MAXIMUM FLOW VELOCITY	88

<b>6. FUTURE WORK</b>	<b>94</b>
<b>7. CONCLUSION</b>	<b>99</b>
<b>REFERENCES</b>	<b>101</b>
<b>REFERENCES</b>	<b>102</b>
<b>VITA</b>	<b>107</b>

## LIST OF FIGURES

Figure 1.1: Normal glow discharge structures in the classical parallel plate configuration of the One Atmosphere Uniform Glow Discharge Plasma with dielectric-coated electrodes.	4
Figure 1.2: Characteristic shapes of riblet grooves.	7
Figure 2.1 Instantaneous normal glow discharge structures in the co-planar flat panel One Atmosphere Uniform Glow Discharge Plasma with the dielectric-coated electrode configuration used for aerodynamic flow control.	9
Figure 2.2: Panel with multiple asymmetric electrodes used for paraelectric flow acceleration to the right.	10
Figure 2.3: Attraction of a polarizable medium into a capacitor.	11
Figure 2.4: A paraelectric plasma accelerator with electric field gradient.	12
Figure 3.1: Early design of plasma panel.	15
Figure 3.2: Modified plasma panel with electrodes on both sides of the dielectric panel.	16
Figure 3.3: Potential optimization parameters in a plasma panel.	17
Figure 3.4: Paraelectric plasma panels. (a) Figure 3.4a: Active electrodes on one side of panel, with a sheet electrode on opposite side, (b) Symmetric electrodes of opposite polarity on opposite sides of panel.	20
Figure 3.5: Asymmetric electrode configuration for coplanar paraelectric acceleration of neutral gas flow to the right.	21
Figure 3.6: Paraelectric plasma panels. (a) Flexible Kapton <sup>TM</sup> polyamide paraelectric panel (dimensions in mm), (b) Rigid aluminum oxide ceramic paraelectric panel (dimensions in mm).	23
Figure 3.7: Peristaltic plasma panels. (a) Peristaltic flow acceleration to the right by traveling electrostatic wave, (b) Configuration for combined paraelectric and peristaltic flow acceleration to the right.	25
Figure 3.8: Peristaltic plasma panels. (a) Ceramic pure peristaltic panel (dimensions in mm), (b) Ceramic combined paraelectric and peristaltic panel (dimensions in mm).	27

Figure 3.9: Peristaltic plasma panels. (a) OAUGDP™ Kapton plasma panel, (b) OAUGDP™ ceramic plasma panel.	28
Figure 4.1: Paraelectric gas flow accelerator experimental setup	31
Figure 4.2: Impedance matched paraelectric gas flow accelerator	33
Figure 4.3: Polyphase power supply system schematic	34
Figure 4.4: Polyphase signal generator schematic	36
Figure 4.5: Labview polyphase generator program, front panel	38
Figure 4.6: AT-AO-6 hardware and pin diagram	40
Figure 4.7: A staircase signal generated by the AT-AO-6 card at 2.66 kHz	42
Figure 4.8: PCI 6713 hardware and pin diagram	43
Figure 4.9: Picture showing power amplifiers and transformers.	45
Figure 4.10: Phase connection diagram of plasma actuators for a peristaltic accelerator panel.	46
Figure 4.11: Peristaltic accelerator panel mounted in the 7 X 11 Inch Low Speed Wind Tunnel at NASA Langley Research Center, operating at 3.5 kV <sub>rms</sub> and 3 kHz.	47
Figure 4.12: Smoke flow visualization system schematic.	48
Figure 4.13: Timing diagram for the trigger and time delay unit.	50
Figure 4.14: The NACA 0015 airfoil with OAUGDP™ electrode strips mounted in the NASA Langley Research Center's 7 X 11 Inch Low Speed Wind Tunnel for smoke flow tests.	51
Figure 4.15: Smoke trails around a NACA 0015 airfoil.	51
Figure 4.16: Smoke trails above a flat panel covered with plasma actutors.	51
Figure 4.17: Pitot probe system schematic	53
Figure 5.1: Airfoil showing aerodynamic forces.	56
Figure 5.2: Boundary Layer.	58

- Figure 5.3: Digital image of the airfoil mounted with plasma actuator panel in place. Chord length is 12.7 cm. A 1.07mm diameter trip wire is shown mounted near the leading edge. This trip wire is used only for some specialized tests reported later in the thesis. 60
- Figure 5.4: Effect of angle of attack with seven plasma actuators energized with 4.2 kV rms, 4.2 kHz and a wind tunnel speed of 2.85 m/sec. 62
- Figure 5.5: Effect of plasma location and number of plasma actuators energized. The angle of attack is 6 °, electrodes operated at 4.5 kV rms, 3.5 kHz and a wind tunnel speed of 2.85 m/sec. 64
- Figure 5.6: Effect of plasma actuator location and number of plasma actuators energized. The angle of attack is 6 °, electrodes operated at 4.5 kV rms, 3.5 kHz, a wind tunnel speed of 2.85 m/sec. 66
- Figure 5.7: Effect of angle of attack with actuator #1 near the leading edge energized with 4.2KVrms, 4.2 kHz and a wind tunnel speed of 2.85 m/sec. 68
- Figure 5.8: Effect of Trip Wire. Actuator #1 was energized with 4.2KVrms, 4.2 kHz and a wind tunnel speed of 2.85 m/sec. 69
- Figure 5.9: Flow re-attachment at high angle of attack, angle of attack - 16° at 3.6 kVrms, 4.2 kHz and a wind tunnel speed of 2.85 m/sec. 70
- Figure 5.10: Flow re-attachment at high wind tunnel velocity, angle of attack - 8° and at 4.0 kVrms, 4.2 kHz, and a wind tunnel velocity of 7.6 m/sec. 70
- Figure 5.11: Smoke Flow Studies of Paraelectric Panel. (a) Smoke trails with wind tunnel velocity of 1. 6 meters/sec and paraelectric plasma actuators not energized,. (b) Smoke trails with wind tunnel velocity of 1. 6 meters/sec and all 12 paraelectric plasma actuators energized with 3.5kV rms and 4.0 kHz. 72
- Figure 5.12: Smoke Flow Studies of Paraelectric Panel. (a) Smoke trails with wind tunnel velocity of 1.6 meters/sec and only the first paraelectric plasma actuator energized with 3.5 kV rms and 4.0 kHz, (b) Position of the 12 plasma actuators when plasma actuators are energized with 3.5 kV rms and 4.0 kHz. 73
- Figure 5.13: Smoke trails of the pure peristaltic panel of figures 3.7a and 3.8a, showing both plasma off and plasma on conditions. Electrodes were energized with 3 kV rms, 4 kHz and the wind tunnel velocity was 3.95 meters/sec. 75
- Figure 5.14: Smoke trails of the combined peristaltic and paraelectric panel, showing both plasma off and plasma on conditions. Electrodes were energized with 3.5 kV rms, 4 kHz and the wind tunnel velocity was 3.95 meters/sec. 77

- Figure 5.15: Combined peristaltic and piezoelectric ceramic panel mounted in the wind tunnel. Arrows indicate the Pitot tube and position of the Pitot tube opening 1.5 cm downstream of the last actuator. 79
- Figure 5.16: Opening of Pitot tube used in the present investigation, inside diameter 0.36 mm. 79
- Figure 5.17: Velocity profile with plasma off and a wind tunnel velocity of 3.95 meters/sec. 81
- Figure 5.18: Velocity profile when all electrodes are energized with wind tunnel off. The Pitot probe system contributed an artificial 0.5 m/sec zero offset. 82
- Figure 5.19: Pitot tube boundary layer velocity profiles taken with a wind tunnel velocity of 1.6 meters/sec, all 12 plasma actuators on the panel energized at 3.5 kV rms, 4.0 kHz, and 50 watts total power. 83
- Figure 5.20: Pitot tube boundary layer velocity profiles for positive and negative peristaltic flow, taken with a wind tunnel velocity of 1.6 meters/sec, and all 12 plasma actuators on panel energized at 3.5 kV rms, 4.0 kHz 85
- Figure 5.21: Visualization of peristaltic flow using titanium dioxide smoke. All electrodes are energized at 3.5 kV rms and 3 kHz with three complete phase cycles on the panel. (a) Phase angles were increased by 45° from left to right, (b) Same condition as (a) except the phasing was reversed. 86
- Figure 5.22: Pitot tube vertical boundary layer profiles 15 mm from the edge of plasma actuator # 1 with the wind tunnel off, 3.5 kV rms, 4.0 kHz, and for 2, 4, 6, 8, 10, and 12 plasma actuators energized. 87
- Figure 5.23: The induced wall-jet velocity 1.5 cm from the last plasma actuator as a function of the number of plasma actuators energized, and at the height of the boundary layer velocity maximum. 89
- Figure 5.24 The maximum jet velocity in the boundary layer as a function of the RF frequency with the wind tunnel off, all 12 electrodes on the panel energized, and the RF voltage 4.5 kV rms. 90
- Figure 5.25: Peristaltically and piezoelectrically induced velocities as functions of RF driving voltage on 12 plasma actuators at a RF frequency of 6 kHz. 92
- Figure 5.26: Peristaltically induced velocity as a function of RF driving voltage and frequency on plasma actuators. 93
- Figure 6.1: Low cost power supply circuit using an automotive ignition coil. 95

Figure 6.2: Ignition coil and flyback transformer schematics.	95
Figure 6.3: Kapton <sup>TM</sup> peristaltic panel installed on a particle imaging velocimetry test section.	97
Figure 6.4: Coplanar OAUGDP <sup>TM</sup> with electrodes embedded in dielectric material.	98

# **1. INTRODUCTION**

## **1.1 Background**

Plasma is the fourth state of matter. If heat is added to a solid, it will first undergo a phase transition from the solid to the liquid state and then from the liquid to the gaseous state. If further heat is added to the gas, the forces binding the electrons to the atoms in the gas are overcome, and the gas forms an electrically conducting plasma. This fourth state of matter can be produced using very high temperatures, strong constant electric fields, or radio frequency (RF) electromagnetic fields. Plasma can be found all around us in nature. Ninety-five percent of our universe is made up of plasma. Applications of plasma include streetlights, fluorescent lights, fabrication of microelectronic devices, flat panel television screens, welding, and many other applications that one might encounter in everyday life.

## **1.2 OAUGDP™ (One Atmosphere Uniform Glow Discharge Plasma)**

In the past it was not possible to generate a stable glow discharge plasma above ten Torr or at atmospheric pressure. In classical electrical discharge physics, if one tries to raise the pressure of a low pressure DC glow discharge, a filamentation instability develops between one and ten Torr in which the glow discharge no longer covers the electrodes, but constricts into a thin streamer. This instability may be accompanied by the glow-to-arc-transition, the latter triggered by higher current densities, cathode heating, and thermionic emission from the cathode.

Operation of a DC normal glow discharge at pressures at and above one atmosphere in hydrogen and air was reported by von Engle et al in 1933. This was

possible in their work only if the cathode was cooled aggressively to inhibit the glow-to-arc- transition. Their procedure also required that a DC glow discharge be established at low pressure [1], and the pressure increased gradually to one atmosphere. A vacuum system was still needed for this kind of atmospheric glow discharge. This method is not satisfactory for industrial or aeronautical applications because of the requirement for a vacuum system, and the unstable nature of the atmospheric glow discharge that can undergo the glow-to-arc-transition. Another atmospheric plasma is the Dielectric Barrier Discharge (DBD), a filamentary low power density plasma at one atmosphere that is generated by electro avalanches between parallel plates. The DBD has been used in Europe to produce ozone for the treatment of public water supplies since the 19<sup>th</sup> century. This filamentary plasma is non uniform and can damage workpieces in contact with it, which is usually not desired.

### **1.2.1 Development of the OAUGDP<sup>TM</sup>**

In the early 1990s it was discovered that if the ion population of an atmospheric glow discharge plasma is trapped between the insulated electrodes of a low frequency RF discharge by a proper choice of RF frequency, a uniform, time-dependent normal glow discharge can be sustained at one atmosphere. The structures and characteristics of the resulting normal glow discharge reverse each half cycle and follow the applied RF voltage. This type of electrical discharge is called the One Atmosphere Uniform Glow Discharge Plasma (OAUGDP<sup>TM</sup>) [2,3]. In January 1992 J.R. Roth and co-workers at the University of Tennessee operated the first One Atmosphere Uniform Glow Discharge Plasma (OAUGDP<sup>TM</sup>) based on the ion trapping mechanism.

The OAUGDP<sup>TM</sup> is a capacitively coupled plasma, created by displacement currents, with no real currents flowing to the electrodes. An OAUGDP<sup>TM</sup> is operated with at least one electrode covered with dielectric material. The dielectric allows charge accumulation that carries the discharge from one half cycle to the next and inhibits RF arcs [4,5].

One dimensional numerical simulation by Ben Gadri [4,5] and fast photography by Massines et al. [6] show that the OAUGDP<sup>TM</sup> displays the phenomenology and features of the normal glow discharge: Aston's law for the electric field in the cathode region, a cathode dark space, a negative glow, a Faraday dark space and a positive column. This structure in a parallel plate discharge is illustrated in Figure 1.1.

Paschen's law states that the breakdown voltage of a gas depends on the product of the pressure of the gas,  $P$  and the distance between the electrodes,  $d$ . There is a unique  $Pd$  value, referred to as the Stoletow point, where the volumetric ionization is a maximum. The classical normal glow discharge operates at the Stoletow point, where the energy cost of producing an ion-electron pair is a minimum. Another advantage of this type of plasma in aerodynamic applications, other than operating in the atmosphere, is that it does not require a magnetic field. Also, the EHD body force is more than one order of magnitude greater than MHD body forces that can be realistically generated for aerodynamic applications [7]. Another fundamental advantage of EHD forces is that the electric field can do work on the charged particles and, through strong collisional coupling at one atmosphere, on the aerodynamic flow itself. A static magnetic field always acts orthogonally to the charged particle velocities, and therefore can do no work

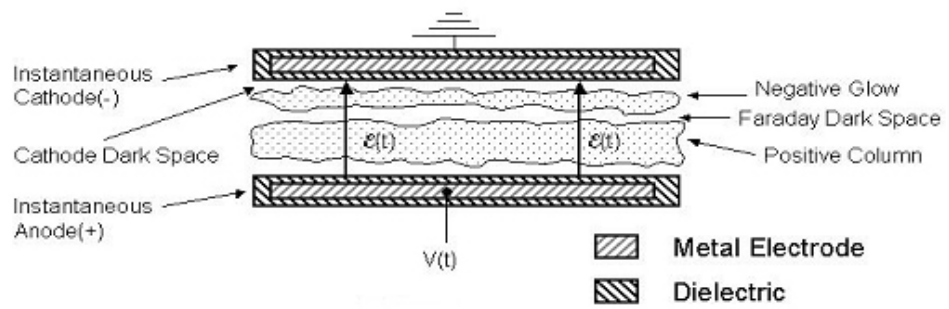


Figure 1.1: Normal glow discharge structures in the classical parallel plate configuration of the One Atmosphere Uniform Glow Discharge Plasma with dielectric-coated electrodes.

on the particles or the flow. Thus, EHD body forces associated with an OAUGDP<sup>TM</sup> plasma have significant advantages for aerodynamic flow control applications, but the issues are how to effectively produce the required plasma at one atmosphere, and how to configure and generate the electric fields to produce effects that may be useful for such applications as drag reduction, heat transfer, lift, or flow separation.

The OAUGD Plasma operates on the principle of ion-trapping. Ion/charge trapping refers to a specific, constrained, periodic oscillation of ions and/or electrons along electric field lines between a pair of electrodes, at least one of which is covered with a dielectric. The electrodes are characteristically either plane parallel plates, or side-by-side in flat-panel aerodynamic plasma actuator applications. This electrostatic trapping may reduce plasma polarization, it keeps ions from knocking secondary electrons off the instantaneous cathode (which may initiate avalanches or breakdown), and most importantly, it prevents ions from heating the cathode surface and initiating a glow-to-arc transition due to thermionic emission.

The magnitudes of the parameters required for bench-top demonstration of the OAUGD plasma are easily attainable. For instance, a frequency of several kilohertz, an rms voltage of several kilovolts, an electrode gap distance of 2 to 5 mm, and an electric field above 8.5 kV/cm are adequate to initiate the plasma in a plasma actuator in air at atmospheric pressure. The OAUGD Plasma is not hard-starting, and does not require external initiation with a Tesla coil or spark gap. While the dissipative (or plasma) current in the OAUGD Plasma is small (about 0.030 amp rms per plasma actuator in these experiments), without special impedance matching, the reactive, non-dissipative

current can be large (approximately 0.4 amp rms) and the power supply should be sized accordingly.

### **1.2.2 Past Attempts to Manipulate Boundary Layer**

Various methods have been used to modify aerodynamic boundary layers [8-19]. These methods can be divided into three categories;

#### *1. Mass flow injection and removal:*

This is accomplished by single or a series of holes or slits on the surface. The injection or removal of air or other gases through such openings helps in boundary layer modification [20].

#### *2. Modifying surface topology:*

A number of ideas of zoological origin have arisen from fast swimming sharks and dolphins. Experimental studies in the 1970's showed that small grooves (riblets) aligned with the flow modified the near-wall structure of the boundary layer and reduced drag. Riblets come in different shapes and sizes, some of which are the L, U and V grooves illustrated in Figure 1.2. According to published data this can reduce the skin friction drag up to 8% [21]. MEM (Micro Electro Mechanical) effectors are used to actively modify the aerodynamic boundary layer. They consist of micro-scale shear stress sensors and actuators on the surface, which are connected through a neural network. The neural network senses the flow, energizes the actuators, which then alters the boundary layer [22].

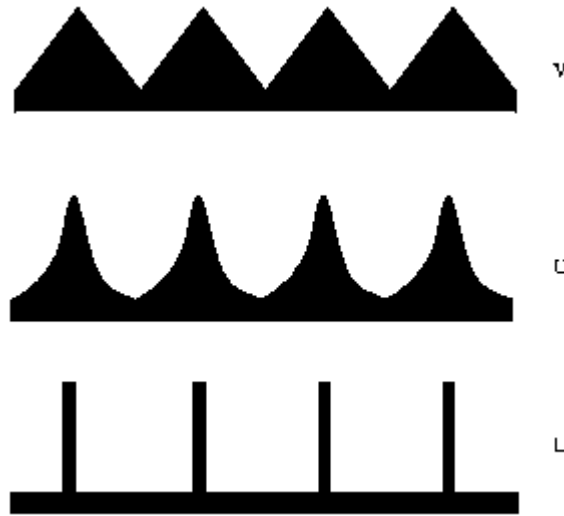


Figure 1.2: Characteristic shapes of riblet grooves.

### 3. *Energizing the mass flow:*

Energizing the mass flow can be accomplished by the following methods: 1) Direct Microwave heating; 2) Laser addition of heat energy; 3) Magnetohydrodynamic (MHD) flow acceleration; and 4) Electrohydrodynamic (EHD) flow acceleration using OAUGDP<sup>TM</sup> plasma actuators. Magnetohydrodynamic (MHD) approaches have received substantial attention over the years and have been used to control the turbulent viscous drag in aerodynamic boundary layers. Most MHD concepts have been based on ionized flow around a magnetized hypersonic vehicle. EHD is a promising alternative to MHD flow control. Paraelectric and peristaltic flow control are alternate EHD methods of flow acceleration and boundary layer modification.

## Drawbacks of Conventional Methods

The conventional methods of flow control/drag reduction have many disadvantages when compared to EHD flow control.

1. *Mass flow injection and removal:*

This technique needs heavy piping and pumps in the system to provide suction or blowing through holes or slits. This method is complex, adds weight to the aircraft, and is a source of airframe noise.

2. *Active surface enhancements:*

- a. *MEMS*

This technique needs complex and delicate sensors and actuators on the surface of the wings that are difficult to clean and maintain.

- b. *Riblets*

The stream-wise riblet grooves on the upper surface of a wing are more practical than the MEMs. One of the main problems of this technique is that riblets are easily damaged or clogged, and they are difficult to maintain.

- c. *MHD*

MHD flow control methods require strong magnetic fields generated by heavy magnets, and large real currents in the plasma that damage electrodes and heat surrounding structures. EHD methods do not use magnets, which drastically reduces the system weight compared to MHD flow control.

## 2. EHD FLOW ACCELERATION

The parallel plate configuration of the OAUGDP™ discussed previously is not useful for aerodynamic flow control, so the co-planar OAUGDP™ shown in Figure 2.1 was developed [23,24] to form a flat layer of surface plasma that can serve as a plasma actuator. In this configuration, arched electric field lines contain the structures of the normal glow discharge along their length. These structures reverse direction with each RF half cycle. This more complex co-planar geometry has not been modeled in the detailed way that the one-dimensional parallel plate geometry was modeled by Ben Gadri [4,5], so the plasma characteristics and the time- and space-resolved profiles of the co-planar geometry are not known in as much detail as those of the parallel plate OAUGDP™ [25].

In order to provide the electric fields and electric field gradients that induce directional flow of the neutral gas above a flat surface, a variety of co-planar OAUGDP™ electrode configurations have been developed. [23,24,26]

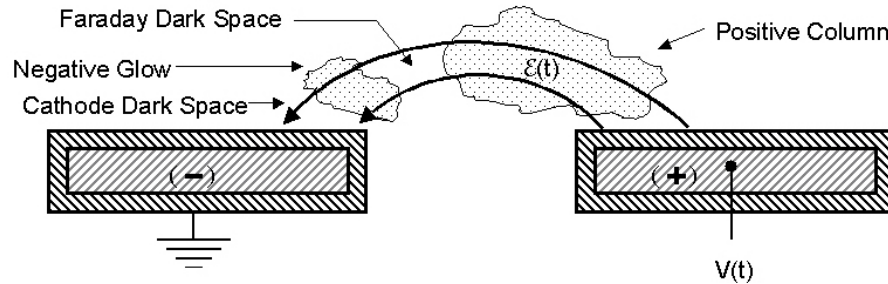


Figure 2.1 Instantaneous normal glow discharge structures in the co-planar flat panel One Atmosphere Uniform Glow Discharge Plasma with the dielectric-coated electrode configuration used for aerodynamic flow control.

The development of the One Atmosphere Uniform Glow Discharge Plasma (OAUGDP™) has made it possible to cover the wings and fuselage of aircraft with glow discharge plasma actuators [23] for aerodynamic flow control at a relatively low power cost. These plasma actuators are mechanically robust, characteristically require no more than a few tens of watts per meter of length, and can provide, through Lorentzian collisions, a purely electrohydrodynamic (EHD) coupling between the electric field in the plasma and the neutral gas in the boundary layer. This coupling is strong enough at one atmosphere to cause aerodynamically significant flow acceleration in the boundary layer, to allow manipulation of the boundary layer and free stream flow, to re-attach flows to an airfoil at high angles of attack, to increase the stall angle of wings, and to allow peristaltic acceleration of neutral gas flow by a traveling electrostatic wave on the surface of a flat plate.

A plasma actuator panel intended for flow acceleration is shown in Figure 2.2, where the electrodes of each actuator are asymmetrically attached above and below an insulating panel.



Figure 2.2: Panel with multiple asymmetric electrodes used for paraelectric flow acceleration to the right.

## 2.1 Paraelectric Flow Acceleration

Paraelectric body forces can be regarded as the electrostatic analog of paramagnetism, in which polarizable media are attracted by an electric field gradient, as illustrated in Figure 2.3. The flow of plasma can be made continuous by establishing a permanent electric field gradient, as illustrated in Figure 2.4. The continuous flow of plasma to the regions of high electric field gradient to the left will cause a continuous flow of neutral gas to the left, the result of Lorentzian collisions of the (positive) plasma ions with the neutral molecules.

It has been shown elsewhere that by equating the kinetic (stagnation) pressure of the flow from a paraelectric plasma actuator to the electrostatic pressure in the plasma driving it, the neutral gas flow velocity can be shown to be proportional to the average electric field in the source [25,27]. In typical applications, limited by sparking and tracking at the actuator electrodes, the paraelectrically-induced flow velocity of a single plasma actuator is no more than about 4 meters/sec [28]. For many applications, including subsonic aerodynamics, higher velocities are desirable, such as the 40-60 meters/sec needed for takeoff and landing of aircraft.

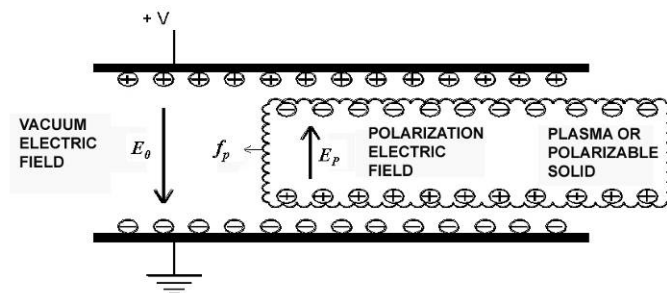


Figure 2.3: Attraction of a polarizable medium into a capacitor.

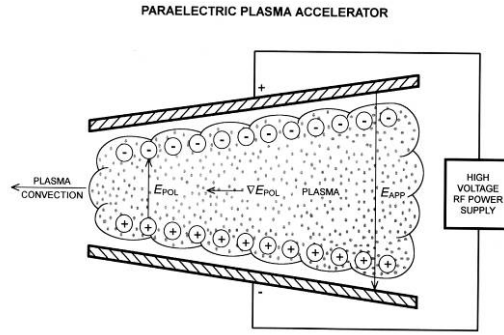


Figure 2.4: A paraelectric plasma accelerator with electric field gradient.

The coupling between the electric field in the plasma and the neutral gas is the result of Lorentzian collisions between the ion population and the neutral gas. In such collisions the ions, on the average, lose all the momentum and energy they gained since their last collision. It has been shown that, at atmospheric pressure, the Lorentzian momentum transfer from the electron population gives rise to induced neutral flow velocities about a factor of one hundred less than that due to the ions [2,3], since the effect of the higher drift velocity of the electrons is overwhelmed by their small mass. Binary Coulomb collisions between ions and electrons play no significant role in the momentum transfer in a partially ionized plasma at atmospheric pressure because of the low fractional ionization.

There is an understandable tendency to disregard the ion (and electron) momentum transfer in atmospheric plasmas because of their low ionization fraction, typically one part in  $10^6$  to  $10^8$ . However, the electrostatic body force is proportional to the *net* charge density, not the ionization fraction, and it has been shown [27] that the net charge density

of atmospheric glow discharges is sufficient to create aerodynamically significant body forces, and have important effects on the neutral gas flow [23,24].

It has also been shown that if viscosity, curvature forces, and other aerodynamic effects are negligible, the total pressure, consisting of the sum of the ideal gas law pressure and the electrostatic pressure, is a constant independent of position [2,3,27]. This may be expressed as

$$nkT + \frac{\epsilon_0}{2} E^2 = \text{constant.} \quad (1)$$

From Equation (1), one can understand that the neutral gas pressure in the plasma,  $p_g = nkT$ , is smaller than the surrounding regions without electric fields. This causes an inflow of the surrounding higher pressure neutral gas. This localized region of low neutral gas pressure in the plasma is maintained because ions transfer their momentum to the neutral molecules, and accelerate the neutral gas away from regions of high electric fields.

## 2.2 Peristaltic Flow Acceleration

An EHD mechanism that may be capable in principle of achieving flow acceleration velocities up to Mach one (approximately 333 meters/sec), is peristaltic flow acceleration, described in US Patent No.5,669,583 [23]. In a peristaltic flow accelerator, successive electrodes are energized at increasing phase angles so that a traveling electrostatic wave moves horizontally along the surface normal to the electrodes. The phase velocity acts on the net charge density, and is given by,

$$v_p = \frac{\omega}{k} = v_o NL \quad \text{meters/sec} \quad (2)$$

where  $v_o$  is the driving frequency in Hertz,  $N$  the number of phases per cycle, and  $L$  the electrode spacing. With typical operating parameters of  $v_o = 3$  kHz,  $N = 8$ , and  $L = 10$  mm, one can achieve a phase velocity of a few hundred meters per second.

It can be shown that the ion drift velocity is the same as the ion-induced neutral convection velocity [26]. This relation is

$$v_{oi} = v_{di} = \mu_i E_{\max} = \frac{eV_o}{M_i v_{in}} \frac{2\pi}{NL} \quad \text{m/sec.} \quad (3)$$

With typical operating parameters, one can calculate that the peristaltically induced neutral gas drift velocity in atmospheric air may be as large as 100 m/sec [3].

### 3. CO-PLANAR PLASMA ACTUATORS

#### 3.1 Development of Plasma Actuators

The OAUGDP<sup>TM</sup> plasma in its original form is generated at one atmosphere between a pair of parallel metal plate electrodes spaced a few centimeters apart, at least one of which is insulated. However, this configuration is not appropriate for aerodynamic boundary layer control and other aerodynamic applications on a flat surface. In 1995, attempts were made to construct flat OAUGDP panels at the UT Plasma Sciences Laboratory of different geometry than that used presently. In those panels that were first built, both sets of RF electrodes were located on the same side of the dielectric panel. This configuration was problematic because it exhibited frequent tracking and sparking on the panel surface. Later attempts were made to cover the bare parallel electrodes with an insulating epoxy or dielectric tape coating in order to suppress the tracking. This measure suppressed the worst tracking, but the panel could only be operated for short durations of 5 to 10 seconds [29] before the plasma heated/chemically attacked the dielectric coating, and initiated tracking. This early panel configuration is shown in Figure 3.1.

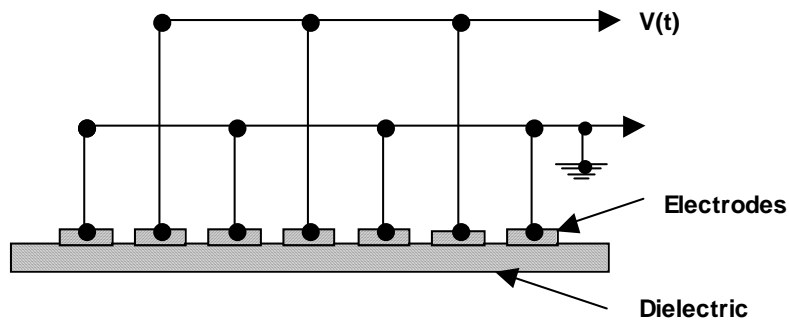


Figure 3.1: Early design of plasma panel.

The tracking problem was addressed by placing electrodes of different polarity on opposite sides of the dielectric panel, as illustrated in Figure 3.2 [23]. This drastically reduced tracking and arcing on the panel surface. This configuration allowed the panel to run for much longer durations and also made possible many options for the electrode geometry and electrical connections. A panel with the general configuration shown above has many parameters that can be optimized, as shown in Figure 3.3.

The important parameters in a plasma actuator include the actuator-to-actuator (electrode) spacing, the thickness of the dielectric panel, the thickness of the electrodes, the type of dielectric material in the panel used, the electrode width, and the space between the trailing edge of the top electrode and the leading edge of the bottom electrode, otherwise referred to as the electrode gap or displacement. The effects of altering these parameters will be discussed in detail in later sections. This electrode geometry is widely used in the aerodynamic applications of plasma actuators due to this geometric flexibility.

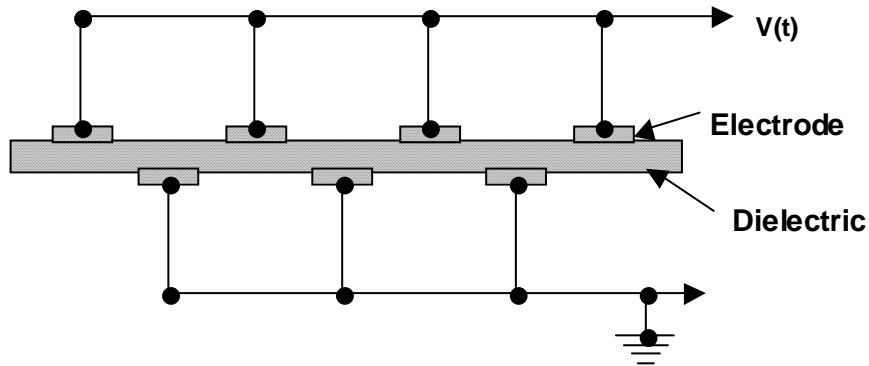


Figure 3.2: Modified plasma panel with electrodes on both sides of the dielectric panel

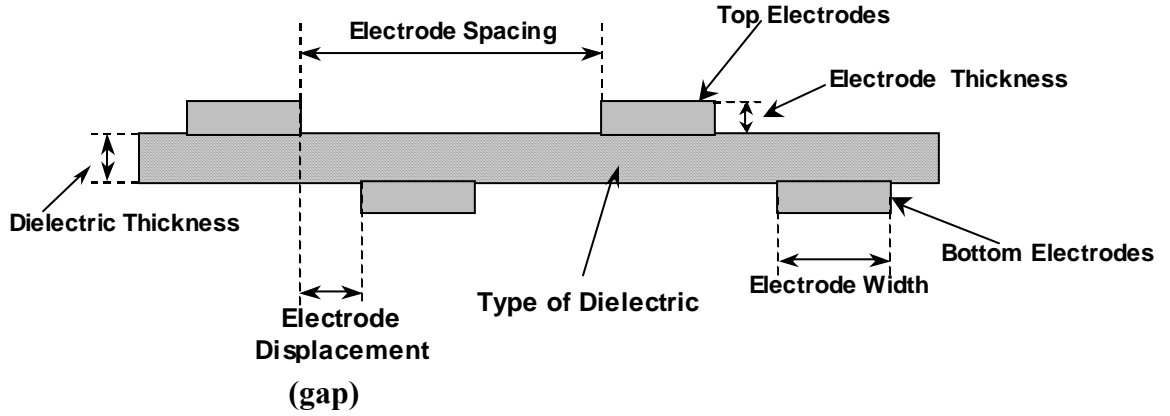


Figure 3.3: Potential optimization parameters in a plasma panel.

### 3.2. Coplanar Electrode Geometries

In this section the construction and geometry of both paraelectric and peristaltic panels are discussed. The One Atmosphere Uniform Glow Discharge Plasma (OAUGDP<sup>TM</sup>) is used in the plasma actuators discussed here. The OAUGDP<sup>TM</sup>, like all normal glow discharges, operates at the Stoletow point thus providing assurance that the generation of ion-electron pairs cannot be done more efficiently. These plasma actuators can provide, through Lorentzian collisions, a purely electrohydrodynamic (EHD) coupling between an electric field in the plasma and the neutral gas in the boundary layer [23,24].

A major goal of our research program is to improve key performance parameters of plasma actuators such as the induced flow velocity, the efficiency of the flow acceleration process, and the robustness and lifetime of the plasma actuators themselves. Plasma actuators can assume many different geometries and configurations. The most important geometric parameters of plasma actuators are listed in Table 3.1

Table 3.1 Plasma Panel Parameters

---

Properties of the dielectric panel:

- a. Dielectric constant.
- b. Endurance
- c. Plasma contact geometry.
- d. Thickness

Material used for dielectric coating and electrodes:

- a. Dielectric constant.
- b. Endurance
- c. Electrical conductivity
- d. Properties of dielectric such as flexibility and thermal properties.

Distance between the electrodes:

- a. Application specific.
- b. Optimized for application.

Thickness and width of the electrode:

- a. Minimal flow disturbance.
- b. Endurance

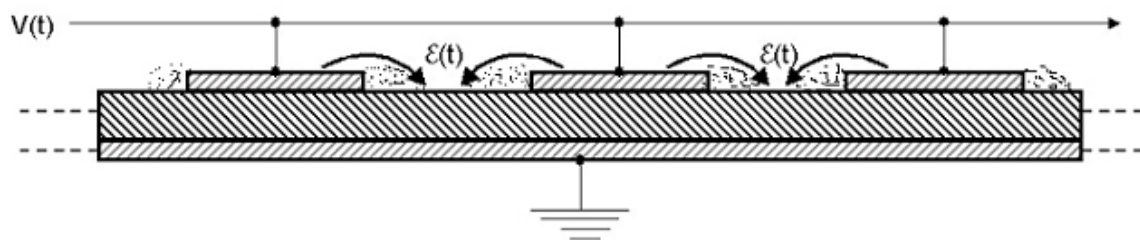
Horizontal displacement (gap) between the top and bottom electrode:

- a. Application specific
  - b. Optimized for maximum flow acceleration.
-

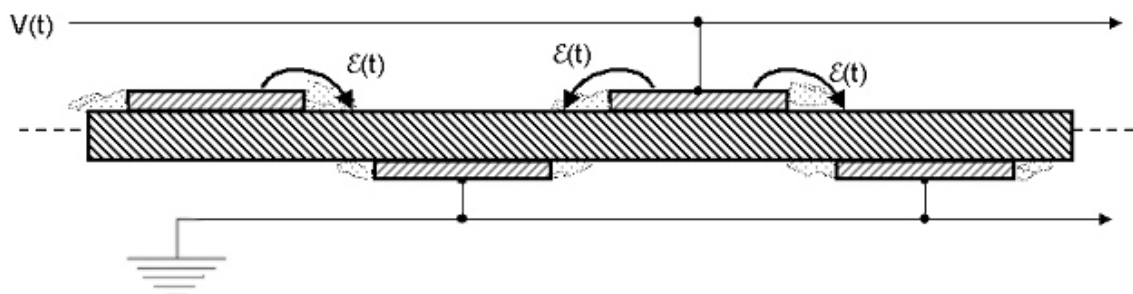
### 3.2.1 Paraelectric Plasma Actuators

These actuators can be classified in terms of electrode arrangement and type of dielectric used. Figure 3.4a shows active electrodes on the top of the dielectric panel and a solid sheet electrode on the bottom. When RF high voltage power is applied, OAUGD Plasma is produced on either side of the electrodes. This panel does not have a net flow in the horizontal direction, but the gas flows down to and horizontally away from both edges of the electrodes. These panels are used for plasma electron number density measurements, to induce drag, and for fabric treatment applications. Figure 3.4b shows the symmetric electrode panel configuration, in which electrodes of opposite polarity are placed respectively on the upper and lower surfaces of the dielectric panel. In this configuration, the bottom electrode is placed midway between the top electrodes. This panel design can be used to induce drag, treat fabrics, and for other surface treatment applications.

Figure 3.5 shows an asymmetric paraelectric panel in which electrodes of opposite polarity are located asymmetrically on the top and bottom of the dielectric panel. It is important that there be a small horizontal displacement (cira 1-2 mm) between the facing edges of the top and bottom electrodes. The plasma forms above the gap created by the displacement, between the two electrodes. For the geometry shown in Figure 3.5, the plasma will accelerate airflow to the right. These asymmetric plasma actuators are useful for aerodynamic applications because they have the ability to accelerate the airflow above the surface of the panel.

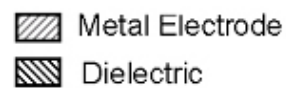


(a)



(b)

Figure 3.4: Paraelectric plasma panels. (a) Figure 3.4a: Active electrodes on one side of panel, with a sheet electrode on opposite side, (b) Symmetric electrodes of opposite polarity on opposite sides of panel.



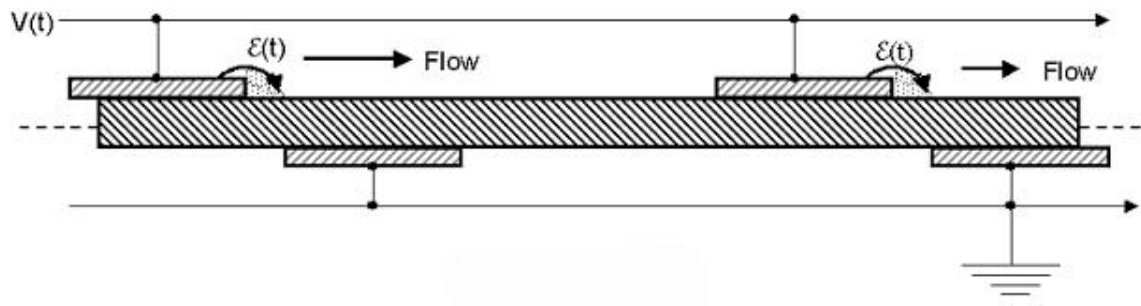
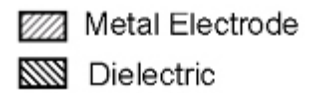


Figure 3.5: Asymmetric electrode configuration for coplanar paraelectric acceleration of neutral gas flow to the right.

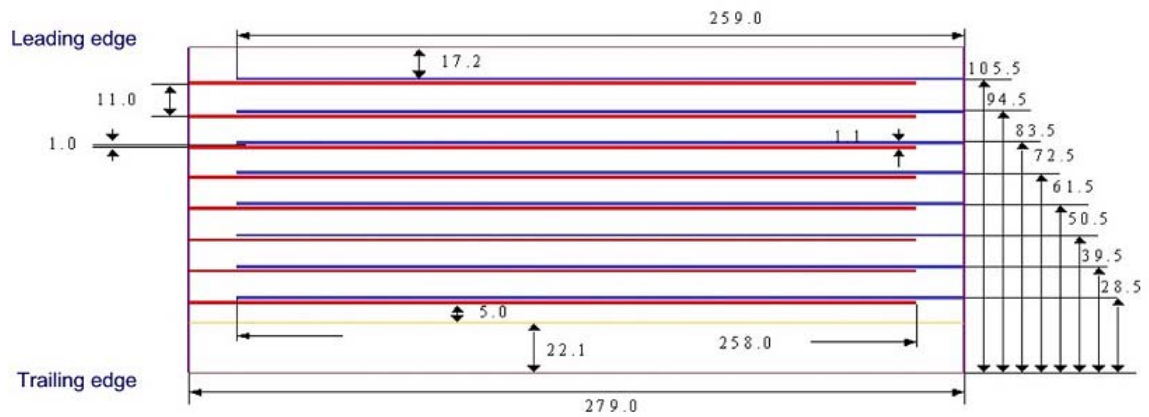


Figures 3.6a and 3.6b show two asymmetric paraelectric panels made of different dielectrics. Figure 3.6a shows a flexible asymmetric panel made of polyamide or Kapton<sup>TM</sup> dielectric material. The spacing between the actuators is 11mm and the horizontal displacement (gap) between the top and bottom electrodes is 1mm. Also Figure 3.6a indicates the leading and trailing edges when placed on an airfoil. This panel was used to take flow attachment data on a NACA 0015 airfoil using paraelectric flow acceleration. An important advantage of this panel is that it is flexible, and it can be made to conform to the shape of the airfoil. However, this panel was not able to withstand high temperatures for long durations at high plasma voltages and frequencies. This overheating causes sparking and carbonization, which damages the panel.

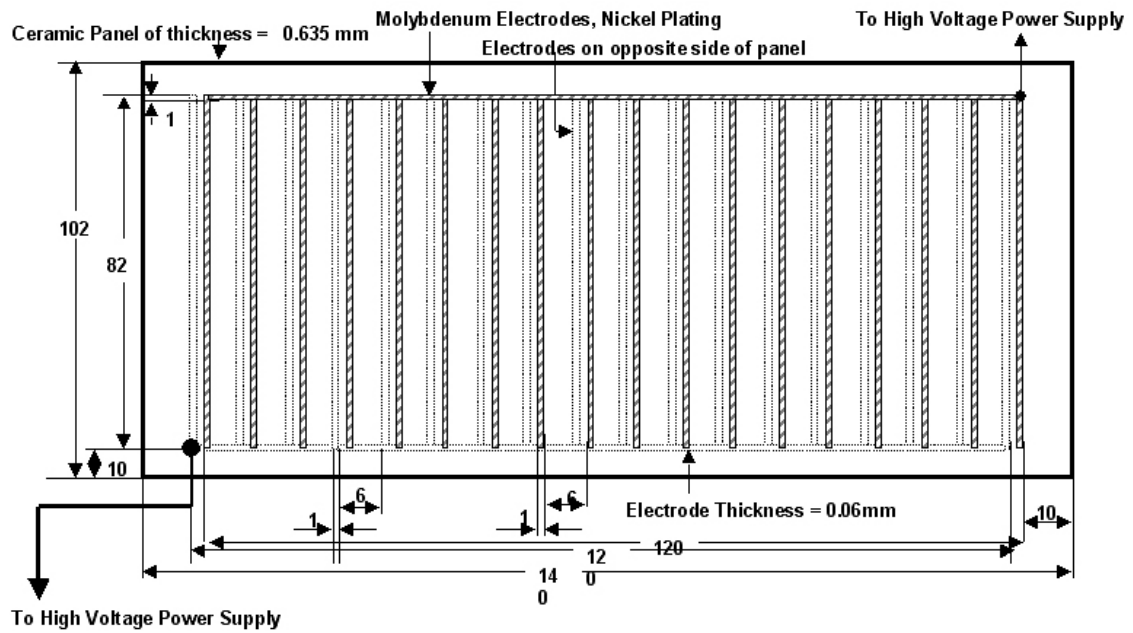
We also fabricated panels made of 0.6 mm thick aluminum oxide, with nickel-plated molybdenum electrodes only 0.06 mm thick fused to the surface. These electrodes were essentially flush with the surface, since their thickness was small compared to the thickness of the boundary layer flow and the height of the flow velocity maximum above the panel. The dimensions and layout of a pure paraelectric ceramic panel used for these investigations is shown in Figure 3.6b. The plasma forms above the horizontal gap between the two electrodes, and for the geometry shown in Figure 3.6b, will accelerate airflow to the left.

### **3.2.2 Peristaltic Plasma Panels**

The geometry and layout of plasma actuators on the peristaltic panels differs from that of the paraelectric panels. The peristaltic panels are of two types; the pure peristaltic



(a)

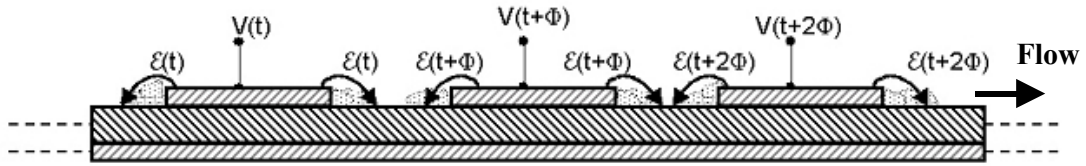


(b)

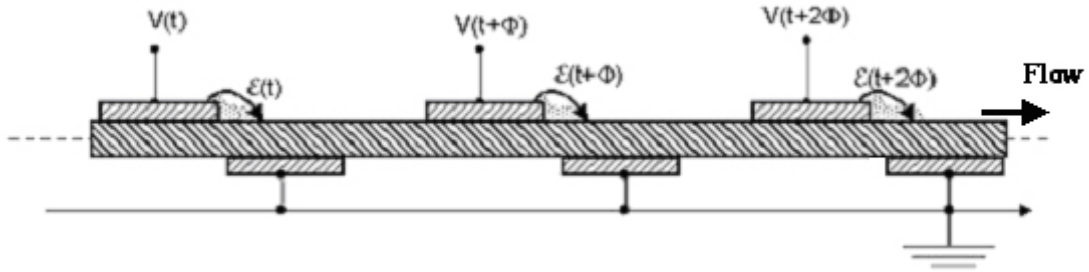
Figure 3.6: Paraelectric plasma panels. (a) Flexible Kapton™ polyamide paraelectric panel (dimensions in mm), (b) Rigid aluminum oxide ceramic paraelectric panel (dimensions in mm).

panel shown in figure 3.7a, and the combined paraelectric and peristaltic panel shown in Figure 3.7b. The peristaltic plasma actuators are driven by an 8-phase polyphase power supply like that diagrammed in Figure 4.3, to excite a traveling electrostatic wave. As seen in Figures 3.7, the electrodes are connected to different potentials with increasing phase angles. Figure 3.7a shows a pure peristaltic panel. It has electrodes on top of the dielectric panel and a solid sheet of electrical conductor on the bottom. In this actuator, the plasma is formed on both sides of each electrode. The pure peristaltic panel is so called because the flow acceleration from this panel is purely peristaltic, and the paraelectric flow acceleration effects on either side of the electrode are cancelled out. The induced flow direction can be reversed by reversing the phasing of the driving voltage.

Turbulence generated by the paraelectrically induced gas flow away from both sides of each electrode in the peristaltic panel of Figure 3.7a disrupts the peristaltic flow acceleration process to such a degree at these low velocities that we used the combined paraelectric and peristaltic ceramic panel shown in Figure 3.7b. By energizing each of the eight phases with a separate asymmetric paraelectric plasma actuator, we were able to avoid the turbulence created by the upstream-induced paraelectric flow observed on the symmetric electrodes of the pure peristaltic panel in Figure 3.7a, while allowing the paraelectrically and peristaltically induced velocities produced on the combined panel to either add or oppose each other. As shown on Figure 3.7b, the electrodes are located on both sides of the dielectric panel. The leading edge of the bottom electrode is displaced horizontally from the following edge of the top electrode by a small gap, circa 1-2 mm. The plasma forms above this gap. In this combined paraelectric and peristaltic panel, the

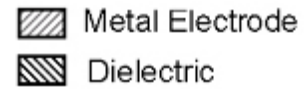


(a)



(b)

Figure 3.7: Peristaltic plasma panels. (a) Peristaltic flow acceleration to the right by traveling electrostatic wave, (b) Configuration for combined paraelectric and peristaltic flow acceleration to the right.



additive paraelectric effect gives an initial impetus to the peristaltic traveling wave. The plasma actuator electrodes are configured so that the net flow is to the right.

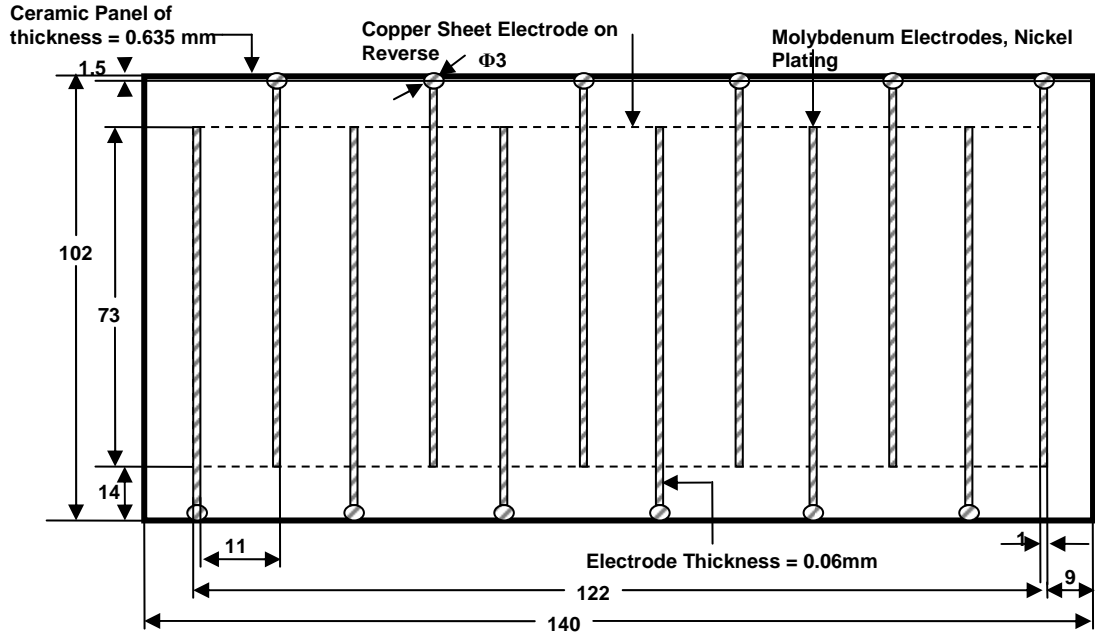
If one compares the maximum flow velocity induced by a paraelectric panel with that of a peristaltic panel for the conditions of this investigation, one observes velocities of comparable magnitude. Usually the distance between the actuators of a peristaltic panel is greater than that of the paraelectric panels, because the neighboring electrodes of a peristaltic panel are at different potentials, and sparking and tracking is more likely.

Figures 3.8a and 3.8b show the dimensions of the pure peristaltic and the combined paraelectric and peristaltic ceramic panels. The distance between the actuators is 11mm, the thickness of the electrode is 0.06mm, flush to the surface of the dielectric material.

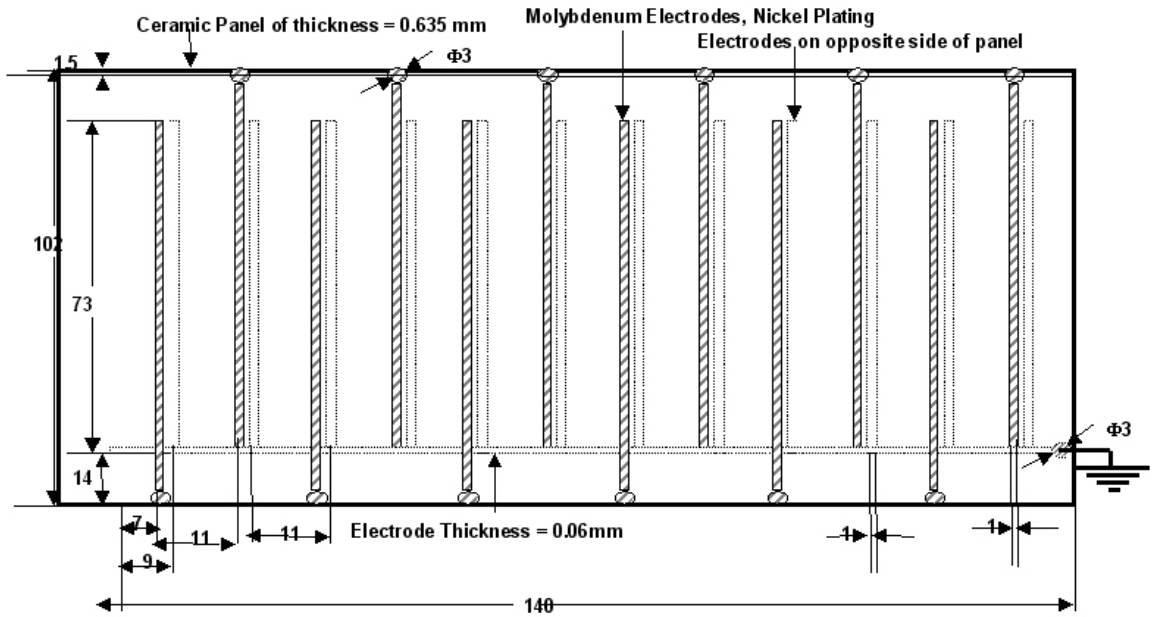
Figure 3.9a is a digital image of the Kapton<sup>TM</sup> polyamide dielectric panel. This panel is flexible and can be made to conform to the surface of the airfoil. Figure 3.9b is a digital image of the pure peristaltic ceramic panel with aluminum oxide dielectric and nickel coated molybdenum electrodes.

### **3.3 Robustness of Plasma Panels**

A concern is whether plasma actuators are robust enough for flight applications, particularly the type of long-term, repeated use they might experience if mounted on the leading edges of aircraft wings for flow re-attachment or flow control. To this end, we put a panel containing multiple plasma actuator strips through a series of tests to determine its performance under unfavorable conditions. These tests were documented by video images that are available at the website address <http://plasma.ee.utk.edu/video/>.



(a)



(b)

Figure 3.8: Peristaltic plasma panels. (a) Ceramic pure peristaltic panel (dimensions in mm), (b) Ceramic combined paraelectric and peristaltic panel (dimensions in mm).

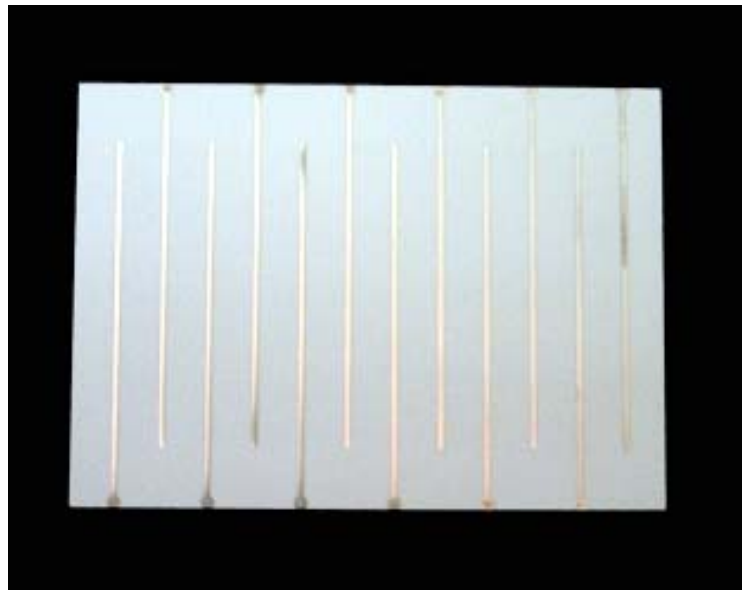


(a)

Dielectric: KAPTON™ (polyamide)

Electrode: Copper

Type: Peristaltic flow configuration



(b)

Dielectric: Aluminum oxide

Electrode: Molybdenum coated with nickel

Type: Peristaltic flow configuration

Figure 3.9: Peristaltic plasma panels. (a) OAUGDP™ Kapton plasma panel, (b) OAUGDP™ ceramic plasma panel.

#### *Air Jet Test:*

We used dry service air at about 90 psig (6.2 KPa), and the effect of the air jet on the plasma light emission was barely visible. The actuator plasma did not extinguish.

#### *Water Spray Test:*

We sprayed a heavy mist of water on a panel covered with energized plasma actuators. The plasma quenched, but the wetted area rapidly dried up as the plasma advanced inwards from the periphery of the quenched area. This process took about 30 to 60 seconds to re-establish the plasma over the entire 25 cm x 25 cm panel.

#### *Maintenance and Wear:*

Another issue is whether the plasma actuators are robust enough to withstand normal wear, abrasion, and maintenance operations associated with flight aircraft. The question often asked of any drag reduction device mounted on the fuselage of an airplane is “Can you walk on it?” We tested this issue quite literally by energizing a 25 cm square plasma panel, and actually walking on the panel. Walking on an un-energized panel and then energizing it showed no visible effects of dirt, contamination, etc. on plasma formation. Actually walking on the *energized* panel quenched the plasma under the Principal Investigator’s footprint, but had no other apparent effect on the surrounding plasma, or on the panel after being walked on.

#### *Electrical Safety*

Finally, there is an understandable concern whether the energized panels can be made electrically safe so that anyone touching it will not be electrocuted or otherwise harmed. We tested this by impedance matching the panel under test, and grounding the upper surface exposed to the atmosphere. Under these conditions, the plasma was generated in

the normal manner, even with a grounding wand in contact with the upper electrodes, and direct contact of the upper electrodes with the Principal Investigator's hand gave no sensation of electrical shock or current flow.

## 4. EXPERIMENTAL APPARATUS

This chapter discusses the power supply systems required to produce both OAUGDP™ paraelectric and peristaltic gas flow acceleration. This chapter also describes the experimental apparatus used to make smoke flow visualization images and to measure boundary layer velocity profiles with a Pitot tube.

### 4.1 Paraelectric System

The power supply system needed to produce paraelectric gas flow acceleration is not complicated compared to that of a peristaltic gas flow accelerator. The system requires an analog signal generator, a power amplifier, and a high voltage transformer, as diagrammed in Figure 4.1.

The above diagram shows the paraelectric gas flow accelerator without impedance matching. An airfoil is used instead of the plasma panel shown in Figure 4.1

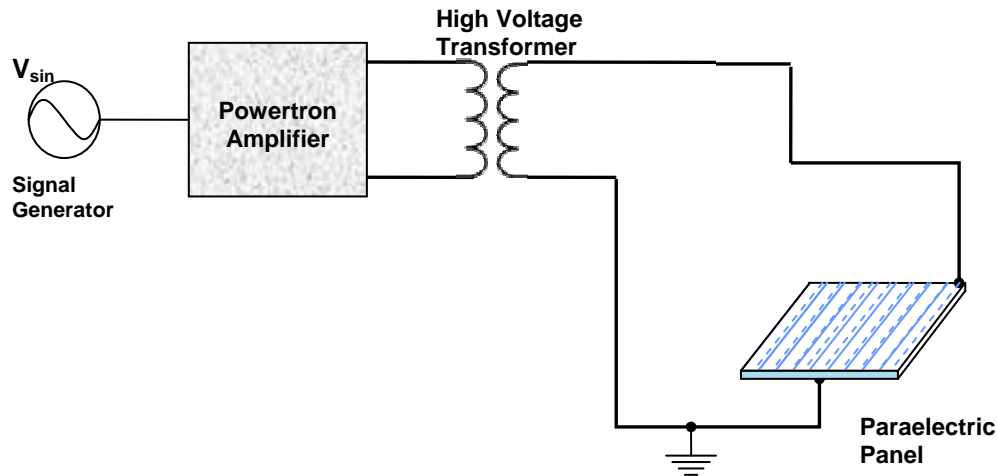


Figure 4.1: Paraelectric gas flow accelerator experimental setup

to do flow re-attachment studies. This un-impedance matched paraelectric system was used in most of our experiments. The detailed setup for flow attachment studies will be discussed in later sections. The signal generator combined with the Powertron<sup>TM</sup> power amplifier and the high voltage transformer generates a RF signal with a frequency up to 12 KHz and a voltage up to 10 KVrms. This produces OAUGD Plasma above the flat panel at each actuator. The voltage and frequency may be optimized to obtain the maximum flow velocity in the boundary layer.

The previous experience by our group has been that the OAUGD Plasma generated using a power supply impedance matched to the plasma actuators always performs better (more stable, less tracking, higher induced flow velocities) than a system without impedance matching. The task of impedance matching is to add a circuit composed of passive electrical parts (inductors, capacitors and/or resistors) between the RF power supply (or its output transformer) and the reactive load (i.e. the plasma panel) in such a way as to make the impedance of the whole load resistive. By eliminating the reactive power, one can increase the power factor of the whole load to nearly unity. By adjusting the impedance of the whole load to a purely resistive value, the maximum power output of the power supply can be delivered to the load. This also promotes the generation of a uniform plasma [30].

An impedance matched paraelectric flow acceleration system is shown in Figure 4.2 [30] The matching network is placed in parallel with the plasma reactor and close to the transformer output, so the stray capacitance of the cables between the transformer and the plasma reactor can be included in the reactor capacitance and matched by the

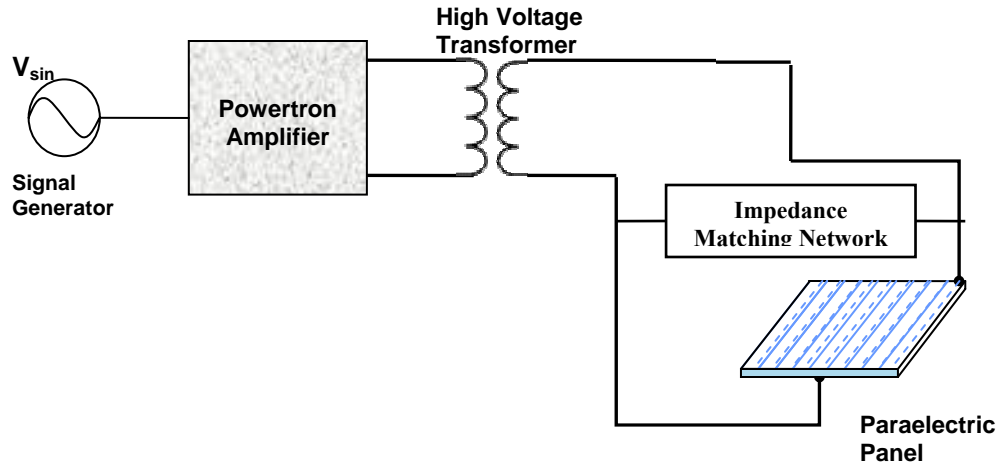


Figure 4.2: Impedance matched paraelectric gas flow accelerator

matching network. By adjusting the resistance in the impedance matching network, the voltage fed to the panel can be maintained at the same level at different driving frequencies.

## 4.2 Development of a Polyphase Power Supply

Many components are required to produce a polyphase power input to a linear array of plasma actuators [31]. Figure 4.3 shows the major components of the polyphase power supply system used for this thesis. The system consists of three stages: Stage I – a polyphase signal generator; Stage II - power amplifier; and Stage III – high voltage transformers. As shown in Figure 4.3, Stage I produces four signals, the second through fourth each advanced by a phase angle of 45 degrees with respect to the previous phase. The output of the polyphase signal generator is supplied to Stage II, where the signals are amplified and output to Stage III. At this stage, the transformer provides the RF high

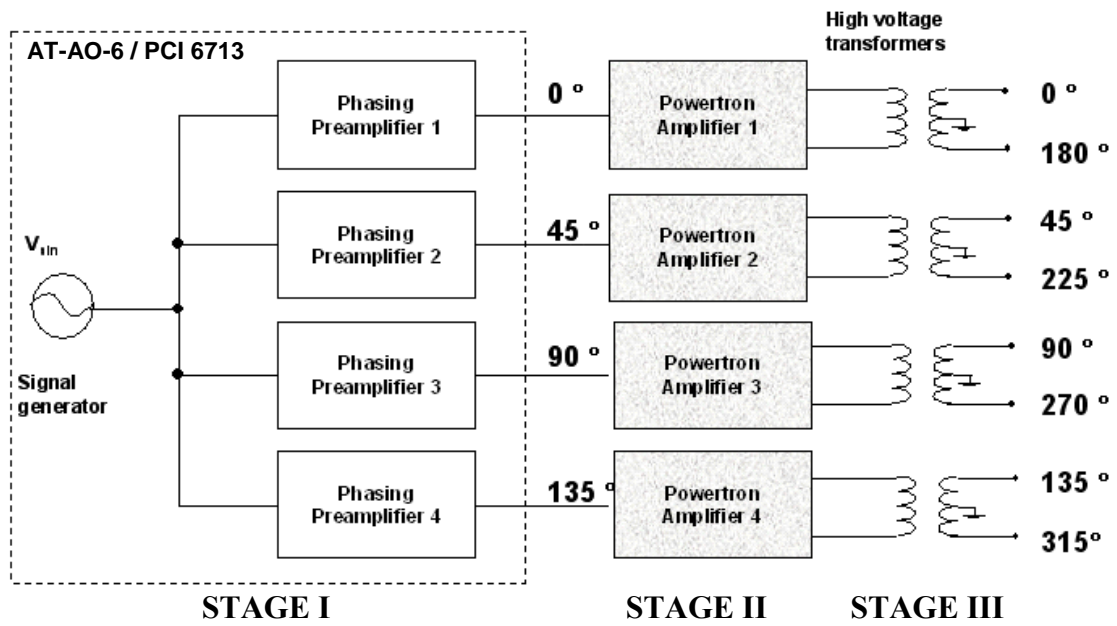


Figure 4.3: Polyphase power supply system schematic

voltage input to the plasma panel. Each stage is described in greater detail in the following sections.

#### **4.2.1 Polyphase Signal Generator**

A polyphase signal generator is required for the polyphase power supply. It can be constructed using analog or digital circuits, depending upon the operating requirements. Several methods were investigated and computer-based signal generation was found to be a satisfactory solution. This approach is shown in Figure 4.4. LabVIEW software, NI-DAQ driver software, a personal computer and PCI 6713/AT-AO-6 are the major components that were used to generate an analog output. These components are described in the following sub-sections.

##### *LabVIEW Software:*

One has several options to choose from when programming NI-DAQ and SCXI hardware. National Instruments application software, NI-DAQ, or register-level programming are available options to program the analog output card.

LabVIEW software features interactive graphics, a state-of-the-art user interface, and a powerful graphical programming language. The LabVIEW Data Acquisition VI Library, and a series of Virtual Instruments (VI) for using LabVIEW with National Instruments DAQ hardware are included with LabVIEW. LabVIEW is a program development environment, much like modern C or BASIC development environments. However, LabVIEW is different from these latter applications in one important respect. Programming languages like C or C++ normally use a text-based approach to create lines of code, while LabVIEW uses a graphical programming language called as ‘G’, to create programs in block diagram form [32].

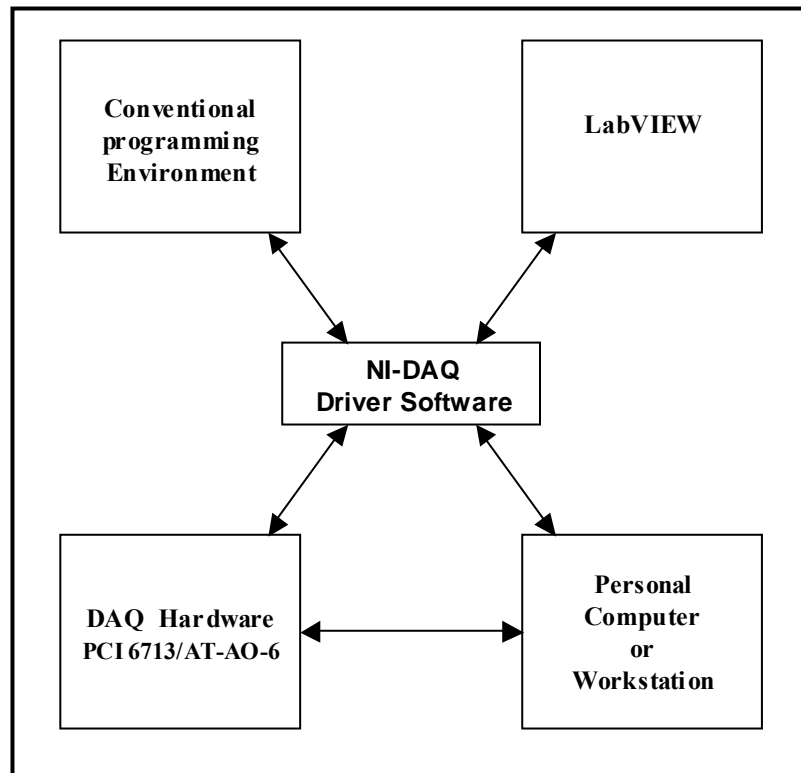


Figure 4.4: Polyphase signal generator schematic

LabVIEW is a general-purpose programming system with extensive libraries of functions for any programming task. LabVIEW includes libraries for data acquisition, GPIB and serial instrument control, data analysis, data presentation, and data storage. LabVIEW also includes conventional program development tools, so one can set breakpoints, animate the execution to see how data passes through the program, and single-step through the program to make debugging and program development easier. LabVIEW programs are called virtual instruments (VIs) because their appearance and operation can imitate actual instruments. However, the functions and operation of the VIs are similar to the functions of conventional language programs.

Several VIs were written to obtain our desired polyphase waveform with  $45^\circ$  phasing. The front panel designed for the control and operation of the polyphase signal generator is shown in Figure 4.5. We can generate four independent waveforms with  $45^\circ$  differential phasing. The amplitude and offset can be changed independently for each of the polyphase signals, or they can all be changed simultaneously by a single control.

The frequency of the signals is a key parameter, the setting of which should be explained in detail. As shown in Figure 4.5, the update rate is changed in order to change the frequency of operation. The green button located on the top of the front panel is used to reverse the phasing of the polyphase signals during peristaltic flow acceleration. The blue button located at the bottom of the control panel is used for shutdown of the whole system during emergency conditions. Another interesting feature of this virtual instrument, not used in the experimental program, is that waveform shape of each signal can be changed separately. For example, we can generate a step waveform with  $45^\circ$  phasing between the signals.

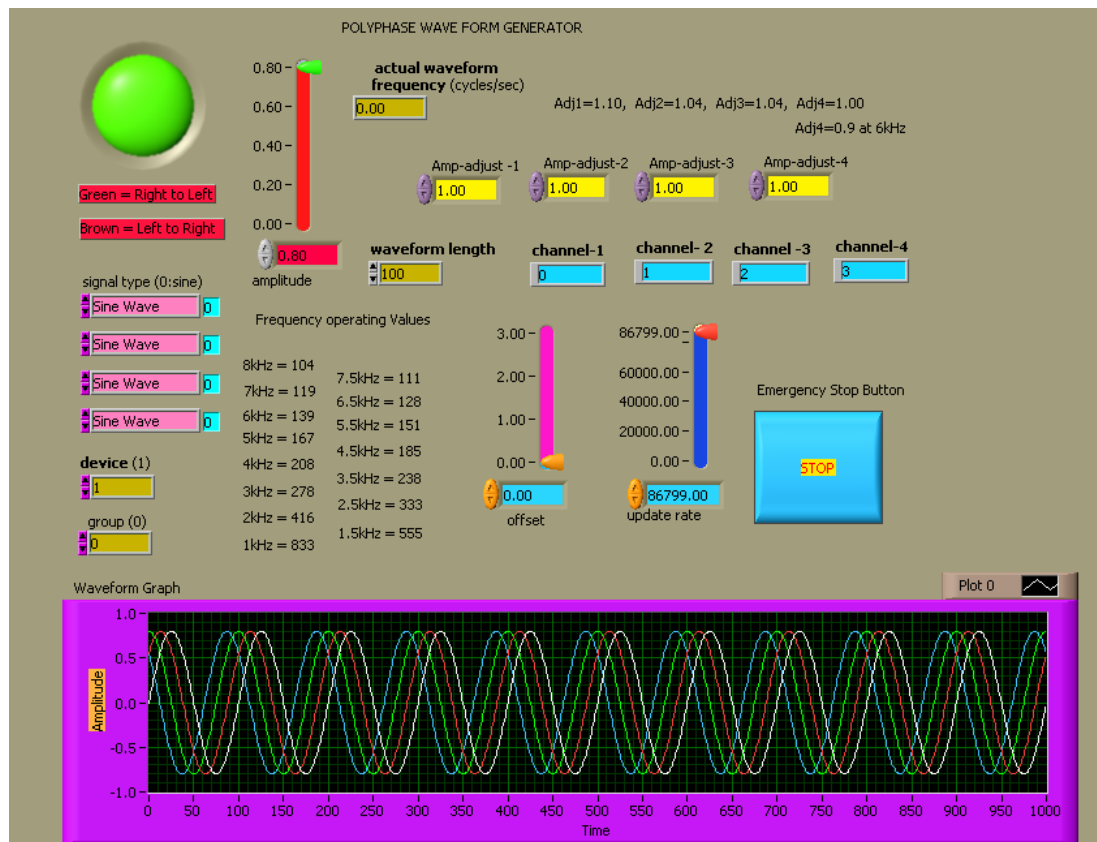


Figure 4.5: Labview polyphase generator program, front panel

#### *NI-DAQ Driver Software:*

The NI-DAQ driver software has an extensive library of functions that one can call from LabVIEW software. These library functions include routines for analog input (A/D conversion), buffered data acquisition (high-speed A/D conversion), analog output (D/A conversion), waveform generation (timed D/A conversion), digital I/O and many other functions [32].

The basic functions of the NI-DAQ drivers are shown in Figure 4.4. The NI-DAQ drivers stand as an interface between the personal computer or workstation running the Labview software and the PCI 6713/AT-AO-6 analog output cards. NI-DAQ also addresses internally many of the complex control issues between the computer and the DAQ hardware such as programming interrupts and DMA controllers. NI-DAQ maintains a consistent software interface among its different versions so that one can change platforms with minimal modifications to the code.

#### *DAQ Hardware: AT-AO-6 / PCI 6713:*

Data acquisition (DAQ) hardware is the part of the power supply system that actually generates the desired analog output from the workstation. Two types of hardware were used; AT-AO-6 and PCI 6713. The National Instruments AT-AO-6 is a high performance, 12 bit analog output board for PCs and workstations. It has 8 analog output channels and is capable of generating output at rates up to 300 KS/sec. The hardware and pin diagram are shown in Figure 4.6. The voltage levels of the AT-AO-6 card are shown in Table 4.1. The single channel output from the AT-AO-6 card looks approximately sinusoidal at frequencies up to 10 KHz. However, if four channels are

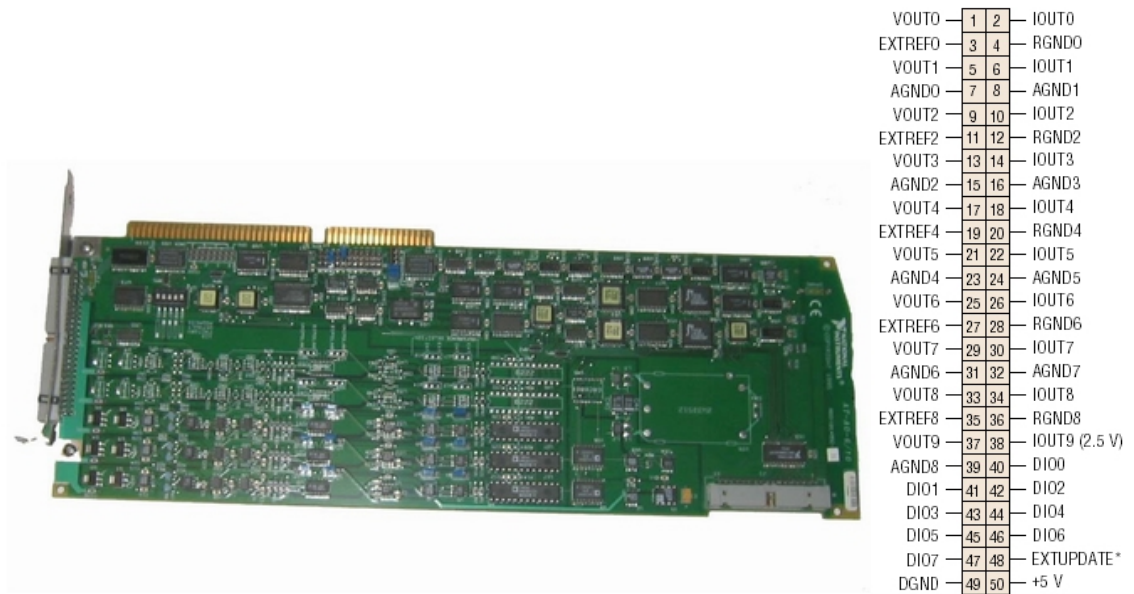


Figure 4.6: AT-AO-6 hardware and pin diagram

Table 4.1: AT-AO-6 hardware voltage levels

Level	Minimum	Maximum
Input Low Voltage	0 V	0.8 V
Input High Voltage	2.2 V	5.25 V
Output Low Voltage	—	0.5 V
Output High Voltage	2.4 V	—

used simultaneously at high output rates (i.e. at higher frequency) the output appears stair-cased. This stair-casing introduces higher harmonics to the power supply system that may generate overheating of the solid state devices in the power amplifier and heating of the high voltage transformer core. The stair-cased waveform is shown in Figure 4.7. To avoid this stair-casing effect or limitation to a comparatively low output frequency, the PCI 6713 is used instead.

The PCI 6713 device contains eight lines of digital I/O for general-purpose use. Each line can individually be software-configured for either input or output. At system startup and reset, the digital I/O ports are all high impedance. It also features a 12 bit digital to analog converter per channel, with update rates up to 1 mega sample/s/channel for analog outputs. This card is capable of producing higher update rates than the AT-AO-6 card. The output from the four channels of this card at frequencies above 5 kHz is no longer stair-cased. A digital image of the card and the pin diagram is shown in Figure 4.8. Table 4.2 shows the voltage levels of the PCI 6713 analog output card. The I/O connector for the 6711/6713 device has 68 pins and the analog output signals are DAC<0..7>OUT, AOGND, and EXTREF. AOGND is the ground reference signal for the analog output channels. All analog output channels as well as EXTREF are referenced to AOGND.

#### **4.2.2 Power Amplifier and Transformer**

The four signals, each advanced at a phase angle of  $45^\circ$  with respect to the previous channel, are produced by the polyphase signal generator and supplied to the RF power amplifiers. Each RF power amplifier has an input range of 0 to 2.5 volts peak-to-peak and a gain of 110 to 130 depending on the level of amplification. A digital image of

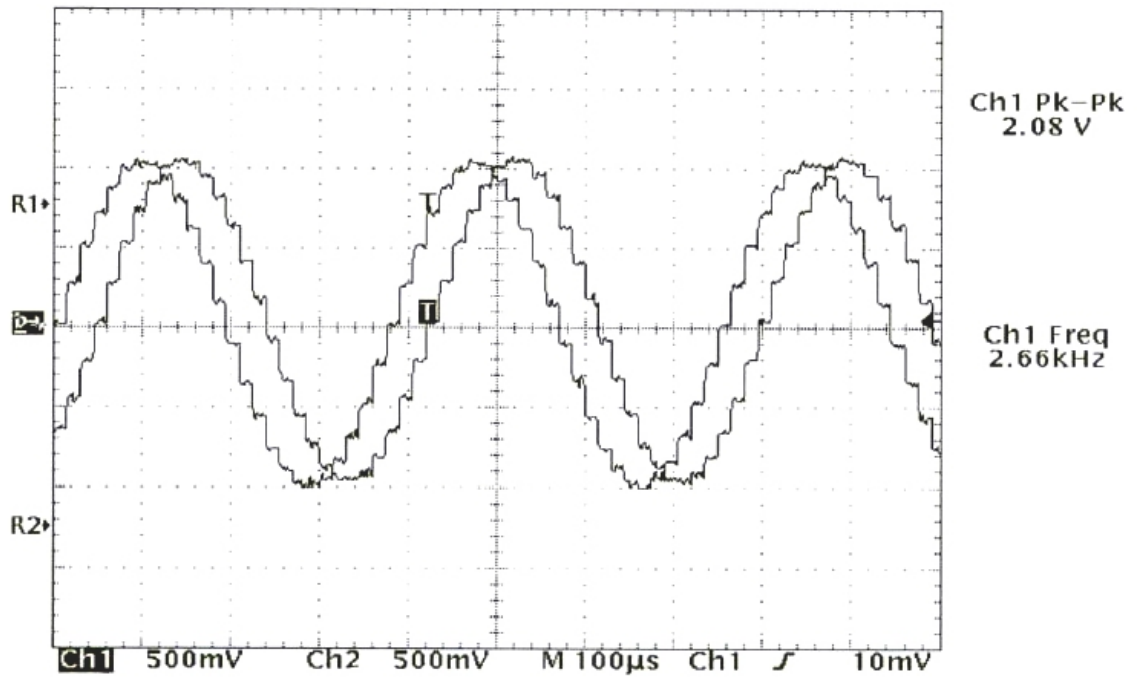
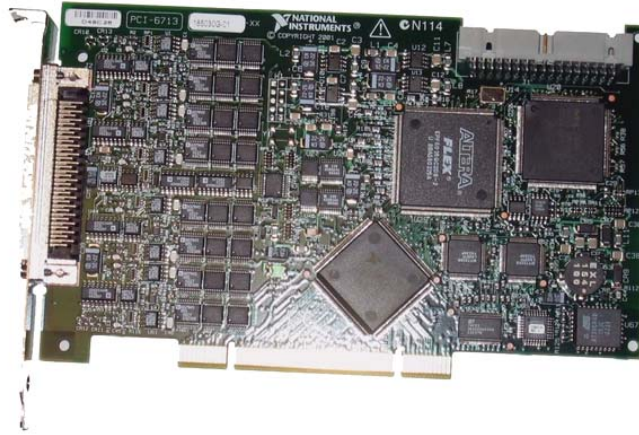


Figure 4.7: A staircase signal generated by the AT-AO-6 card at 2.66 kHz



A0GND	34	68	NC
NC	33	67	A0GND
A0GND	32	66	A0GND
A0GND	31	65	DAC7OUT1
DAC6OUT1	30	64	A0GND
A0GND	29	63	A0GND
DAC5OUT1	28	62	NC
A0GND	27	61	A0GND
A0GND	26	60	DAC4OUT1
DAC3OUT	25	59	A0GND
A0GND	24	58	A0GND
A0GND	23	57	DAC2OUT
DAC0OUT	22	56	A0GND
DAC1OUT	21	55	A0GND
EXTREF	20	54	A0GND
DIO4	19	53	DGND
DGND	18	52	DIO0
DIO1	17	51	DIO5
DIO6	16	50	DGND
DGND	15	49	DIO2
+5 V	14	48	DIO7
DGND	13	47	DIO3
DGND	12	46	NC
PF10	11	45	EXTSTROBE
PF11	10	44	DGND
DGND	9	43	PF12
+5 V	8	42	PF13/GPCTR1_SOURCE
DGND	7	41	PF14/GPCTR1_GATE
PF15/UPDATE	6	40	GPCTR1_OUT
PF16/WFTRIG	5	39	DGND
DGND	4	38	PF17
PF19/GPCTR0_GATE	3	37	PF18/GPCTR0_SOURCE
GPCTR0_OUT	2	36	DGND
FREQ_OUT	1	35	DGND

Figure 4.8: PCI 6713 hardware and pin diagram

Table 4.2: PCI 6713 hardware voltage levels

Level	Minimum	Maximum
Input Low Voltage	0 V	0.8 V
Input High Voltage	2.0 V	5.0 V
Output Low Voltage	—	0.4 V
Output High Voltage	4.35 V	—

the power amplifier is shown in Figure 4.9 and its rating is shown in Table 4.3. The power amplifier consists of 24 pairs of P-type and N-type MOSFET transistors mounted on a heat sink and cooled by two fans. The high voltage transformer casings are shown in Figure 4.9, and their ratings are shown in Table 4.3. The output voltage desired is more than 5 kV<sub>rms</sub>, and the frequency response up to 10 kHz. Transformers with serial connection and the center tap grounded are used to generate 5 kV<sub>rms</sub>. This arrangement gives two voltage outputs with a 180° phase difference between them. The transformers are immersed in a mineral oil bath in order to suppress high voltage breakdown during high voltage spikes associated with transients and radio frequency interference.

#### **4.2.3 Peristaltic Experimental Setup**

All major components of the peristaltic experimental apparatus were explained in earlier sections. Figure 4.10 shows the phase connection diagram of a peristaltic (or traveling wave) gas flow accelerator panel. Figure 4.11 shows a peristaltic panel installed in the 7 X 11 Inch Low Speed Wind Tunnel at NASA Langley Research Center, operating at 3.5 kV<sub>rms</sub> and 3 kHz.

#### **4.3 Smoke Wire Flow Visualization System**

The components of the smoke flow visualization system are diagrammed in Figure 4.12. The system consists of two major assemblies, one for producing the smoke trails and the other for capturing the smoke trails on a digital camera.

The 25 micron diameter stainless steel smoke wire is located 15 mm upstream from the first plasma actuator on the panel, at the panel midline. A small weight is hung at the end of the smoke wire to keep it straight and vertical. Another important reason for the weight is to pull the smoke wire out of the wind tunnel if the wire breaks due to

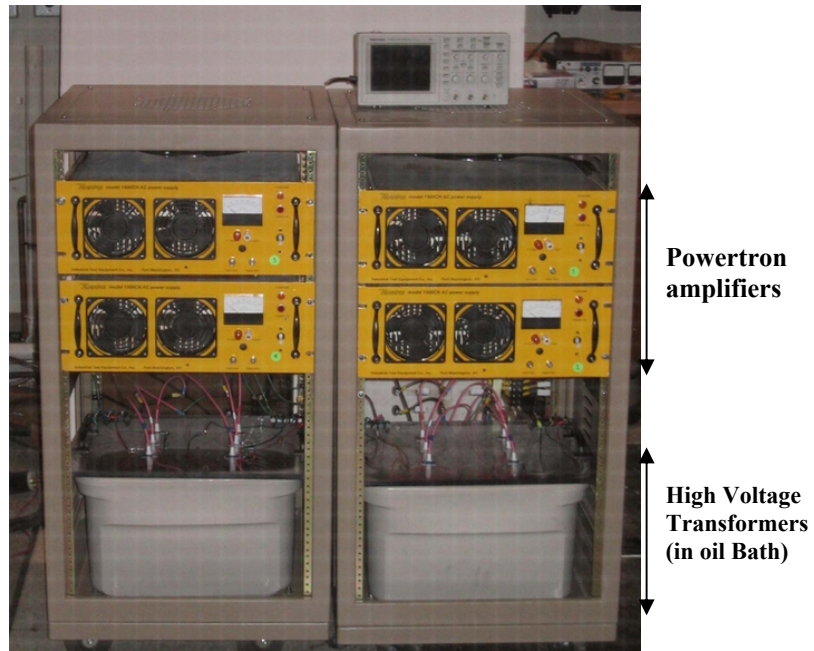


Figure 4.9: Picture showing power amplifiers and transformers.

Table 4.3: Rating of the power amplifier and high voltage transformer

Powertron Amplifier (4)	High Voltage Transformer (4)
<u>Manufacturer:</u> Industrial Test Equipment Co. , Inc <u>Model:</u> 1500CN AC Power Supply <u>Gain</u> $\approx$ 110 to 130 <u>Frequency range:</u> 0. 5 to 20 kHz	<u>Manufacturer:</u> Industrial Test Equipment Co. , Inc <u>Model:</u> VT-35/RM-109 <u>Maximum output voltage:</u> 10 kV

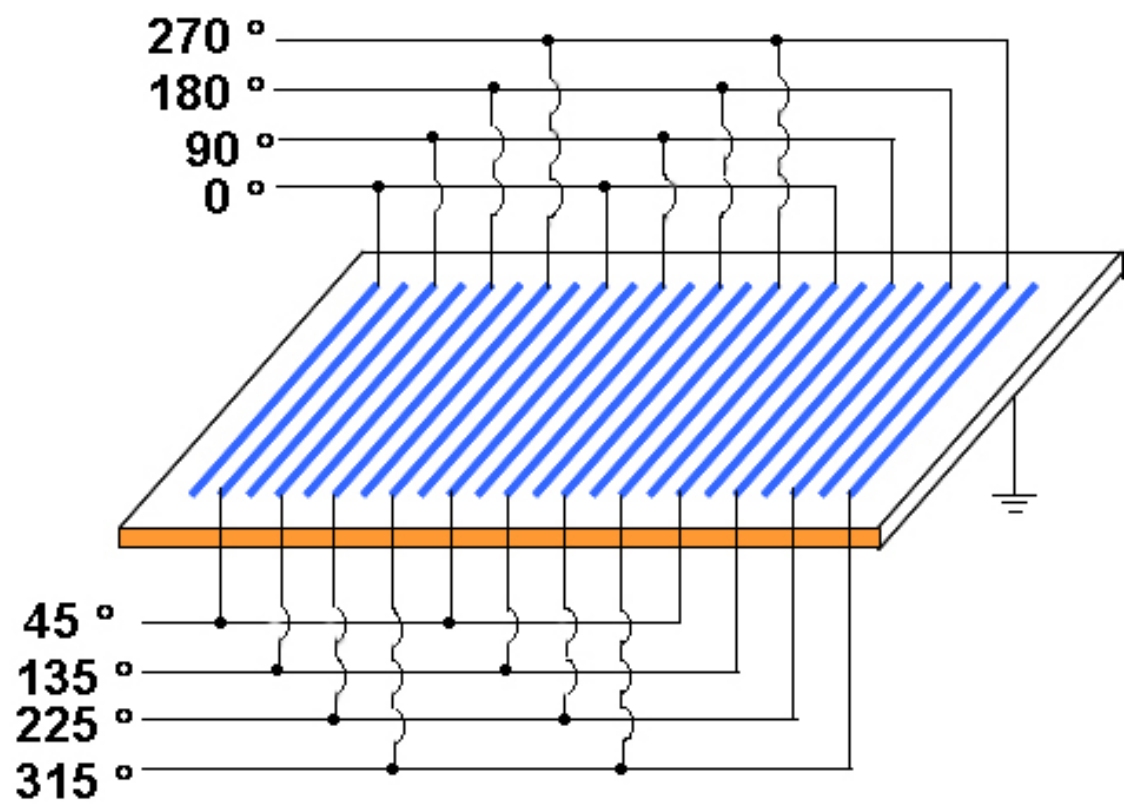


Figure 4.10: Phase connection diagram of plasma actuators for a peristaltic accelerator panel.

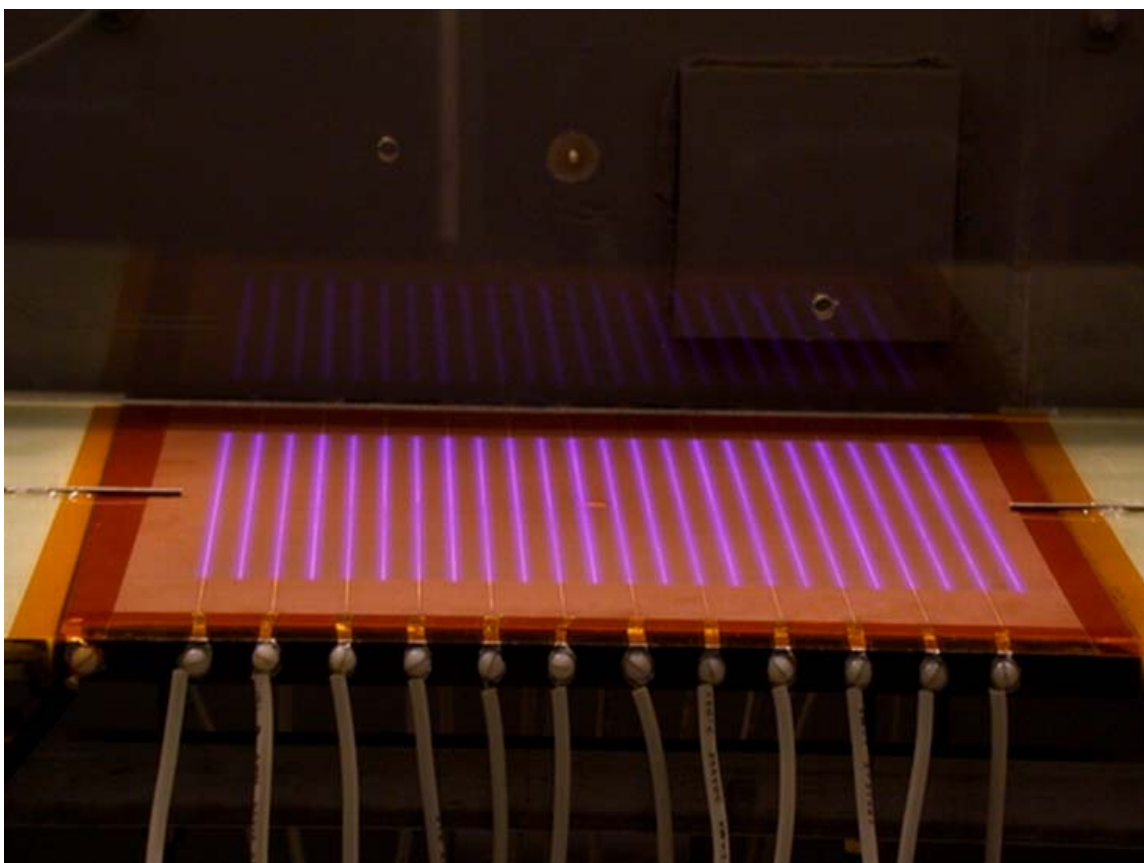


Figure 4.11: Peristaltic accelerator panel mounted in the 7 X 11 Inch Low Speed Wind Tunnel at NASA Langley Research Center, operating at  $3.5 \text{ kV}_{\text{rms}}$  and 3 kHz.

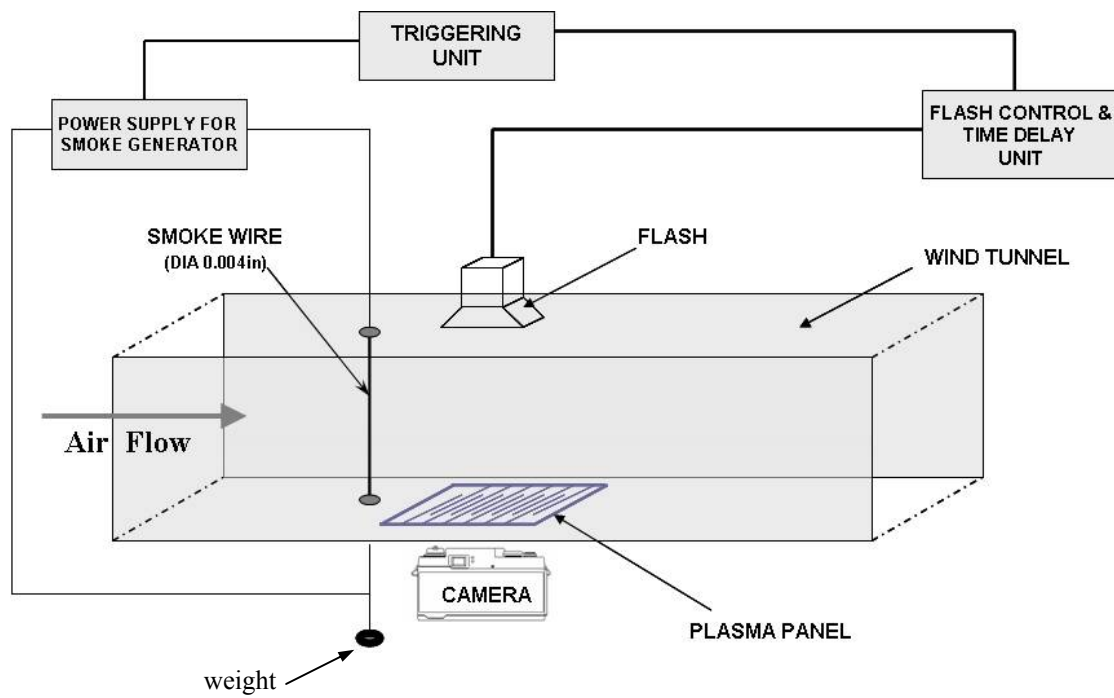


Figure 4.12: Smoke flow visualization system schematic.

overheating. If left in the test section, the stainless steel wire might short circuit the panel. Before each run, the wire is coated with light mineral oil, the surface tension of which causes the oil to form approximately equally-spaced beads along the length of the wire.

The triggering unit initiates both the smoke wire firing system and the strobe system. The triggering unit first heats the smoke wire with a current pulse, and after a set delay, the strobe lamp is energized. The delay is set such that the smoke trails are illuminated by the strobe light. The delay depends on the type of oil used, the airflow speed in the wind tunnel, and the voltage used for the smoke wire power supply. The delay is varied until the best image of the smoke trails is captured by the camera. The delay is usually set around 2.5 to 3.0 msec. The digital camera is operated with its shutter open. The timing is indicated by the diagram in Figure 4.13 [29]. The preset delay is such that the required image is captured by the digital camera.

With the plasma power supply and wind tunnel flow speed set at the desired levels, a current pulse is sent through the smoke wire, which heats the wire and causes the beads of mineral oil to vaporize and produce approximately evenly spaced vertical smoke trails.

Figure 4.14 shows a Kapton<sup>TM</sup> plasma panel mounted on a NACA 0015 airfoil in the wind tunnel for flow separation studies. The smoke lines flow both below and above the airfoil. One such example is shown in Figure 4.15 and on such images flow separation studies are based. Figure 4.16 shows an example in which a flat panel covered with plasma actuators at the bottom of the image is used, instead of an airfoil.

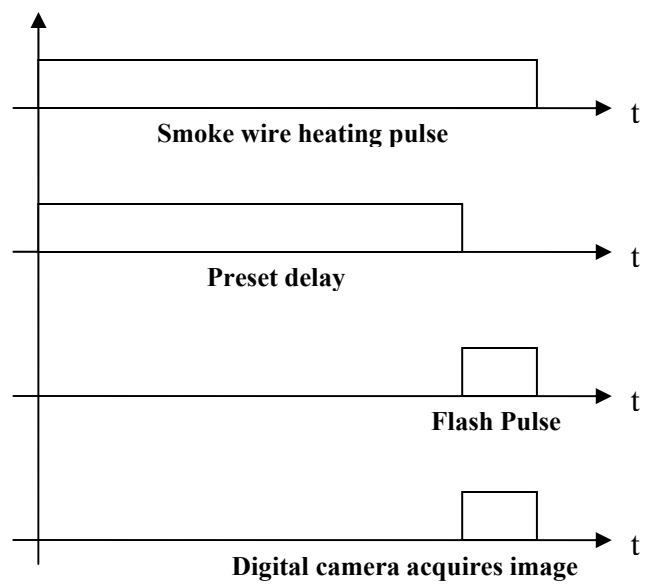


Figure 4.13: Timing diagram for the trigger and time delay unit.

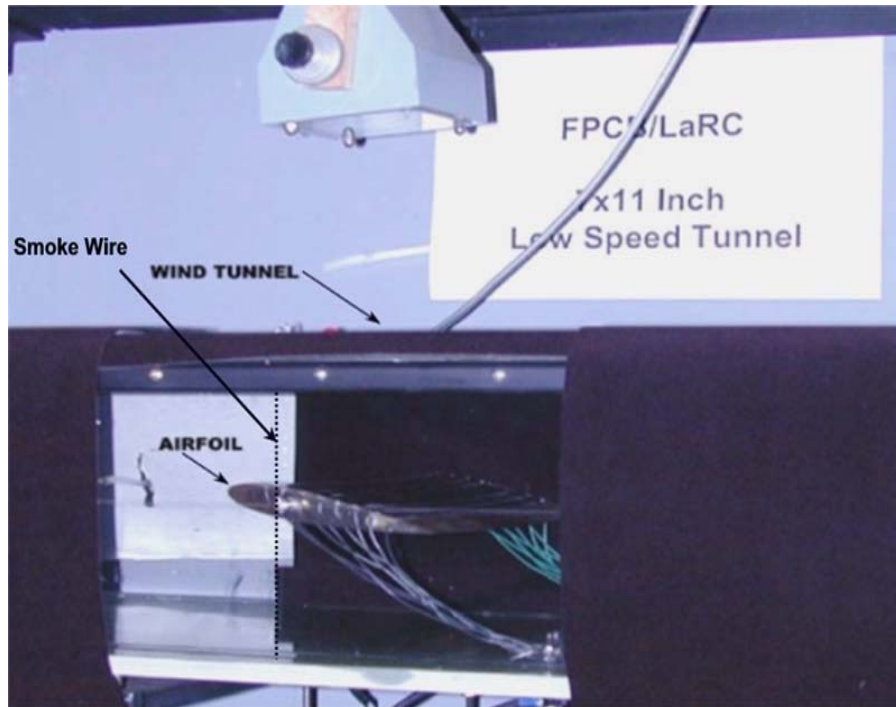


Figure 4.14: The NACA 0015 airfoil with OAUGDP™ electrode strips mounted in the NASA Langley Research Center's 7 X 11 Inch Low Speed Wind Tunnel for smoke flow tests.

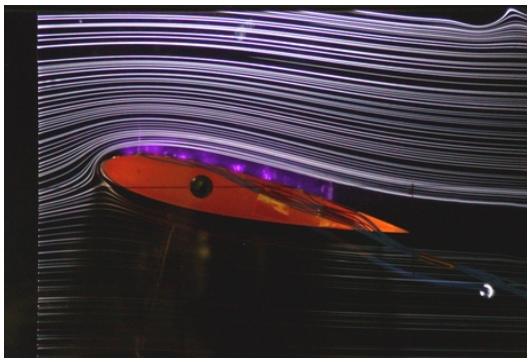


Figure 4.15: Smoke trails around a NACA 0015 airfoil.

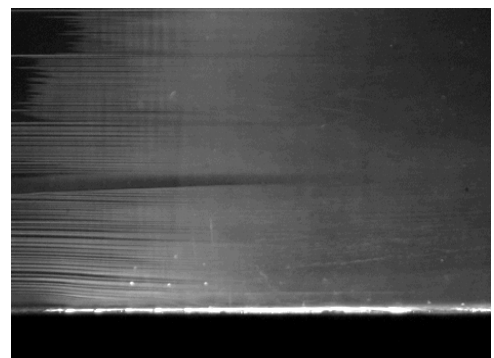


Figure 4.16: Smoke trails above a flat panel covered with plasma actuators.

#### 4.4 Pitot Probe System

The Pitot probe system contains two kinds of connections: one is the pneumatic connections, and the other is the IEEE 488(GPIB) electrical connections. The over-all Pitot probe system is shown in Figure 4.17. In the Pitot probe transducer, pressure is measured with an electronic silicon pressure sensor with a full scale differential pressure rating of  $\pm 10$  mmHg. The accuracy of the sensor was  $\pm 0.004$  mmHg, combined span, linearity and hysteresis. The maximum Pitot pressure was in the range of 0.01-0.02 mmHg, indicating the possibility of significant absolute error in the measured velocities. The sensitivity of the system and the zero-point offset accuracy were such that the minimum velocity that could be measured was 0.5 meters/sec.

As shown in Figure 4.17 there are three digital pressure gauges, two of them to measure the differential pressure inside the wind tunnel, and the third a [25] barometric pressure gauge. These pressure gauges are connected to a personal computer using GPIB connections. A digital step motor controller is used to operate a Pitot probe actuator capable of moving along three orthogonal axes. The step motor controller is also connected to the computer through an IEEE 488 GPIB connection. All this digital equipment is connected to a computer and is managed by NI measurement and automation software.

The process of velocity profile measurement is programmed using software called HPVEE. This software is similar to LabVIEW and is programmed in a graphical environment. Before each run, inputs such as the axis of the probe movement, number of steps or measurements to be taken, distance to be moved, length of each step, and number of data points to be averaged are programmed into the system. The data taken for each

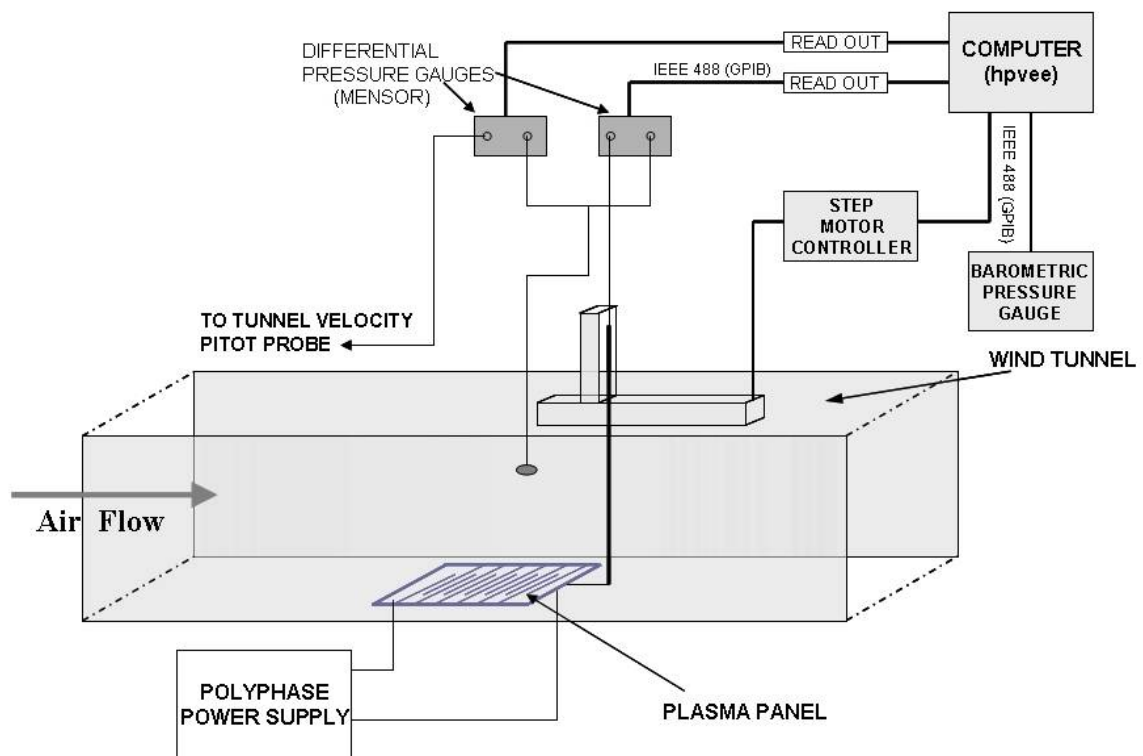


Figure 4.17: Pitot probe system schematic

run is stored as a text file. The text file has all the details of pressure, steps, distance and other data. The data from the text file is later plotted to visualize the results.

On a comparative basis, the Pitot tube data are useful for identifying qualitative trends. The pressure gage zero was checked and adjusted frequently, and the data were averaged to reduce random reading fluctuations. In addition to the sensor accuracy, the Pitot probe's angular sensitivity is an important issue for other than laminar flow measurements. In the case of flow at an angle to the probe, the measured Pitot velocity could be as much as 50% lower than the actual velocity vector magnitude. For turbulent flow measurements, other error sources such as wall interference and probe position accuracy are small compared to the much larger scale and angle effects. Overall, the interpretation of the Pitot velocity data should be on a qualitative, comparative basis for plasma-on and plasma off conditions at the same test model, tunnel free stream velocity, and probe position.

## 5. EXPERIMENTAL RESULTS AND DISCUSSION

### 5.1 Smoke Flow Visualization

Smoke flow visualization studies were done to observe the effects of the plasma actuators on the boundary layer. In this section flow visualization results from both the airfoil and flat panel configurations are presented.

#### *Boundary Layer Studies:*

When two solids interact, forces are transmitted between them at the point of contact. However, when a solid interacts with a fluid, the situation becomes more complex because the fluid can change its shape. Also, the fluid can flow around the body and maintain physical contact with the solid object at all points. If the fluid is in motion, the velocity will have different values at different locations around the body. The local pressure is related to the local velocity, so the pressure also varies around a closed surface enclosing the body, and a net force (lift, drag) can be produced. Integrating the pressure perpendicular to the surface of the solid over its area produces the net force. The net force opposite to the gravity vector is called the lift. The net force opposite to the flow direction is called the drag, and along the flow direction is called propulsion.

Lift can be generated by a wide variety of objects, including airplane wings, rotating cylinders, spinning balls, and flat plates. Lift is the force that supports an aircraft in the air. Lift can be generated by any part of an airplane, but most of the lift on a normal airliner is generated by the wings. In our research we used both an airplane wing (or airfoil) and flat plates. The airfoil in Figure 5.1 shows the lift and drag vectors, and also the angle of attack referred to the horizontal.

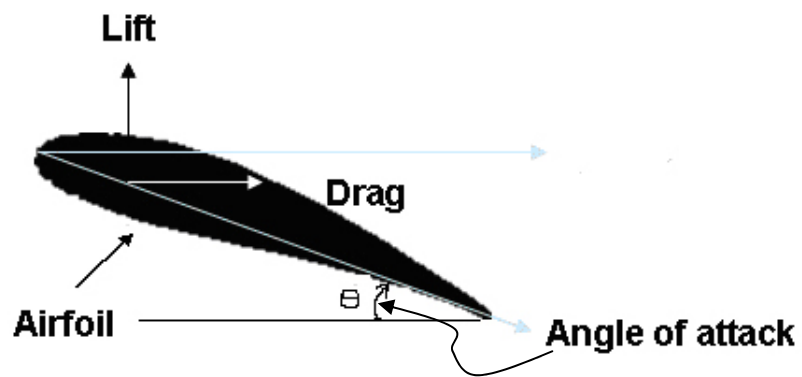


Figure 5.1: Airfoil showing aerodynamic forces.

Lift is generated only when there is relative motion between an object and the surrounding fluid. Most wind tunnel experiments are conducted by keeping the object (airfoil) fixed, and moving the fluid (air). The major factors that affect the lift of an airfoil are its shape and its relative velocity in the fluid.

As an object moves through a fluid, or as a fluid moves past an object, the molecules of the fluid near the object are displaced and move around the object. The magnitude of the aerodynamic forces generated, depends on the shape of the object, its speed, and the mass density, viscosity and compressibility of the fluid. As fluid moves past an object, the molecules next to the surface adhere to it. The molecules just above the surface are slowed down by their collisions with the molecules sticking to the surface. These molecules in turn slow down the flow just above them. The farther one moves away from the surface, the more attenuated is the influence of the object surface. This creates a thin (boundary) layer of fluid near the surface in which the velocity changes from zero to the free stream value. The flow within the boundary layer is very important for many problems in aerodynamics.

Boundary layers may be either laminar (layered,  $\nabla \times \mathbf{v} = 0$ ), or turbulent (disordered,  $\nabla \times \mathbf{v} \neq 0$ ) depending on the value of the Reynolds number. For lower Reynolds numbers, the boundary layer is laminar and the stream-wise velocity changes uniformly as one moves away from the wall, as shown on the left side of Figure 5.2. For higher Reynolds numbers, the boundary layer is turbulent and the stream-wise velocity is characterized by unsteady (changing with time) turbulent flows inside the boundary layer, illustrated on the right-hand side in Figure 5.2.

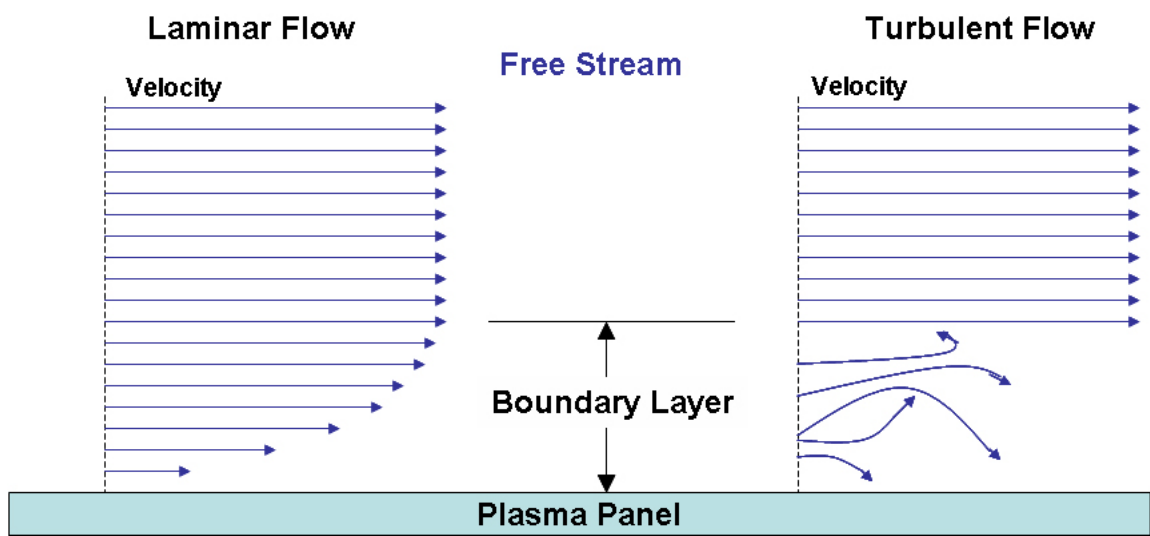


Figure 5.2: Boundary Layer.

In our investigations, a hot wire anemometer was used to make sure the flow regime was laminar.

### **5.1.1 Preparation of OAUGDP™ Airfoil**

Figure 3.9a shows the Kapton™ plasma panel with polyamide dielectric material. The panel is flexible and can be made to conform the airfoil surface. The panel shown has an asymmetric paraelectric plasma actuator electrode configuration. To run the flow separation experiments, the Kapton™ panel was mounted on the upper surface of a NACA 0015 airfoil. This airfoil is more prone to flow separation effects than other airfoil configurations. The testing configuration of the airfoil is shown in Figure 5.3. To get the best results, the plasma panel should conform exactly to the surface of the airfoil. Even though the Kapton™ panel is flexible, obtaining adequate smoothness of the airfoil is a tedious task.

A small recessed groove was milled on top of the wing section, the depth of which is equal to the thickness of the Kapton™ plasma panel. Before bonding the panel to the airfoil, the copper electrodes on the top and bottom of the Kapton™ dielectric panel must be connected by soldering thin wires to the electrodes on both sides of the dielectric without changing the smoothness or shape of the airfoil surface. The Kapton™ panel assembly is bonded to the airfoil using a special very thin adhesive tape (3M).

While bonding the panel to the airfoil, one must take care not to leave any air bubbles between the panel and the airfoil. Such bubbles can cause dielectric breakdown at higher voltages. When this airfoil is used in the wind tunnel to take flow separation data, the airfoil surface should be free of contaminants. Most such contaminants originate from the smoke wire. Between runs the airfoil surface is cleaned thoroughly.



Figure 5.3: Digital image of the airfoil mounted with plasma actuator panel in place. Chord length is 12.7 cm. A 1.07mm diameter trip wire is shown mounted near the leading edge. This trip wire is used only for some specialized tests reported later in the thesis.

### 5.1.2 Paraelectric Flow Re-attachment

Controlled re-attachment of separated flows over lifting surfaces at moderate and high angles of attack using plasma actuators is demonstrated in this section. The airfoil described in the previous section is installed in the wind tunnel as shown in Figure 4.14. Several experiments were performed to demonstrate the effectiveness of paraelectric plasma actuators to reduce the flow separation associated with the airfoil.

The performance of almost all aircraft is influenced by laminar flow separation bubbles that may occur at low Reynolds numbers. This separation bubble is caused by a pressure rise along the surface, which pushes the laminar boundary layer away from the curved airfoil surface. The boundary layer separates from the airfoil surface almost tangentially, forming a wedge-shaped region between the airfoil and the free-stream smoke trails, called the flow separation region. This flow separation region causes the airfoil to “stall” (i.e. fail to generate lift)

The flow visualization system described in Section 4.3 was used to generate the desired smoke trails. A Kapton<sup>TM</sup> panel with a paraelectric asymmetric electrode configuration is used for the experiments described below. Figure 5.4 shows a series of runs to assess the effects of angle of attack at low wind tunnel velocities. These data were taken with NACA airfoil # 0015, with OAUGDP<sup>TM</sup> panel #1, and a wind tunnel velocity of 2.85 meters/second. The left-hand column in Figure 5.4 shows the effect of angle of attack with the plasma off and the right-hand column shows the effect of angle of attack with 7 actuators energized ( actuator # 5 was disabled by a short circuit)

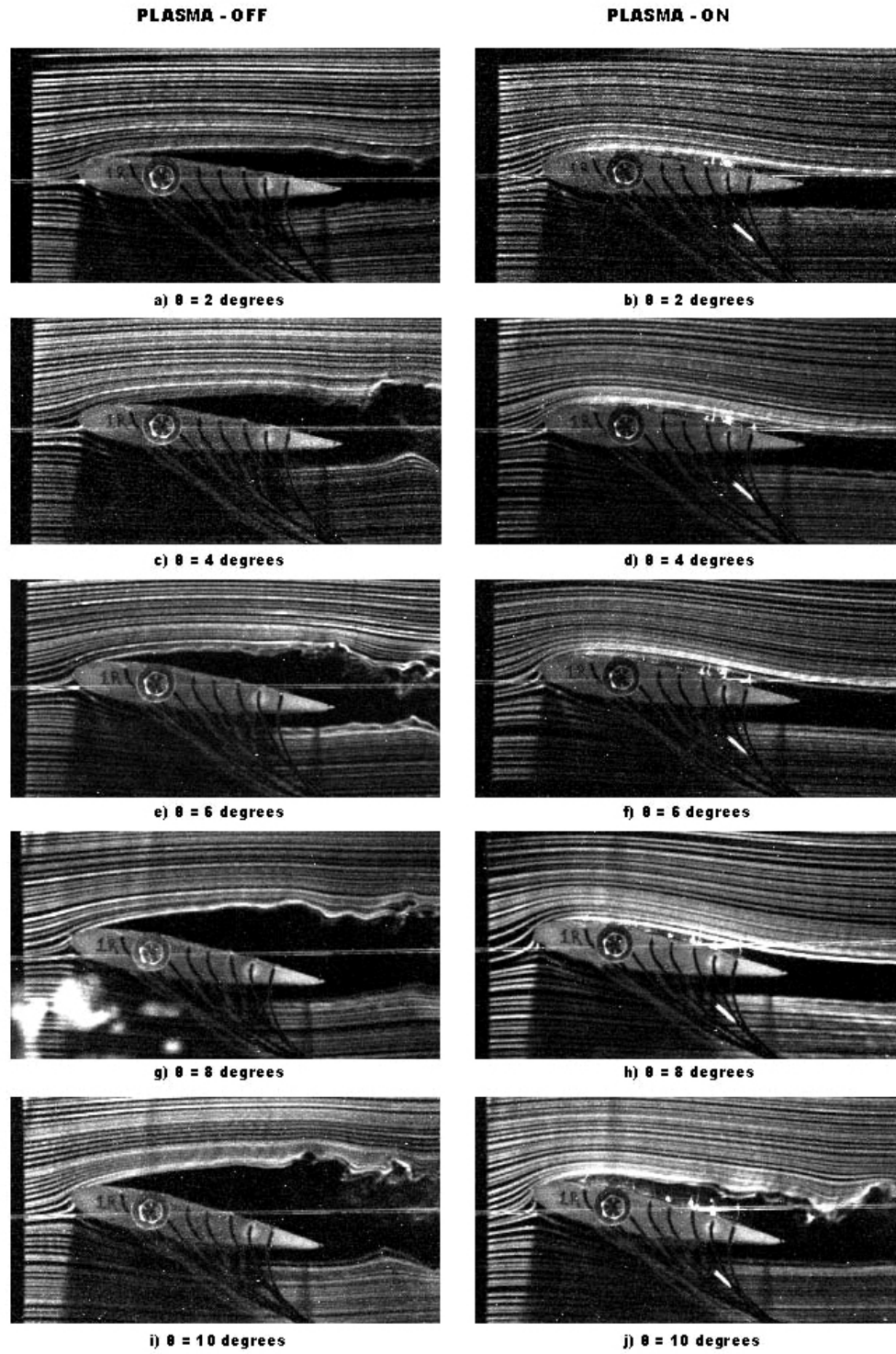


Figure 5.4: Effect of angle of attack with seven plasma actuators energized with 4.2 kV rms, 4.2 kHz and a wind tunnel speed of 2.85 m/sec.

at 4.2 kV rms and 4.2 kHz. The effect of the plasma is very apparent in these pictures.

The left-hand column of Figure 5.4 shows the airfoil at angles of attack from 2 degrees to 10 degrees with the plasma off. The thin line that runs through each picture marks the zero degree angle of attack with respect to the horizontal. Flow separation is evident at all angles of attack. As the angle of attack increases, the waviness of the air flow separation boundary, like the flapping of a flag, increases downstream of the airfoil. Such an instability is characteristic of greatly increased drag and the formation of a trail of vortices.

The right-hand column of Figure 5.4 shows the airfoil at the same angles of attack as previously, with 7 electrodes energized (1 to 4 and 6 to 8). For these conditions, flow separation and vortex formation are suppressed below an 8 degree angle of attack. The flow separation bubble formed at 10 degrees was not completely suppressed.

Figure 5.4 illustrates the effect of the plasma actuators in manipulating the boundary layer above the surface of the airfoil, but it does not identify the location of the electrode that is most responsible for suppressing flow separation. Figure 5.5 shows a series of runs to assess the effect on the flow of the location of the energized plasma actuators. The angle of attack is constant at 6 degrees. Data were taken with NACA airfoil # 0015 with OAUGDP™ asymmetric plasma actuators on a Kapton™ panel mounted on top of the airfoil and a wind tunnel velocity of 2.85 meters/second. The electrodes were energized at 4.5 kV rms and 3.5 kHz. Figure 5.5a shows the flow separation with the plasma off. The plasma actuators are progressively energized starting with actuator # 2.

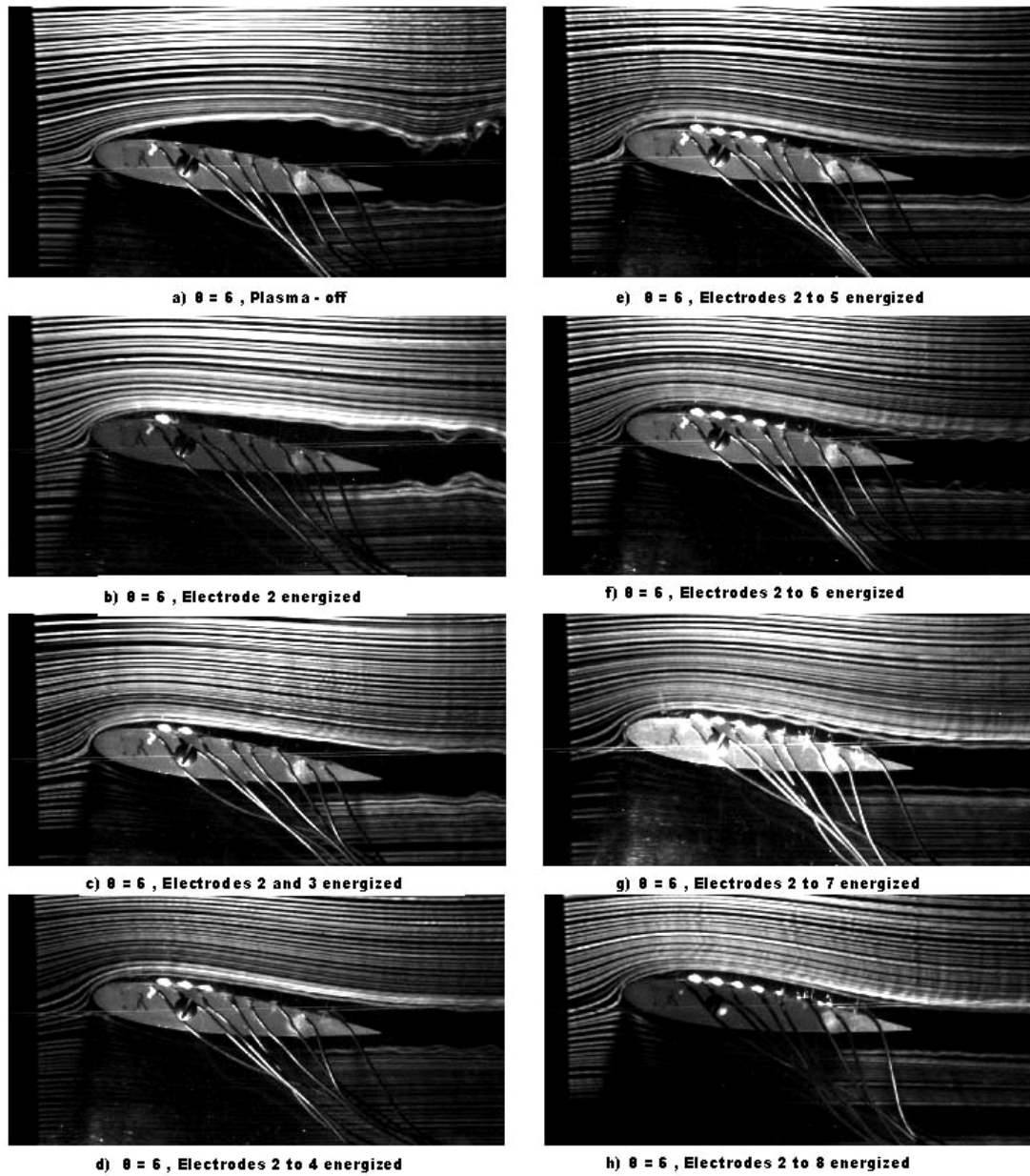


Figure 5.5: Effect of plasma location and number of plasma actuators energized. The angle of attack is  $6^\circ$ , electrodes operated at 4.5 kV rms, 3.5 kHz and a wind tunnel speed of 2.85 m/sec.

From Figure 5.5b it is evident that most of the re-attachment is due to electrode # 2, located near the leading edge of the airfoil (Electrode #1 was disabled by a short circuit). This single electrode did not completely eliminate the formation of vortices. As additional plasma actuators are energized, vortex formation (indicated by waviness in the flow separation boundary) is progressively reduced, and when all actuators (#2 to #8) are energized the “flapping” instabilities and vortex formation are virtually eliminated.

Figure 5.6 shows the effect of plasma actuators located at the trailing edge, compared to actuators located at the leading edge. The angle of attack is kept constant at 6 degrees. Data were taken with the same NACA 0015 airfoil with paraelectric OAUGDP™ plasma actuators and a wind tunnel velocity of 2.85 meters/second. The electrodes were energized by an RF voltage of 4.5 kV rms and 3.5 kHz. Figure 5.6a shows the airfoil with 7 actuators (#2 to #8) energized, and no flow separation; the actuators were progressively turned off starting with actuator # 2.

As the actuators were turned off one by one starting from the leading edge, their effect on the flow progressively decreased. When the actuators from # 2 to # 4 were off, the remaining actuators did almost nothing to the flow; there was no significant difference between the plasma off condition shown in Figure 5.6f, and the partially energized condition 5.6e.

Since the electrode that has most effect (i.e. the leading electrode) is known from previous runs, a series of runs were taken to assess the effect on the flow of angle of attack and the presence of an energized OAUGDP™ on actuator # 1 only. Data were

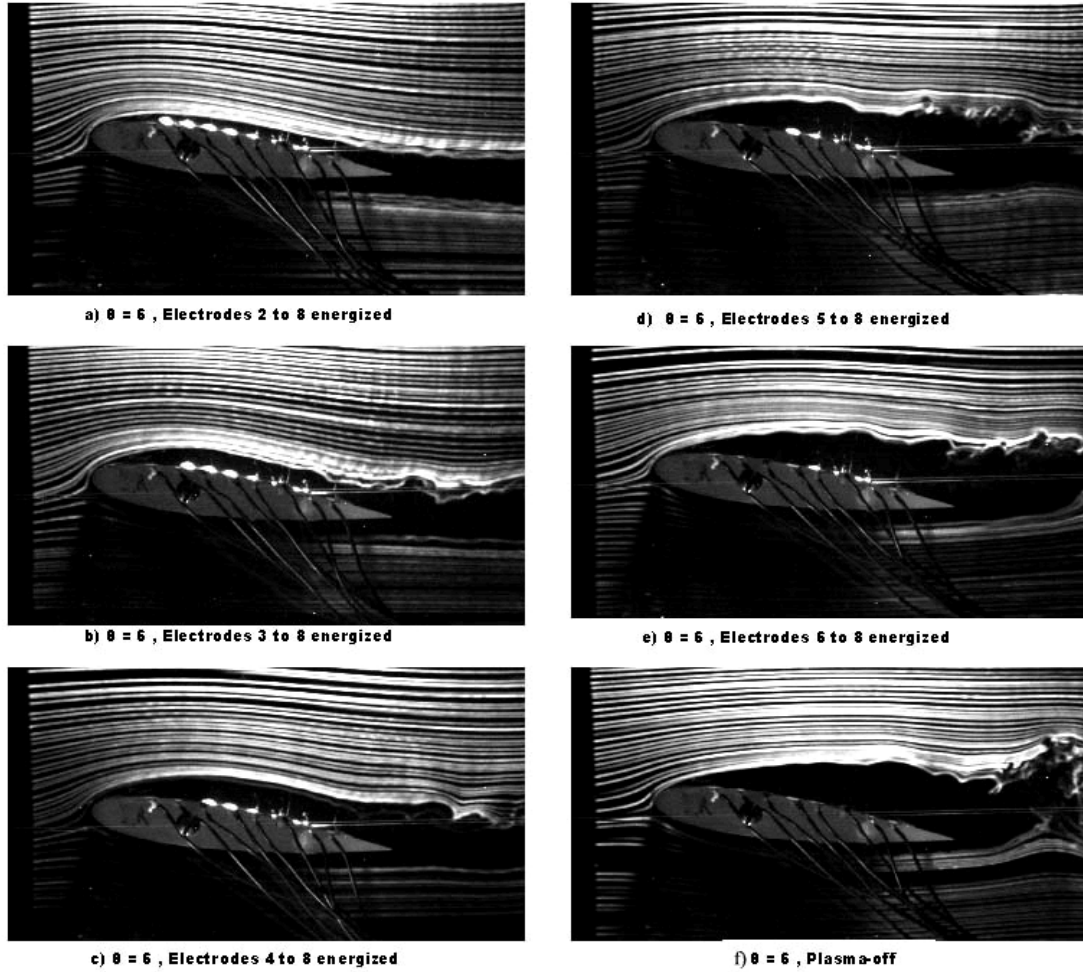


Figure 5.6: Effect of plasma actuator location and number of plasma actuators energized. The angle of attack is  $6^\circ$ , electrodes operated at 4.5 kV rms, 3.5 kHz, a wind tunnel speed of 2.85 m/sec.

taken with the same NACA 0015 airfoil with the Kapton<sup>TM</sup> OAUGDP<sup>TM</sup> paraelectric plasma panel and a wind tunnel velocity of 2.85 m/sec.

The left-hand column shows the effect of angle of attack with plasma actuator #1 off; the right-hand column shows the effect of angle of attack with only electrode #1 energized at 4.2 kVrms and 4.2 kHz. The single electrode at the leading edge of the airfoil was able to attach the flow until an 8 degree angle of attack, as shown in Figure 5.7j. Figure 5.7k shows the condition in which all eight plasma actuators were energized. It shows little difference from Figure 5.7j in which only one electrode is energized.

Figure 5.8 shows experimental runs taken to assess the effect of a trip wire on the flow. These data were taken to ascertain whether the slight thickness of the plasma electrode (cira 0.1 mm) might cause the effects discussed above. A 1.07 mm diameter trip wire was attached at the position of plasma actuator #1 and smoke trail flow field photographs were taken. Figure 5.8a shows the flow field when the plasma is off, but the trip wire present. Figure 5.8b shows the plasma off condition with no trip wire, and Figure 5.8c shows the flow field with only plasma actuator #1 energized, at 4.3 kV rms and at 4.2 kHz, and no trip wire. Comparing the results from these images, it is evident that plasma actuators and not flow tripping by the presence of electrode strips causes the above mentioned effects.

Figure 5.9 shows an airfoil mounted in the 7 X 11 inch Wind Tunnel with a 16 degree angle of attack, a wind tunnel velocity of 2.8 m/sec and all electrodes energized at 3.6 kV rms and 4.2 kHz. The OAUGDP<sup>TM</sup> plasma was able to attach the flow without any instability at this angle of attack. Figure 5.10 shows flow attachment at a higher wind tunnel velocity, 7.6 m/sec. The airfoil is at an 8 degree angle of attack with all

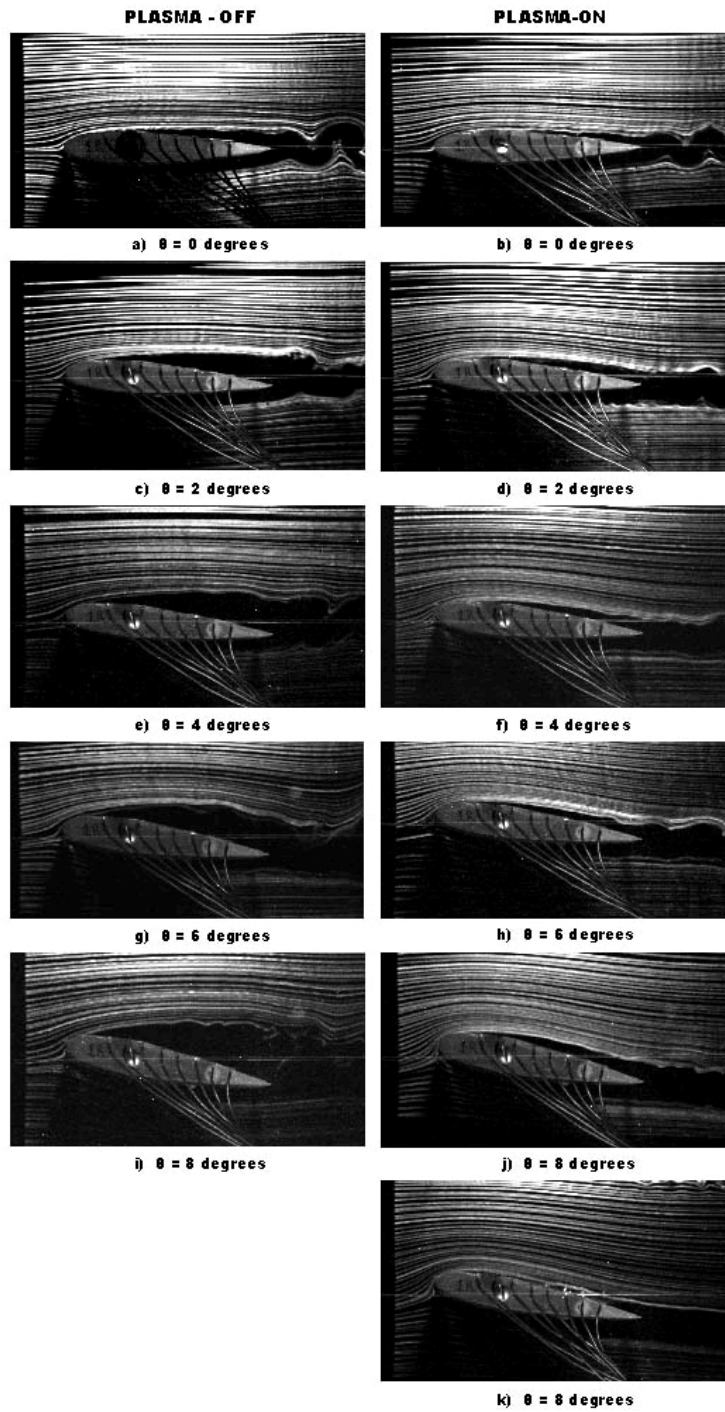
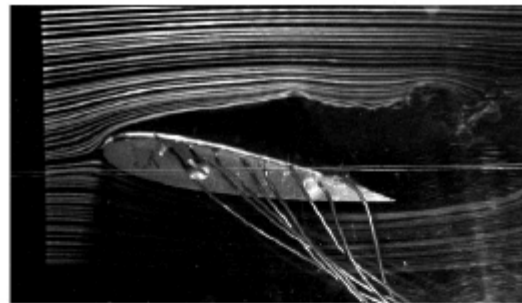
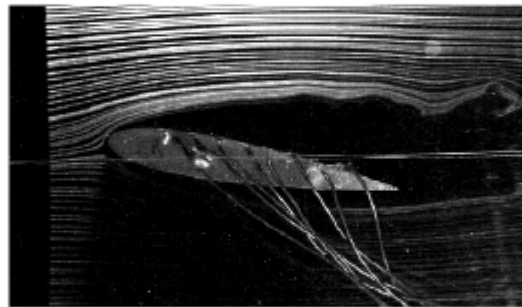


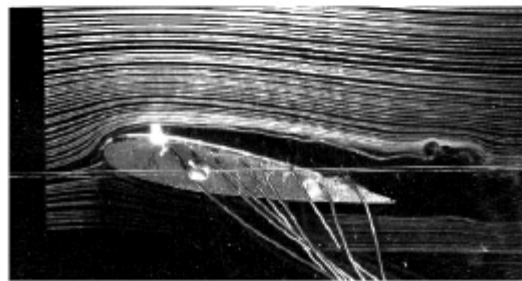
Figure 5.7: Effect of angle of attack with actuator #1 near the leading edge energized with 4.2KVrms, 4.2 kHz and a wind tunnel speed of 2.85 m/sec.



**a) With Trip wire - Plasma - off**



**b) Without Trip wire - Plasma - off**



**c) Without Trip wire - Plasma - on**

Figure 5.8: Effect of Trip Wire. Actuator #1 was energized with 4.2KVrms, 4.2 kHz and a wind tunnel speed of 2.85 m/sec.

**PLASMA OFF**



**PLASMA ON**

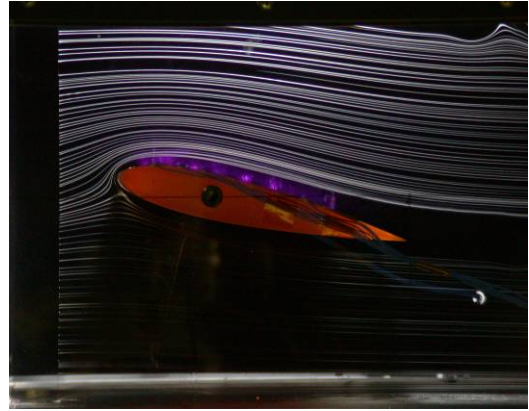


Figure 5.9: Flow re-attachment at high angle of attack, angle of attack -  $16^\circ$  at 3.6 kVrms, 4.2 kHz and a wind tunnel speed of 2.85 m/sec.

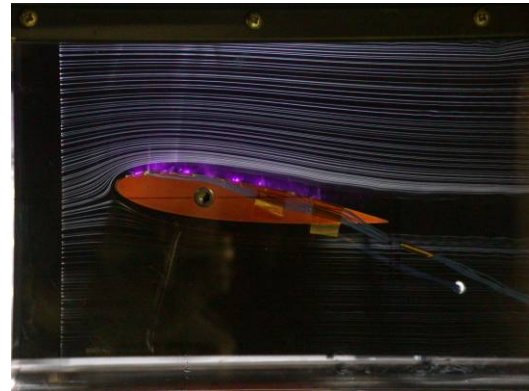
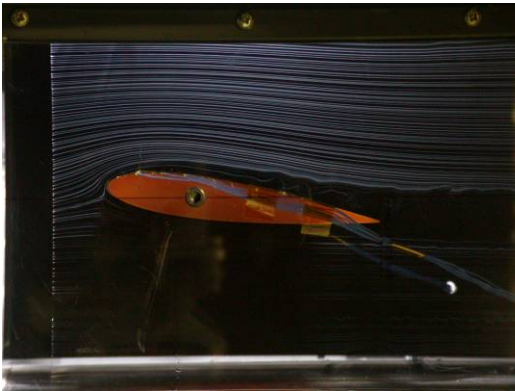


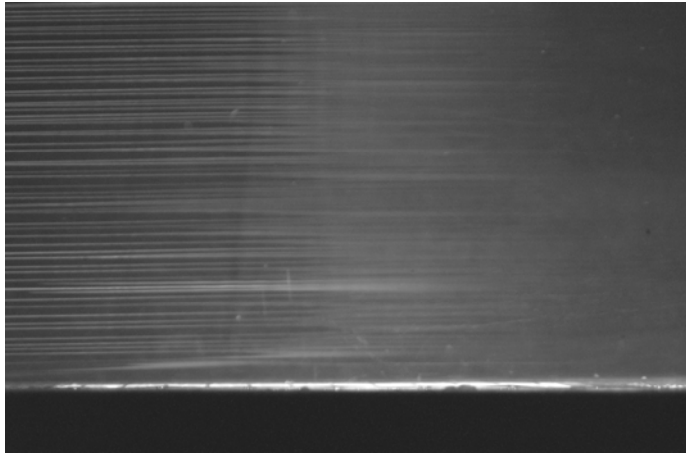
Figure 5.10: Flow re-attachment at high wind tunnel velocity, angle of attack -  $8^\circ$  and at 4.0 kVrms, 4.2 kHz, and a wind tunnel velocity of 7.6 m/sec.

plasma actuators energized at 4.0 kV rms and 4.2 kHz. The flow is almost attached in the plasma off condition, and it has a slight wave like instability downstream of the airfoil, indicating vortex formation and drag, which is eliminated when the actuators are on.

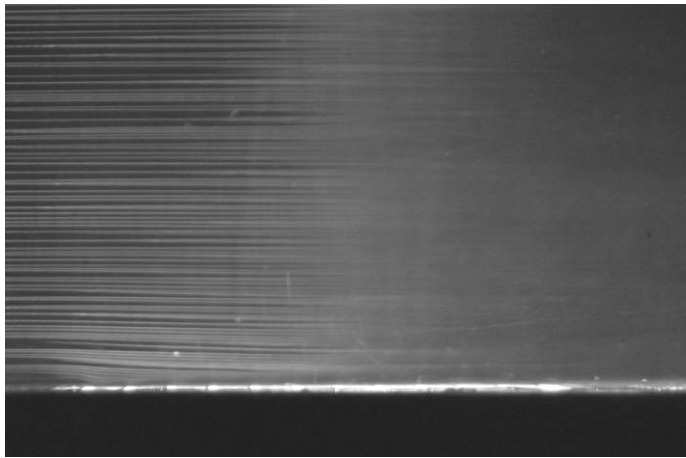
### **5.1.3 Smoke Flow Studies of Paraelectric Panel**

The paraelectrically-energized panel illustrated in Figure 3.8b was placed in the wind tunnel with the free stream velocity set at 1.6 meters/sec. With the panel un-energized, the flow field above the panel was laminar, as shown in Figure 5.11a, with a suggestion of boundary layer growth from a flow-tripping disturbance near the leading edge of the panel. When all 12 paraelectric plasma actuators were energized to add momentum to the 1.6 meter/sec wind tunnel flow at the boundary, the flow lines became more laminar, as shown in Figure 5.11b, and dipped down toward the panel. This descent of the flow lines is the result of the lower neutral gas pressure on the panel surface created by the presence of the plasma, and pumping of the neutral gas to the right by Lorentzian momentum transfer [3]. In Figure 5.11b, there is no evidence of counter-flowing boundary layer flow, turbulence generation, or a vertical component of the induced flow velocity that would produce an angled wall jet.

Figure 5.12a shows the condition when only electrode #1 is energized at 3.5 kV and 4.5 kHz. It clearly shows the smoke trails dipping down towards the panel at the position of the energized electrode. Figure 5.12b shows the position of the plasma actuators without smoke trails and all electrodes energized. This image is helpful during paired comparison between the plasma off and plasma on conditions of the plasma panel.

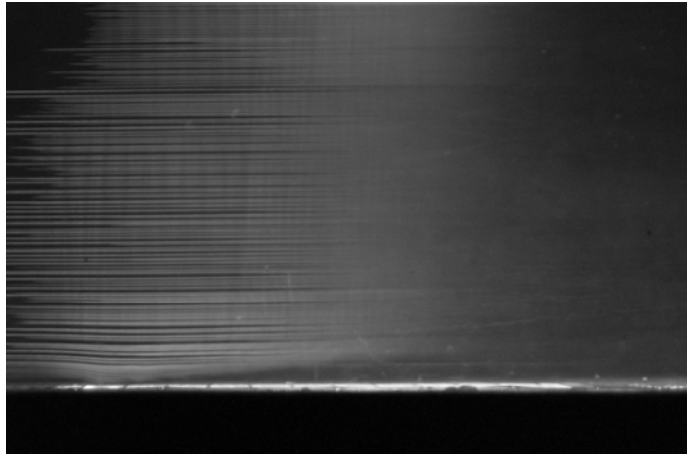


(a)



(b)

Figure 5.11: Smoke Flow Studies of Paraelectric Panel. (a) Smoke trails with wind tunnel velocity of 1.6 meters/sec and paraelectric plasma actuators not energized. (b) Smoke trails with wind tunnel velocity of 1.6 meters/sec and all 12 paraelectric plasma actuators energized with 3.5kV rms and 4.0 kHz.



(a)



(b)

Figure 5.12: Smoke Flow Studies of Paraelectric Panel. (a) Smoke trails with wind tunnel velocity of 1.6 meters/sec and only the first paraelectric plasma actuator energized with 3.5 kV rms and 4.0 kHz, (b) Position of the 12 plasma actuators when plasma actuators are energized with 3.5 kV rms and 4.0 kHz.

#### 5.1.4 Smoke Flow Studies of Peristaltic Panel

As explained before there are two different types of peristaltic panel; smoke flow tests were conducted on both the pure peristaltic panel and combined piezoelectric and peristaltic panels. The pure peristaltic panel shown in Figure 3.7a and 3.8a was installed in the 7x11 Inch Low Speed Wind Tunnel. The panel generates OAUGDP<sup>TM</sup> plasma on both sides of each electrode as illustrated in Figure 3.7a. It was found during previous research with plasma actuators [26,27] that the OAUGDP<sup>TM</sup> creates a low pressure region, and an induced boundary layer flow away from both sides of each electrode, resulting in the formation of turbulent vortex pairs between each pair of strip electrodes. The airflow over the ceramic pure peristaltic panel of Figure 3.9b with the plasma off and a wind tunnel free stream velocity of 3.95 meters/second is shown in Figure 5.13a. When all the electrodes were energized with 4 kV and 4 kHz, the behavior of smoke trails on the same panel is shown in Figures 5.13b and 5.13c. Figure 5.13b shows the polyphase power supply phased in such a way that the induced peristaltic gas flow is to the right (positive flow) and Figure 5.13c shows the smoke trails when the peristaltic gas flow is to the left (negative flow).

The smoke trails in Figures 5.13b and 5.13c show that the pure peristaltic flow is turbulent in the boundary layer. The turbulence arises from the phenomenon documented in previous studies of drag [28,29], whereby the plasma on both sides of the electrode creates a low pressure region there, and the descending flows of air are pumped by the plasma to the right and left. The flow to the right adds ( in the direction of the polyphase traveling wave) momentum to the boundary layer flow, but the flow to the left simply trips the flow into turbulence and results in the thickened boundary layer flow evident in

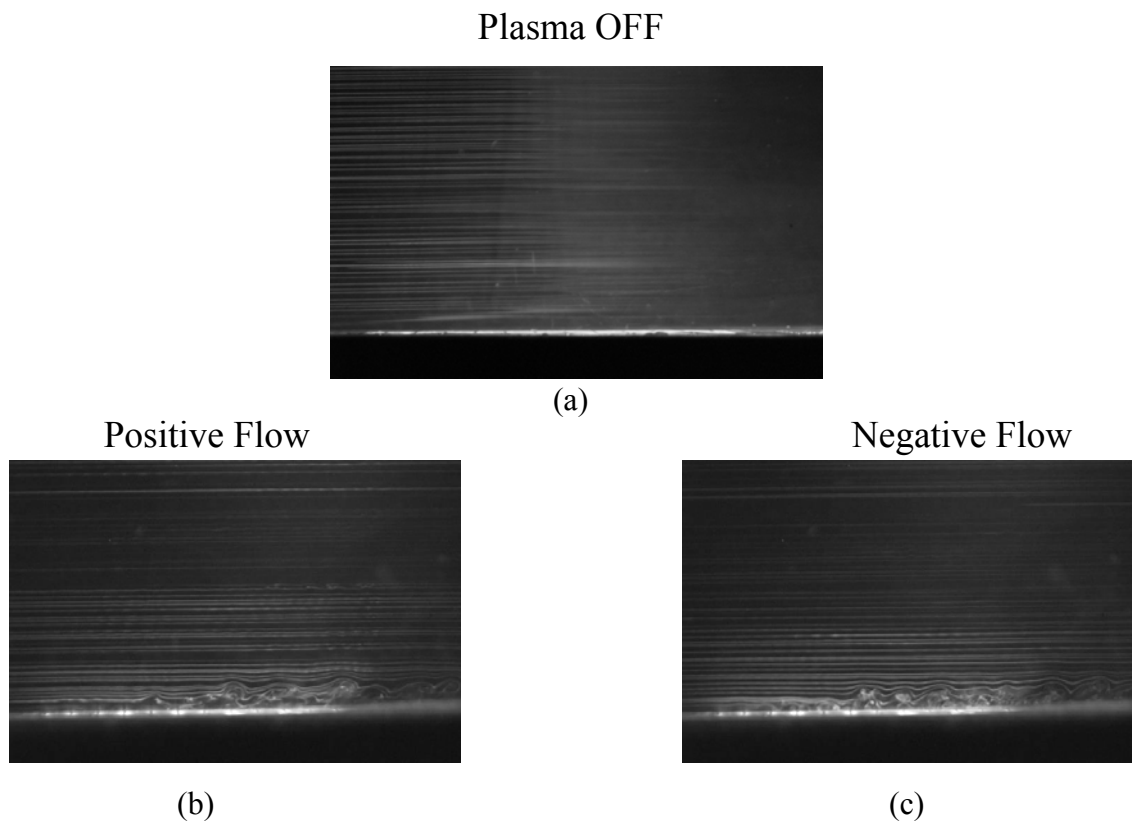
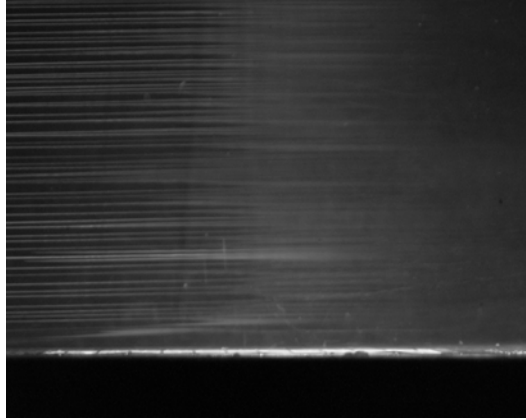


Figure 5.13: Smoke trails of the pure peristaltic panel of figures 3.7a and 3.8a, showing both plasma off and plasma on conditions. Electrodes were energized with 3 kV rms, 4 kHz and the wind tunnel velocity was 3.95 meters/sec.

Figures 5.13b and 5.13c. It is clear from Figures 5.13b and 5.13c that the “pure peristaltic” panel design of Figure 3.8a, despite its simplicity, is an inferior plasma actuator because of the flow tripping and induction of turbulence associated with the paraelectric flows counter to the peristaltic wave and free stream velocity. Over the parameter envelope covered in these investigations, we did not see any cases in which the peristaltic effects so dominated the paraelectric flow acceleration that the boundary layer of a pure peristaltic panel remained laminar, with parallel flow (or smoke) lines.

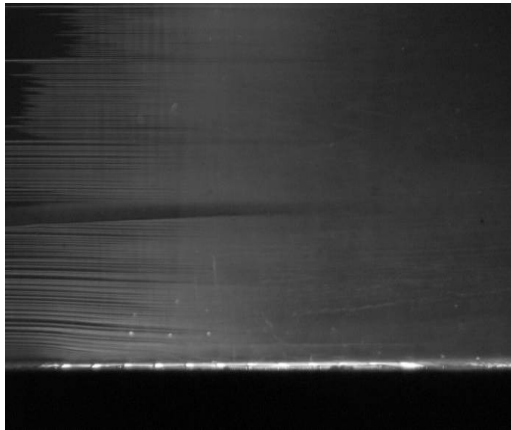
It is clearly desirable to add the paraelectrically induced flow from asymmetric electrodes to the peristaltically induced flows generated by a phased array of electrodes. This can be done with the combined electrode geometry documented in Figure 3.8b, which accelerates both the paraelectric and peristaltic flows in only one direction, as illustrated in Figure 3.7b. The combined paraelectric and peristaltic panel was mounted in the wind tunnel. The plasma off condition is shown in Figure 5.14a. When the panel was energized with 8 phase polyphase power so that both the peristaltically and paraelectrically induced velocities added and were in the direction of the wind tunnel flow, the behavior of the smoke trails is shown in Figure 5.14b. Here, the Lorentzian momentum is added to the flow, and the resulting low pressure above the panel surface causes the flow lines to dip down toward the panel without flow tripping or the generation of turbulence. When the phasing is made in such a way that the peristaltically induced velocities oppose the direction of the wind tunnel flow, the resulting flow field is shown in Figure 5.14c. The flow field is not turbulent as expected, and the paraelectric forces in the direction of the wind tunnel flow dominate the peristaltic forces opposing the flow.

Plasma OFF



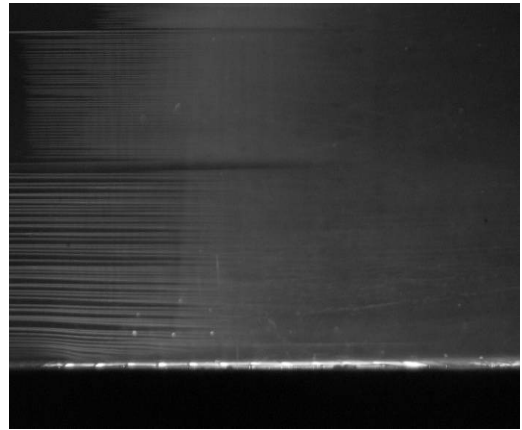
(a)

Positive Flow



(b)

Negative Flow



(c)

Figure 5.14: Smoke trails of the combined peristaltic and paraelectric panel, showing both plasma off and plasma on conditions. Electrodes were energized with 3.5 kV rms, 4 kHz and the wind tunnel velocity was 3.95 meters/sec.

However, the smoke flow is less attached to the surface of the panel when compared to Figure 5.14b. It is clear that the electrode design of Figure 3.8b is to be preferred for peristaltic flow acceleration. Another observation is that under no set of operating conditions, for any of the panel designs, did flow lines rise at an angle from the panel surface, as though vertically upward momentum had been introduced. The horizontal, laminar nature of the flow (except for the flow tripping of Figure 5.13b and 5.13c) may be the result of upper electrodes much thinner than the height of the maximum of the wall jet velocity (0.06mm versus about 1mm, respectively).

## **5.2 Boundary Layer Velocity Profile of Plasma Actuators**

To better understand the vertical velocity profile of the plasma actuators, Pitot tube measurements of the horizontal velocity component of the boundary layer flow were made using the instrumentation shown in Figure 5.15. The system used to measure and store velocity profile data is explained in Section 4.4. The ceramic panel shown in Figure 5.15 is recessed in a rectangular groove machined in the bottom plate of the wind tunnel, to avoid flow tripping. The Pitot probe was mounted on the axis of panel, with its opening 1.5 cm from the downstream edge of the last electrode on the upper surface of the panel. The vertical extent of the measured velocity profiles ranged from the surface to as much as 3 centimeters above the surface. In these measurements, no vertical sidewalls were erected at the edges of the panel to avoid out-flowing of the gas at the edges of the panel. The opening of the Pitot tube tip is shown in Figure 5.16. The tip was constructed from 25 gage stainless steel hypodermic tubing (OD=0.5 mm, ID= 0.36 mm).

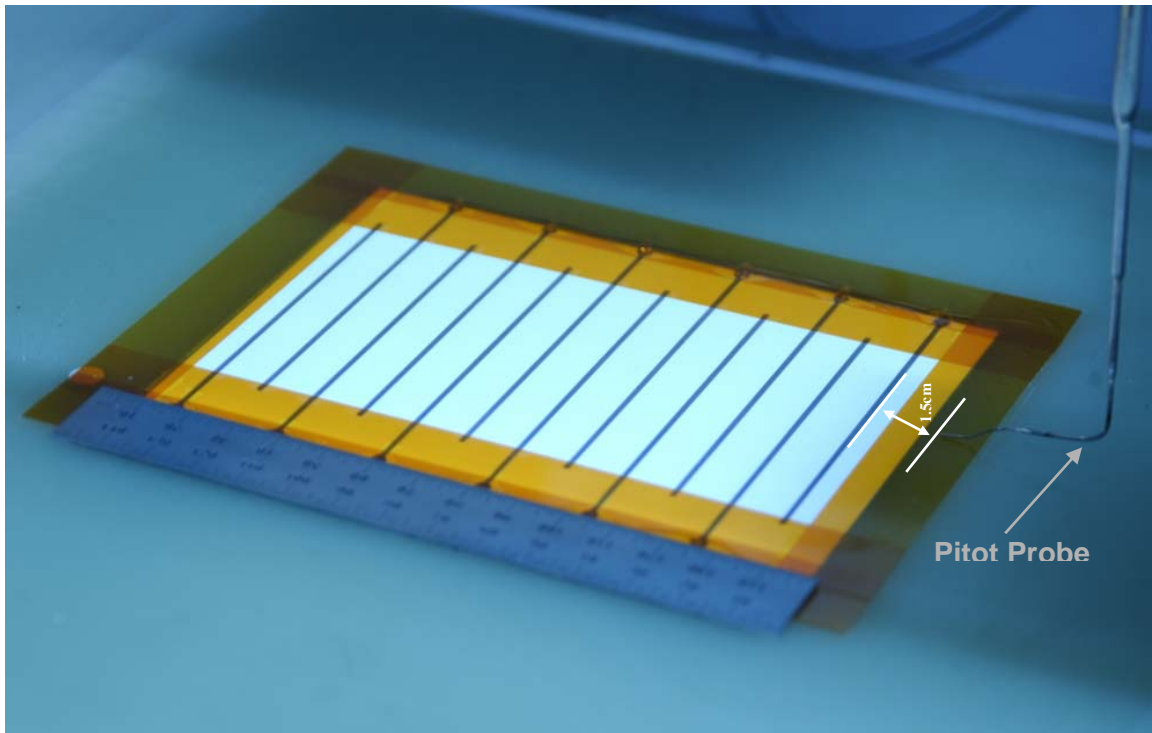


Figure 5.15: Combined peristaltic and piezoelectric ceramic panel mounted in the wind tunnel. Arrows indicate the Pitot tube and position of the Pitot tube opening 1.5 cm downstream of the last actuator.

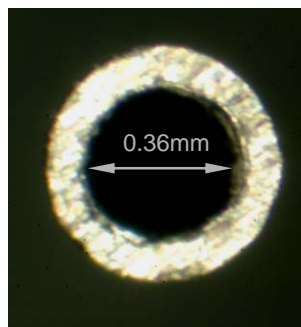


Figure 5.16: Opening of Pitot tube used in the present investigation, inside diameter 0.36 mm.

Since the Pitot probe is metallic, care was taken to keep the probe at a safe distance from the electrodes. Bringing the probe closer may cause a discharge between the probe and surface electrodes, and damage to the Pitot system electronics.

#### *Paraelectric panel velocity profile*

The combined peristaltic and paraelectric panel was run in the pure paraelectric mode (i.e. all the plasma actuators on the panel were operated at the same electrical phase). Vertical profiles of the boundary layer velocity were taken up to a height of 12mm, which was in the free stream of the wind tunnel. These profile measurements were accompanied by an aphysical 0.5 m/sec positive zero offset associated with the Pitot tube measuring system. Figure 5.17 shows the boundary layer velocity profile with the plasma actuators un-energized and the wind tunnel velocity set at 3.95 meters/sec.

Figure 5.18 shows the boundary layer velocity profile of the combined paraelectric and peristaltic panel run in the pure paraelectric mode with 3.5 kV, 4 kHz, and the wind tunnel off. The velocity near the surface of the panel reaches 1.6 m/sec.

#### *Peristaltic panel boundary layer profile*

A set of characteristic boundary layer profiles from a combined paraelectric and peristaltic ceramic panel operating with a wind tunnel velocity of 1.6 m/sec is shown in Figure 5.19. The left-hand profile shows the classic boundary layer profile with the plasma actuators un-energized. The Pitot-system noise/zero offset is evident below 0.5 m/sec. The right-hand profile shows the boundary layer profile with all 12 actuators on the panel energized

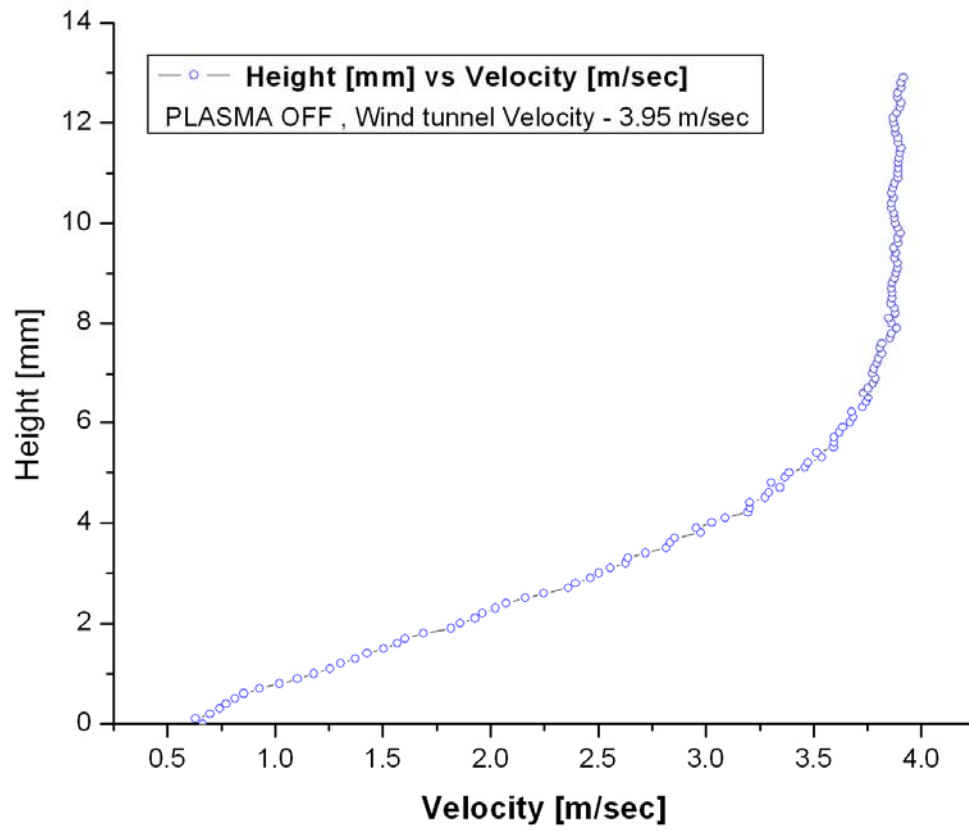


Figure 5.17: Velocity profile with plasma off and a wind tunnel velocity of 3.95 meters/sec.

## VELOCITY PROFILE

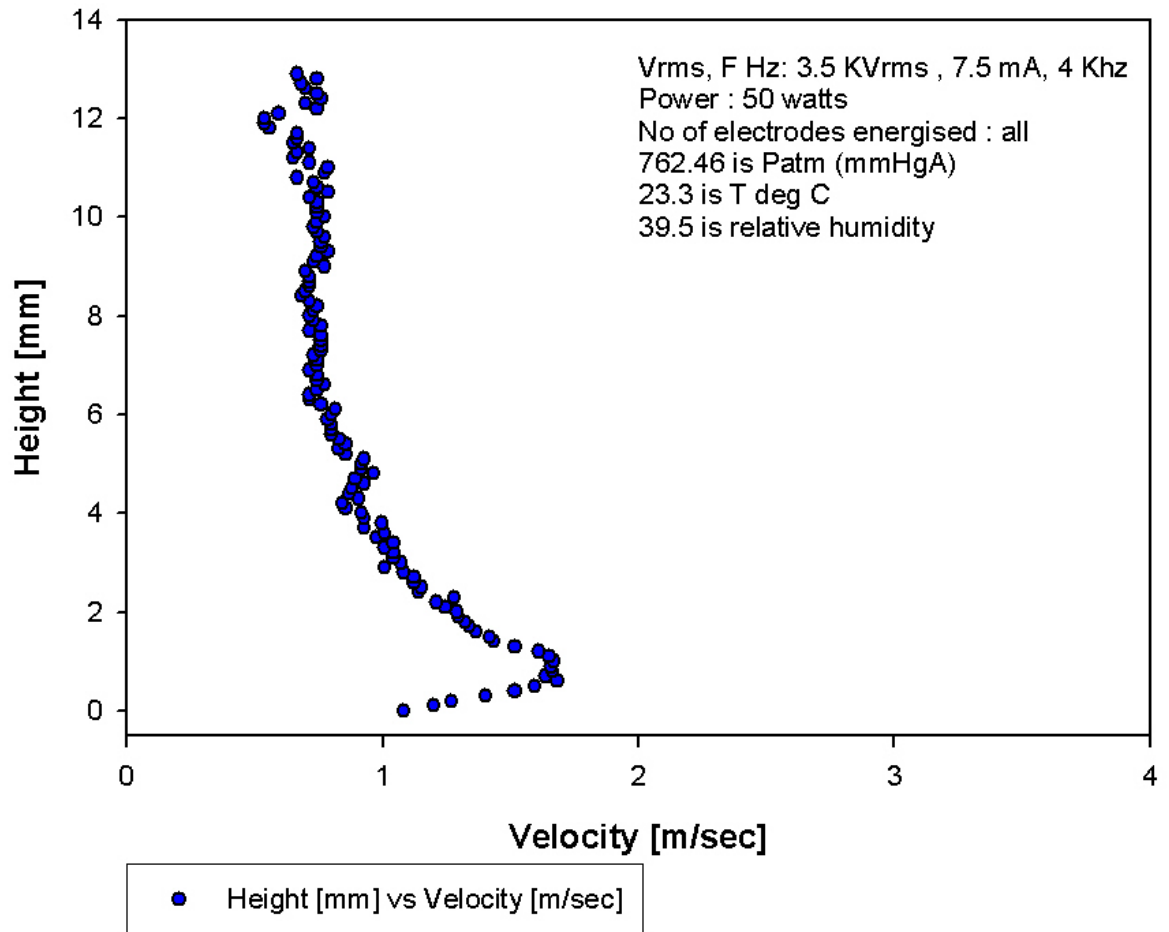


Figure 5.18: Velocity profile when all electrodes are energized with wind tunnel off. The Pitot probe system contributed an aphysical 0.5 m/sec zero offset.

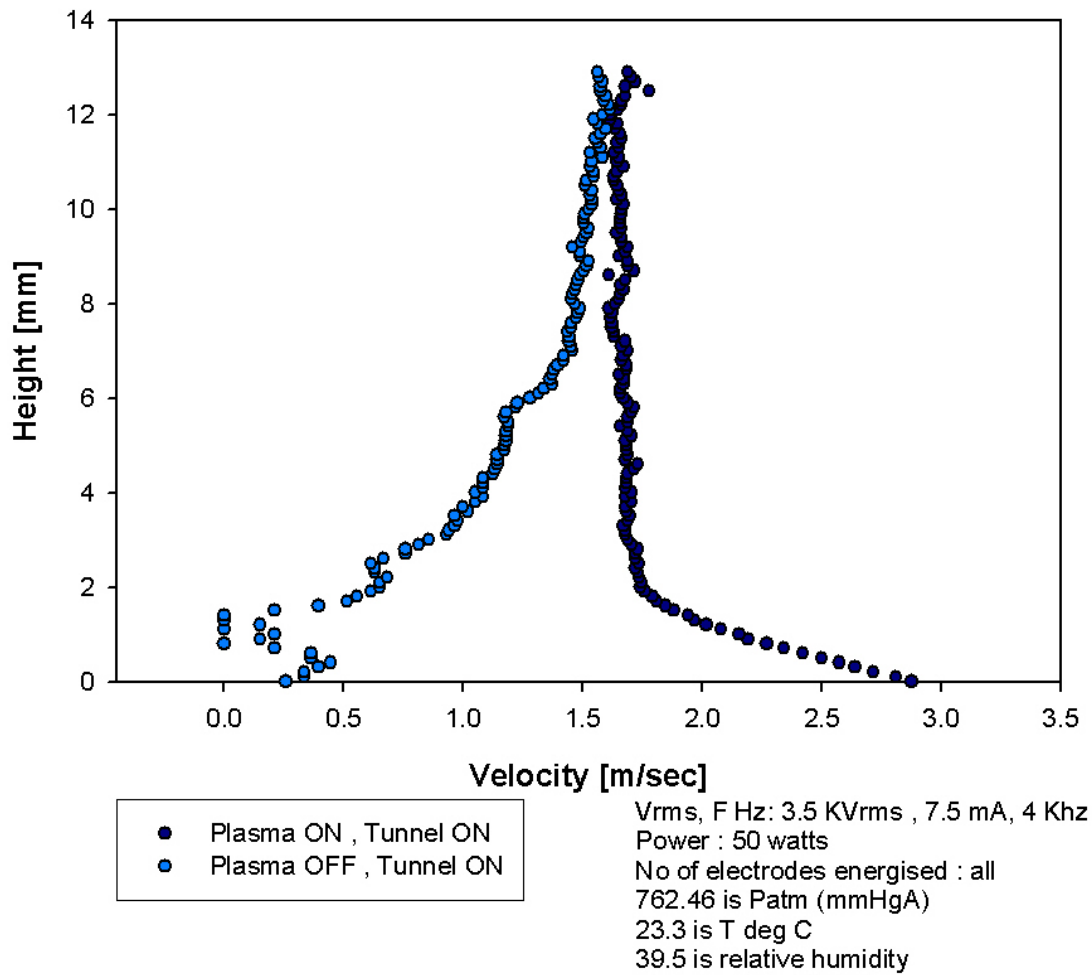


Figure 5.19: Pitot tube boundary layer velocity profiles taken with a wind tunnel velocity of 1.6 meters/sec, all 12 plasma actuators on the panel energized at 3.5 kV rms, 4.0 kHz, and 50 watts total power.

in such a way as to add momentum to the boundary layer flow. This momentum addition has been sufficiently effective in this case that the peak of the velocity profile is closer to the panel surface than the resolution of the Pitot tube positioning system, approximately 100 microns.

Figure 5.20 compares three different modes of operation; when the plasma actuators are turned off, when the peristaltic and paraelectric flow is in the same (positive) direction, and when the peristaltic and paraelectric flows oppose each other.

Figures 5.21a and 5.21b show visualization of peristaltic flow acceleration using titanium dioxide smoke. All electrodes are energized at 3.5 kV rms and 3 kHz with three complete phase cycles on the panel. Figure 5.21a shows the flow direction when phase angles were increased by 45° from left to right and Figure 5.21b shows the condition when the phasing was reversed.

### **5.2.1 Effect of Number of Plasma Actuators Energized**

These measurements were taken to determine whether the addition of momentum to the boundary layer flow was linear with the number of plasma actuators in series, or whether saturation occurred, due to sideways flow from the panel, boundary layer thickening, or other effects. This issue was addressed with the Pitot tube in the configuration of Figure 5.15 with the wind tunnel off, and the plasma actuators were energized successively starting from the pair closest to the Pitot tube, then the two closest pairs, and so forth until all 12 actuators were energized.

The results of these measurements are plotted in the three-dimensional graph of Figure 5.22, the axes of which are the flow velocity, the number of actuators energized, and the height above the panel surface. These data were taken at an RF voltage

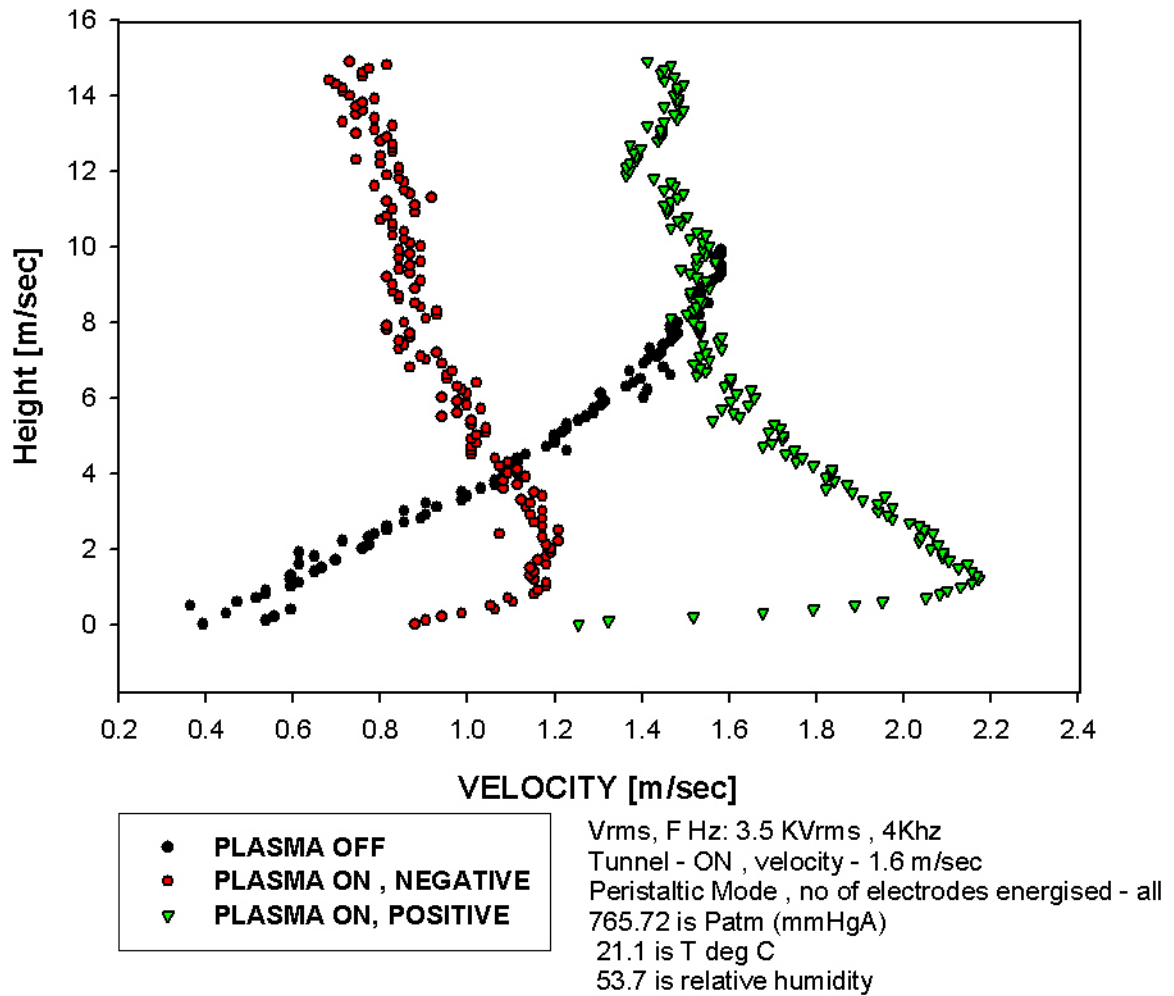
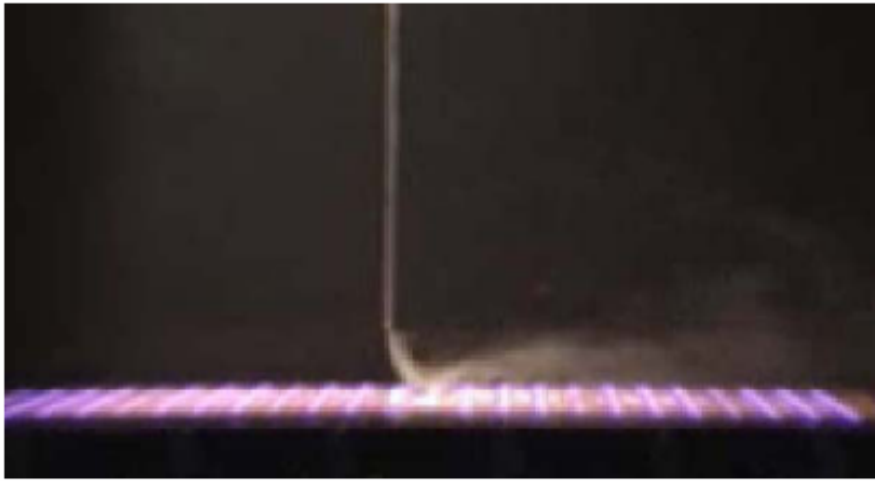
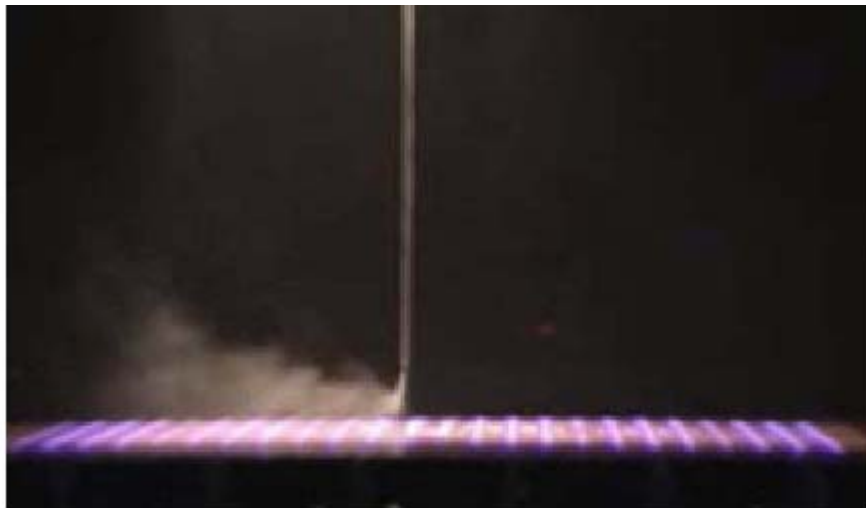


Figure 5.20: Pitot tube boundary layer velocity profiles for positive and negative peristaltic flow, taken with a wind tunnel velocity of 1.6 meters/sec, and all 12 plasma actuators on panel energized at 3.5 kV rms, 4.0 kHz



(a)



(b)

Figure 5.21: Visualization of peristaltic flow using titanium dioxide smoke. All electrodes are energized at 3.5 kV rms and 3 kHz with three complete phase cycles on the panel. (a) Phase angles were increased by  $45^\circ$  from left to right, (b) Same condition as (a) except the phasing was reversed.

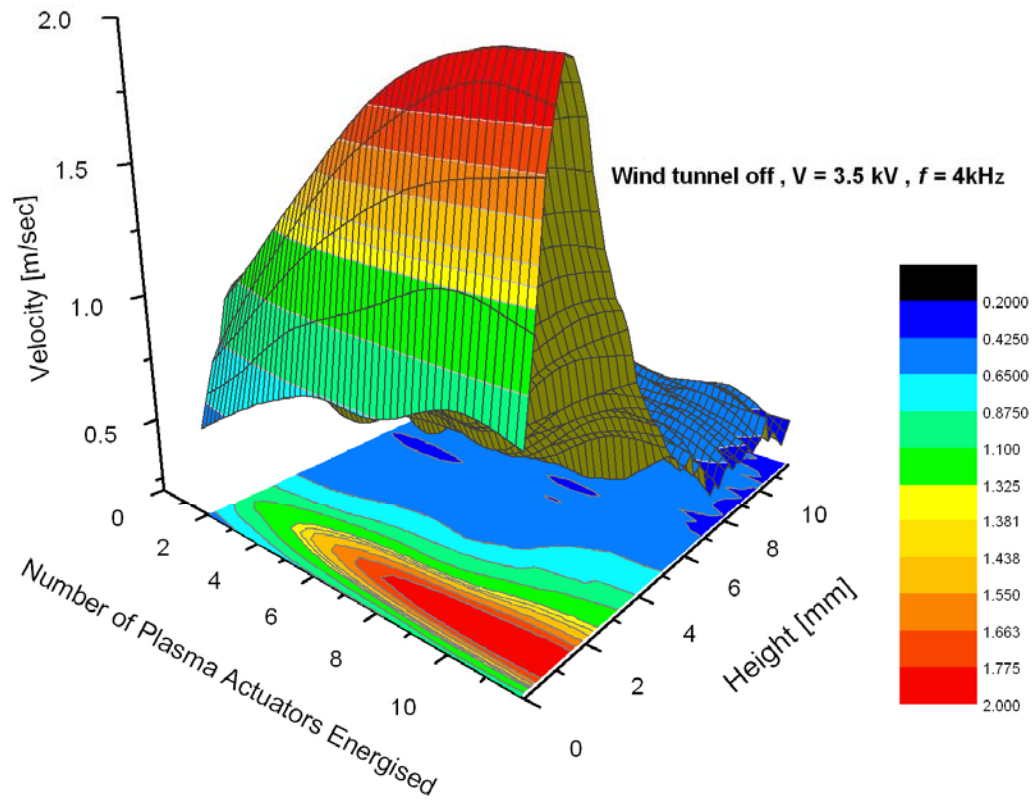


Figure 5.22: Pitot tube vertical boundary layer profiles 15 mm from the edge of plasma actuator # 1 with the wind tunnel off, 3.5 kV rms, 4.0 kHz, and for 2, 4, 6, 8, 10, and 12 plasma actuators energized.

on the actuators of 3.5 kV and a RF frequency of 4.0 kHz. They show that the peak velocity is not linear with the number of actuators, but saturates after about 10 actuators in series. The maximum of the velocity profile is at a height of about 1 mm at the Pitot tube position regardless of the number of electrodes energized.

Figure 5.23 shows the velocity (at the wall jet maximum) as a function of the number of electrodes energized. It is evident that the velocity becomes asymptotic after a certain number of actuators were energized. However, for some high voltage experimental runs the velocity increased monotonically as the number of actuators increased. The ceramic panel is limited to 12 electrodes and this limits our ability to understand the effect of the number of electrodes energized. If a larger panel with more electrodes were used, eventually the flow velocity may become asymptotic due to viscosity, turbulence, etc.

### **5.2.2 Parametric Variations of Maximum Flow Velocity**

The effect on the maximum plasma actuator jet velocity of varying the RF frequency energizing the electrodes is plotted in Figure 5.24. For these data, the wind tunnel was off (the velocity was due entirely to the plasma actuators), the voltage was kept constant at 4 kV rms, and all 12 actuators on the panel were energized. The voltage could not be increased above 4 kV rms for these conditions because of sparking and tracking and panel breakdown at higher frequencies. The velocity increased linearly with RF frequency. There are at least two reasons for this: as the frequency increases, the ion trapping improves, increasing the plasma density; and the number of impulses per second of Lorentzian momentum addition increases with frequency.

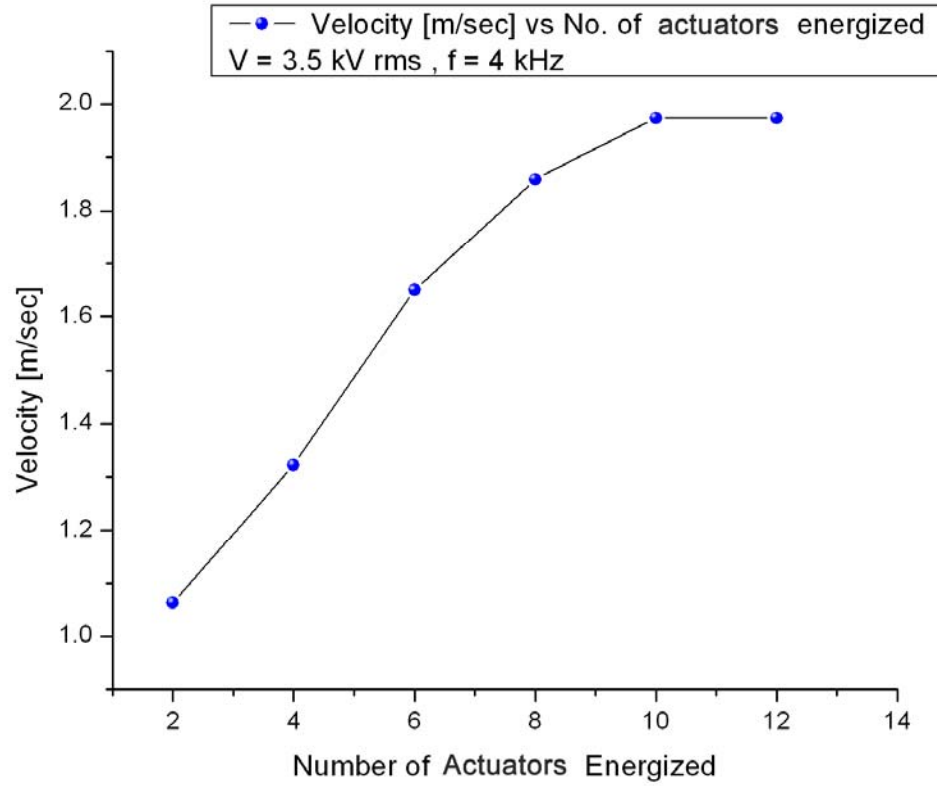


Figure 5.23: The induced wall-jet velocity 1.5 cm from the last plasma actuator as a function of the number of plasma actuators energized, and at the height of the boundary layer velocity maximum.

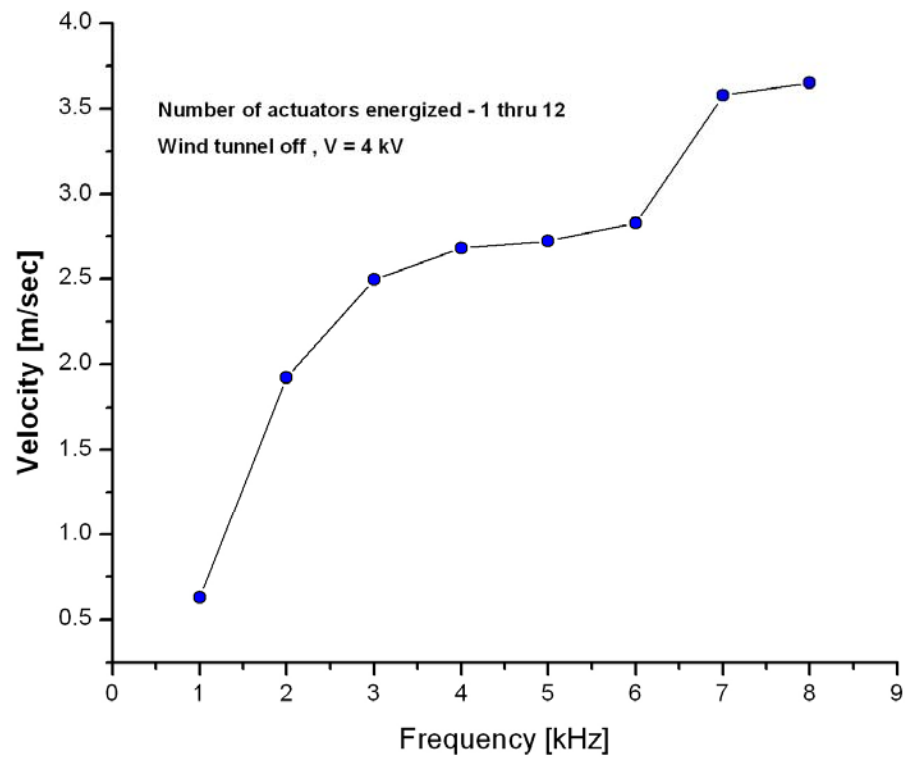


Figure 5.24 The maximum jet velocity in the boundary layer as a function of the RF frequency with the wind tunnel off, all 12 electrodes on the panel energized, and the RF voltage 4.5 kV rms.

The dependence of the maximum wall jet velocity on RF voltage for paraelectric and peristaltic excitation of a ceramic panel at an RF frequency of 6.0 KHz is shown in Figure 5.25 with all 12 plasma actuators energized. These measurements were taken using the combined paraelectric and peristaltic panel shown in Figure 3.8b. Figure 5.25 clearly shows the difference between the peristaltic and paraelectric flow acceleration. The paraelectric flow results were obtained by operating all 12 actuators in phase; and the combined paraelectric and peristaltic results were obtained with 8 phase polyphase excitation of the actuators. These data indicate that the paraelectric acceleration mechanism was weaker than the peristaltic acceleration for these conditions.

Figure 5.26 shows the dependence of maximum wall jet velocity on both RF voltage and frequency. These measurements were taken with the pure peristaltic panel shown in Figure 4.10; this panel is larger and has more actuators than the ceramic panel. The graph shows the increase in maximum wall jet velocity as both RF voltage and frequency is increased.

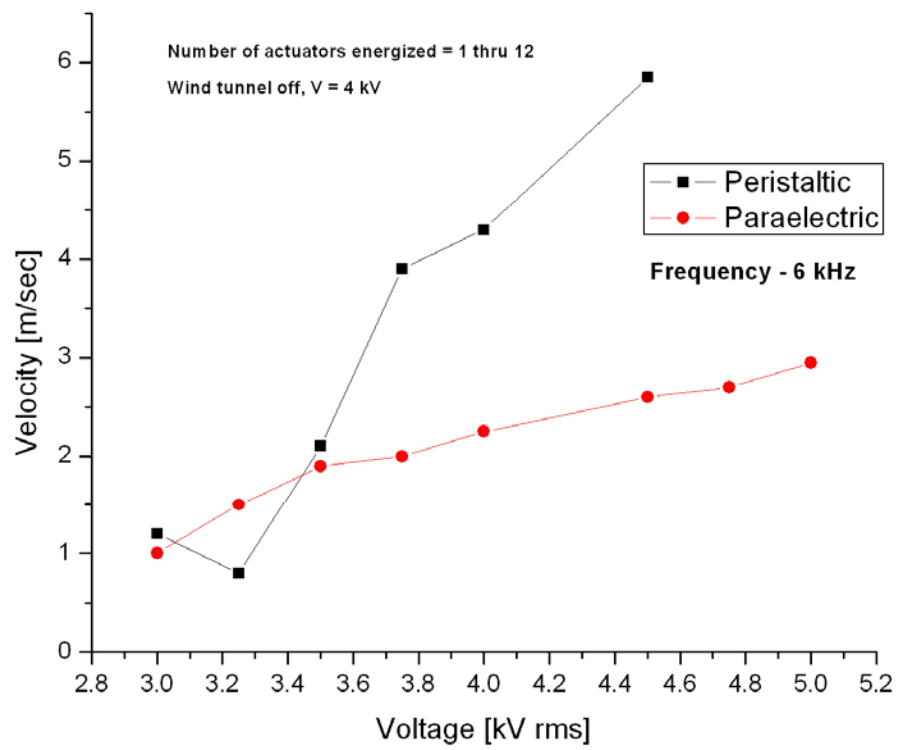


Figure 5.25: Peristaltically and paraelectrically induced velocities as functions of RF driving voltage on 12 plasma actuators at a RF frequency of 6 kHz.

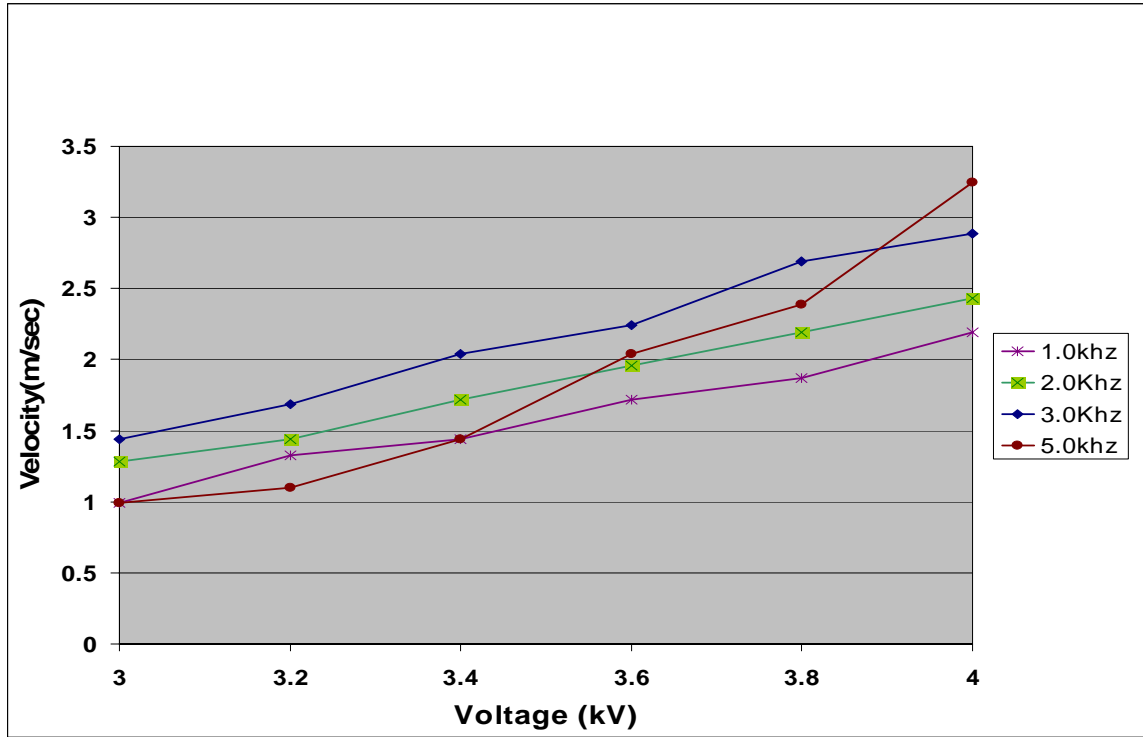


Figure 5.26: Peristaltically induced velocity as a function of RF driving voltage and frequency on plasma actuators.

## 6. FUTURE WORK

Several lines of research and development of plasma actuators can be undertaken to extend the present work.

### *Low cost power supply*

The Powertron<sup>TM</sup> power amplifier and high voltage transformer system used for our current aerodynamic research is comparatively heavy and costly. Further studies are needed to develop a new power supply that is light and inexpensive. One approach to such a power supply is shown in Figure 6.1. Important components of this circuit are an automotive ignition coil, a Mosfet (MOS field-effect transistor), and a 555 timer. The frequency of this power supply is varied by changing the values of the resistors and capacitors. The following equation is derived from the circuit of Figure 6.1:

$$f = \frac{1.44}{(R_1 + 2R_p) \times C_1}$$

The RF power supply actually used can be replaced using audio power amplifiers (which cost around \$40 to \$100) driving automotive ignition coils. If this circuit is used for 8-phase peristaltic flow acceleration experiments, eight ignition coils are needed. Another approach is to use flyback transformers (i.e. those used in television sets) that can produce two different outputs with a 180 degree phase difference. Only four such transformers are needed for 8-phase peristaltic acceleration experiments. Figure 6.2 shows a schematic of the ignition coil and flyback transformer circuits. The average cost of the ignition coils or flyback transformers is about \$20.



### *Impedance matching*

Most of the experimental runs presented in this paper were not impedance matched. According to our previous studies [26,27,28], the plasma produced by a power supply impedance matched to the plasma load performs better. It is therefore advisable to impedance match the RF power supply to the plasma actuator(s) of the paraelectric gas flow accelerator. Another desirable task is to impedance match all the phases of the polyphase peristaltic flow accelerator, where each phase should be impedance matched separately to obtain the best results.

### *Particle Imaging Velocimetry*

Particle image velocimetry is a pulsed planar laser light sheet technique in which the images of fine particles lying in the plane of the light sheet are recorded on a video camera or photograph. The displacement of the particle images is measured in the plane of the image, and used to determine the displacement ( and hence the velocity) of the particles in the flow. Such a technique was used at the NASA Langley Research Center to obtain the flow field over the peristaltic Kapton<sup>TM</sup> panel shown in Figure 3.9a. Figure 6.3 shows the apparatus used for this technique. Several planes parallel and perpendicular to the panel were used to capture the flow field. However, we found that the flow field could not be captured because the direction of flow above the peristaltic panel is not in a single plane. This indicates that a technique called “3D particle imaging velocimetry” should be used in order to capture the three dimensional peristaltic flow.



Figure 6.3: Kapton™ peristaltic panel installed on a particle imaging velocimetry test section.

#### *Embedded electrode panels*

The panels that were used for the above experiments do not have embedded electrodes, electrodes covered by the aluminum oxide panel material. It would be desirable to use an embedded electrode panel for aerodynamic flow acceleration applications. Such a panel would have all its electrodes embedded within the ceramic panel in the configuration shown in Figure 6.4. Such a configuration makes the panel more robust with respect to sparking and electrical breakdown, resulting in an improved life-time and greater safety when operated on an aircraft.

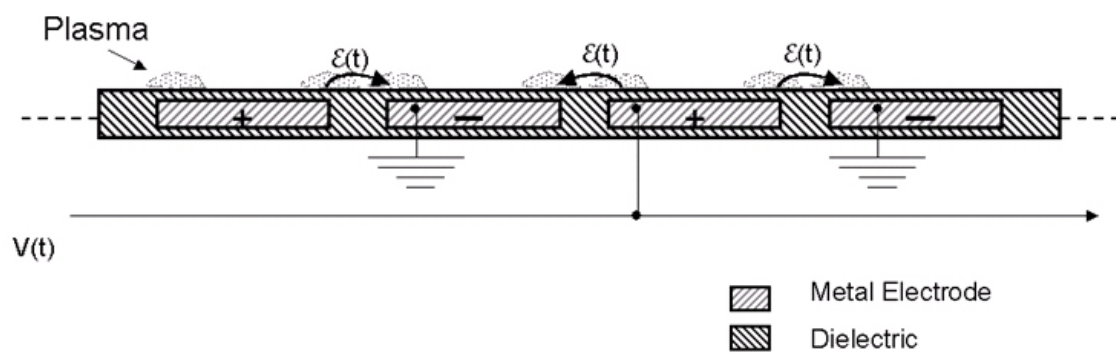


Figure 6.4: Coplanar OAUGDP™ with electrodes embedded in dielectric material.

## 7. CONCLUSION

The ability of both paraelectric and peristaltic OAUGDP<sup>TM</sup> actuators to accelerate neutral gas flows to several meters per second in atmospheric pressure air was demonstrated. The plasma actuators also were able to add or remove momentum from a boundary layer without adding or removing mass. This paper presents many successful examples of mechanically and electrically robust paraelectric, pure peristaltic, and combined paraelectric and peristaltic plasma actuators.

Paraelectric momentum addition has a significant effect on re-attaching flows to a NACA 0015 airfoil at free stream velocities up to 7.6 meters/sec and at angles of attack up to 12°. Peristaltically induced flows up to 6 meters/sec were demonstrated. In addition, it is evident from Figures 5.19a and 5.19b that reversing the phase angle of the peristaltic electrostatic wave reversed the flow. Smoke flow visualization tests indicate that the pure peristaltic panel is of limited interest because of the counter-flowing jets originating on the upstream side of the phased electrode strips. The most promising design was the combined paraelectric and peristaltic panel of Figure 3.8b, in which the peristaltic flow from phased electrodes was given an additional boost by paraelectric momentum addition, with no momentum addition counter to the dominant flow to induce turbulence in the boundary layer.

Smoke flow studies were performed to document the presence or absence of boundary layer turbulence for the types of panel under development, and for various operating conditions. The behavior of smoke trails for the paraelectric and combined paraelectric and peristaltic panels was laminar over the entire range of operating conditions studied, with the flow lines parallel to, or slowly descending towards the

plasma actuators (or panel). Further observations from smoke flow studies show that there is no jet leaving either the paraelectric or the peristaltic plasma actuator at an angle to the flow direction when there is a wind tunnel flow, as illustrated in Figures 5.11b, 5.13b and 5.13c. This may be related to the circumstance that the electrodes in the ceramic panel are flush (within 0.06mm) with the surface, and project into the flow much less than the height of the maximum velocity of the boundary layer wall jet.

Vertical boundary layer velocity profiles were taken under a wide range of plasma actuator operating conditions. The velocity profile characteristically shows a flow velocity decrease with height, and a maximum flow velocity at a height at or slightly less than 1mm. In Figure 5.16, the maximum velocity occurred within the smallest vertical resolution of our Pitot system, approximately 50 microns. The velocity increase of a staged series of plasma actuators initially rises linearly, but saturates above 10 such actuators, presumably because the flow “escapes” from the spanwise edges of the active area of the actuator panel. We found also that the maximum wall jet velocity increases linearly with the RF driving frequency and voltage, below the optimum of these parameters for the ion trapping frequency.

If paraelectric or peristaltic methods of flow acceleration could produce higher velocities, comparable to the landing or take-off speed of aircraft, it might be possible to replace the mechanical, electro-mechanical and hydraulic components of existing aircraft with robust, light and less problematic OAUGDP<sup>TM</sup> plasma actuators.

## REFERENCES

## REFERENCES

- [1] Von Engle, A., Seeliger, R, and Steenback, M.: “On the glow discharge at high pressure” *Zeit. fur Physik*, Vol. 85, 144 (1933) pp 144-160.
- [2] Roth, J. R.: *Industrial Plasma Engineering. Volume I -- Principles*. Institute of Physics Publishing, Bristol and Philadelphia, ISBN 0-7503-0318-2,(1995) See Section 12.5.2
- [3] Roth, J. R.: *Industrial Plasma Engineering. Volume II -- Applications to Non-Thermal Plasma Processing*. Institute of Physics Publishing, Bristol and Philadelphia, ISBN 0-7503-0545-2, (2001) See Section 18.6.
- [4] Ben Gadri R., “One Atmosphere Glow Discharge Structure Revealed by Computer Modeling,” *IEEE Trans. Plasma Sci.*, Vol. 27, No. 1, 1999.
- [5] Ben Gadri, R., "Numerical Simulation of an Atmospheric Pressure and Dielectric Barrier Controlled Glow Discharge". Ph.D. thesis, Order No 2644, University Paul Sabatier, Toulouse III, France, (1997).
- [6] Massines, F.; Ben Gadri, R.; Rabehi, A.; Decomps, Ph.; Segur, P.; and Mayoux, Ch.: "Experimental and Theoretical Study of a Glow Discharge at Atmospheric Pressure Controlled by Dielectric Barrier", *Journal of Applied Physics*, vol. 83, No. 6, pp 2950-2957, 1998.
- [7] Roth, J. R., Tsai, P. P.-Y. C, Liu, M. Laroussi, and Spence, P. D., "One Atmosphere Uniform Glow Discharge Plasma" U. S. Patent # 5,414,324, Issued May 9, 1995.
- [8] Malik, M. R., Weinstein, L.M., and Hussani, M. Y., “Ion Wind Drag Reduction”, *AIAA Paper 83-0231*, 1983.

- [9] El-Khabiry, S. and Colver, G. M.: “Drag Reduction by DC Corona Discharge Along an Electrically Conductive Flat Plate for Small Reynolds Number Flow”. *Phys. Fluids*, Vol. 9, No. 3 (1997) PP 587-599.
- [10] Enloe, C. L., McLaughlin, T. E., VanDyken R. D., Kachner, K. D., Jumper, E. J. and Corke, T. C.: “Mechanisms and Responses of a Single Dielectric Barrier Plasma” AIAA Paper 2003-1021, Proc. of the 41st AIAA Aerospace Sciences Meeting & Exhibit Reno, NV, January 6-9, 2003
- [11] Shyy, W., Jayaraman B. and Andersson, A.: “Modeling of Glow Discharge-Induced Fluid Dynamics”. *J. of Applied Physics*, Vol. 92, No. 11 (2002) pp 6434-6443.
- [12] Soldati, A. and Banerjee, S.: “Turbulence Modification by Large-Scale Organized Electrohydrodynamic Flows”. *Phys. Fluids*, Vol. 10, No. 7 (1998) PP 1742-1756.
- [13] Fulgosi, M.; Soldati, A. and Banerjee, S.: “Turbulence Modulation by an Array of Large-Scale Streamwise Structures of EHD Origin”. Proc. of FEDSM '99 3rd ASME/JSME Joint Fluids Engineering Conference, July 18-23 1999 San Francisco, CA pp 1-8.
- [14] Rivir, R., White Lt. A., Carter C., Ganguly B., Forelines A, and Crafton J.: “Turbine Flow Control, Plasma Flows” AIAA Paper 2003-6055, Proc. of the 41st AIAA Aerospace Sciences Meeting & Exhibit Reno, NV, January 6-9, 2003.
- [15] List, L., Byerley A. R., McLaughlin, T. E., and Van Dyken, R. D. “Using a Plasma Actuator to Control Laminar Separation on a Linear Cascade Turbine Blade” AIAA Paper 2003-1026, Proc. of the 41st AIAA Aerospace Sciences Meeting & Exhibit Reno, NV, January 6-9, 2003

- [16] Huang, J., Corke T. C. and Thomas, F. O.: “Plasma Actuators for Separation Control of Low Pressure Turbine Blades” AIAA Paper 2003-1027, Proc. of the 41st AIAA Aerospace Sciences Meeting & Exhibit Reno, NV, January 6-9, 2003.
- [17] Hultgren, L. S. and Ashpis, D. E. “Demonstration of Separation Delay with Glow-Discharge Plasma Actuators” AIAA Paper 2003-1025, Proc. of the 41st AIAA Aerospace Sciences Meeting & Exhibit Reno, NV, January 6-9, 2003.
- [18] Corke, T. C., Jumper, E. J., Post, M. L., Orlov, D. and McLaughlin, T. E.: “Application of Weakly-Ionized Plasmas as Wing Flow-Control Devices” AIAA Paper 2002-0350, Proc. of the 41st AIAA Aerospace Sciences Meeting & Exhibit Reno, NV, January 6-9, 2003.
- [19] Post, M. L. and Corke, T. C.: “Separation Control on High Angle of Attack Airfoil Using Plasma Actuators” AIAA Paper 2003-1024, Proc. of the 41st AIAA Aerospace Sciences Meeting & Exhibit Reno, NV, January 6-9, 2003.
- [20] Hefner, J., and Bushnell, N.,: “Viscous Drag Reduction in Boundary Layers” AIAA Progress in Aeronautics and Astronautics, vol. 123, Seabass A.R., ed., ISBN 0-930403-66-55, pp. 457-476., 1989.
- [21] Walsh MJ. “Riblets, in Progress in Aeronautics and Astronautics”, Vol. 123, 1990.
- [22] Kimura, M., Tung, S., Ho, C., Jiang, F., Tai, Y.,: “MEMS for Aerodynamic Control”, AIAA Paper 97-2118, 28<sup>th</sup> AIAA Fluid Dynamics Conference, June 29 – July 2, 1997, Snowmass Village, CO.

- [23] Roth, J. R.: "Method and Apparatus for Covering Bodies with A Uniform Glow discharge Plasma and Applications Thereof" U. S. Patent # 5,669,583, Issued Sept 23, 1997.
- [24] Sherman, D. M., Wilkinson S. P., and Roth J. R. "Paraelectric Gas Flow Accelerator" U. S. Patent # 6,200,539 B1, Issued March 13, 2001.
- [25] Roth, J. R.: "Aerodynamic Flow Acceleration using Paraelectric and Peristaltic Electrohydrodynamic (EHD) Effects of a One Atmosphere Uniform Glow Discharge Plasma (OAUGDP<sup>TM</sup>)". Physics of Plasmas, Vol. 10, No.5 (2003).
- [26] Roth, J. R., Sherman D. M. and Wilkinson S. P.: "Electrohydrodynamic Flow Control with a Glow Discharge Surface Plasma", AIAA Journal, Vol. 38, No. 7, July 2000, pp 1166-1172.
- [27] Roth, J. R., Sherman D. M. and Wilkinson S. P.: "Boundary Layer Flow Control with a One Atmosphere Uniform Glow Discharge Surface Plasma". AIAA Paper 98-0328, Proc. of the 36th AIAA Aerospace Sciences Meeting & Exhibit Reno, NV, January 12-15, 1998
- [28] Roth, J. R., Sin, H., Madhan, R. C. M. and Wilkinson S. P.: "Flow Re-Attachment and Acceleration by Paraelectric and Peristaltic Electrohydrodynamic (EHD) Effects". AIAA Paper 2003-0351, Proc. of the 41st AIAA Aerospace Sciences Meeting & Exhibit Reno, NV, January 6-9, 2003.
- [29] Sherman, D. M.: "Manipulating Aerodynamic Boundary Layers Using an Electrohydrodynamic Effect Generated by a One Atmosphere Uniform Glow Discharge Plasma". M. S. in Physics Thesis, Department of Physics, University of Tennessee, Knoxville, August 1998.

- [30] Chen, Z.: "Impedance Matching for One Atmosphere Uniform Glow Discharge Plasma (OAUGDP<sup>TM</sup>) Reactors", IEEE Trans. Plasma Sci., Volume: 30, Issue: 5 , Oct. 2002, Pages:1922 - 1930
- [31] Sin, H.: Polyphase Power Supply and Peristaltic Flow Accelerator Using a One Atmospheric Uniform Glow Discharge Plasma". M.S. in Electrical Engineering Thesis, Department of Electrical and Computer Engineering, University of Tennessee, Knoxville, December, 2002.
- [32] PCI/PXI-6711/6713 User Manual, National Instruments, October 1998 Edition Part Number 322080A-01.

## **VITA**

Madhan Raja Chandra Mohan was born in Virudhunagar, India. He received his bachelor of engineering degree in electrical and electronics engineering from Madurai Kamaraj University, India. In August 2001, he began his graduate study at the University of Tennessee at Knoxville and worked as a graduate research assistant at UT Plasma Sciences Laboratory assisting with research involving OAUGDP<sup>TM</sup> plasma actuators. His research interests include industrial applications of plasma, VLSI design and analog circuit design. He is a student member of IEEE Nuclear and Plasma Sciences Society and a recipient of IEEE Nuclear and Plasma Sciences Society travel grant award in 2003. He plans to graduate with a Master's degree in Electrical engineering in August, 2004.